3-21-2019

Examination of Flow Dynamics and Passive Cooling in an Ultra Compact Combustor

Tylor C. Rathsack

EXAMINATION OF FLOW DYNAMICS AND PASSIVE COOLING IN AN ULTRA COMPACT COMBUSTOR

THESIS

Tylor C. Rathsack, Captain, USAF

AFIT-ENY-MS-19-M-239

DEPARTMENT OF THE AIR FORCE
AIR UNIVERSITY

AIR FORCE INSTITUTE OF TECHNOLOGY

Wright-Patterson Air Force Base, Ohio

AFIT-ENY-MS-19-M-239

EXAMINATION OF FLOW DYNAMICS AND PASSIVE COOLING IN AN ULTRA COMPACT COMBUSTOR

THESIS

Presented to the Faculty

Department of Aeronautics and Astronautics

Graduate School of Engineering and Management

Air Force Institute of Technology

Air University

Air Education and Training Command

In Partial Fulfillment of the Requirements for the

Degree of Master of Science in Aeronautical Engineering

Tylor C. Rathsack, BS

Captain, USAF

March 2019

DISTRIBUTION STATEMENT A.

APPROVED FOR PUBLIC RELEASE; DISTRIBUTION UNLIMITED

AFIT-ENY-MS-19-M-239

EXAMINATION OF FLOW DYNAMICS AND PASSIVE COOLING SCHEME IN AN ULTRA COMPACT COMBUSTOR

Tylor C. Rathsack, BS

Captain, USAF

COMMITTEE MEMBERSHIP

Marc D. Polanka, PhD
Chair

Lt. Col James L. Rutledge, PhD
Member

Major Levi M. Thomas, PhD
Member

Major Brian T. Bohan, PhD
Member

Abstract

The Ultra Compact Combustor (UCC) promises to greatly reduce the size of a gas turbine engine's combustor by altering the manner in which fuel is burnt. Differing from the common axial flow combustor, the UCC utilizes a rotating flow, coaxial to the engine's primary axis, in an outboard circumferential cavity as the primary combustion zone. The present study investigates two key UCC facets required to further this combustor design.

The first area of investigation is cooling of the Hybrid Guide Vane (HGV). This UCC specific hardware acts as a combustor center body that alters the exit flow angle and acts as a secondary combustion zone. As improved UCC designs yield higher operating temperatures, cooling of this component must be considered. Previous numeric efforts determined the viability of a passive cooling scheme where cooler compressor air was drawn into an opening at the stagnation region of the HGV and used for both internal and film-cooling of the vane. The present study experimentally investigated the performance of five cooled HGV configurations, each having a unique combination of film-cooling, internal passage area, and internal passage geometry, over a range of flow conditions. Results confirmed the efficacy of HGV cooling via passive air ingestion. The internal vane geometry affected both internal coolant mass flow and pressure rise offering a means to adjust both parameters based on cooling requirements. Vane internal to external pressure differential had a strong impact on blowing ratio where low differences provided sub-optimal cooling benefits and large differences caused the coolant jet to penetrate into the freestream, altering its flow structure.

Next, the UCC hardware was modified to accommodate enhanced combustor diagnostics. Previous studies relied on point measurements or optical analysis of a small portion of the cavity

greatly limiting the obtainable data. By replacing the rear enclosure of the combustor with a clear quartz back plate, analysis of the flow dynamics in the entire cavity was made possible. Design features that ensured a sealed combustor while still accommodating thermal expansion of the quartz allowed extensive data to be collected while avoiding damage to the modified hardware.

These modifications were then leveraged to assess the underlying complex aerodynamic and combustion phenomenon driving previously observed average combustor exit temperatures. Emissions of OH and CH radicals were recorded using intensified relay optics and a high speed camera providing information on flame location. Tracking the flame's movement enabled it's velocity within the cavity to be determined. Observed average cavity tangential velocity increased with cavity airflow rate and had the highest local value within the cavity, near the step air injection. Velocity was lowest at the vane tips of the HGV, which locally disrupted flow migration. Increased tangential velocities adversely affected the ability of the flame stabilizing mechanism to anchor a flame, resulting in less overall flame activity at higher cavity velocities. This was primarily driven by the method of air injection which, at all but the lowest tangential velocities, prevented flow recirculation in half of the stabilizing zones. Further increase in cavity tangential velocity altogether pushed the flame off of the outside diameter of the combustor, which temporarily stabilized around the HGV prior to extinguishing. Lastly, analysis of combustion event movement indicated larger tangential velocities decreased residence time coinciding with a previously observed drop in average combustor exit temperature.

Acknowledgments

First and foremost, I owe my success and survival to God. Knowing that He placed me on the path that led to AFIT gave me the constant encouragement that He would see me through my time here. I also enjoyed seeing His divine providence (which Tony Evans describes as “the way God arranges things to achieve His sovereign purpose”) play out day-to-day. This was most true in frustrating setbacks in the lab that led to a better understanding of His peace and the many hours spent on writing that helped me grow in patience.

Secondly, I would like to thank my wife. We married and moved in together the weekend before I started my time at AFIT making my Master’s work a large part of our married life together. Despite the competition for my time, my wife has been wonderfully understanding and supportive. I’ve been most impressed by her willingness to be my flash card buddy to help me study for my exams.

Lastly, I would like to thank all of the folks who went above and beyond their simple job descriptions to help me. My advisor, Dr. Marc Polanka, gave hours of his week and weekends to read my papers and guide me towards better critical thinking. My committee members (Lt Col Rutledge, Major Thomas, and Major Bohan) shared their engineering and writing expertise. Lt Kevin DeMarco and Mr. Carl Pickl provided immeasurable help with the UCC hardware. The AFIT ENY lab technicians (Mr. Jamie Smith, Mr. Josh DeWitt, Mr. Keith Long, and Mr. Mike Ranft) provided excellent help with the lab facilities. Mr. Brian Crabtree and Mr. Joe Owings improved and brought my UCC designs to life. Finally, I need to thank Dr. Larry Goss of ISSI who always made time to help me with lab setup, data collection, and post-processing.

Tylor C. Rathsack

Table of Contents

List of Figures

List of Tables

List of Abbreviations

List of Symbols

I. Introduction

The design of a jet engine's combustor has employed the same flow configuration since its creation over 80 years ago. Air leaving the compressor is oriented axially by the compressor exit guide vanes, travels through the combustor with a bulk axial motion, and routes through a turbine inlet guide vane prior to entering the turbine. This configuration results in a combustor length on the order of 25 – 50 cm [1] not including the length of the two guide vanes. Modern aviation demands for more power from smaller engines is straining the limits of this combustor configuration.

The Ultra Compact Combustor (UCC) is a promising technology with the potential to help meet these demands by reducing the length, and thus size, of a gas turbine engine's combustor by 66% [2] using the configuration shown in Figure 1. This shortening is achieved by burning the fuel circumferentially in a swirling flow field with an axis of rotation coaxial to the primary axis of the engine. Two benefits of this orientation drive the resulting length savings. The first is based on the work of Lewis [3] who showed that a centrifugal force imparted on a reacting flow will increase the rate of flame propagation. The second results from altering the traditional linear flow path through the combustor to a rotating one that moves along the perimeter of the engine. This change enables paths of travel well in excess of what the axial length alone would permit.

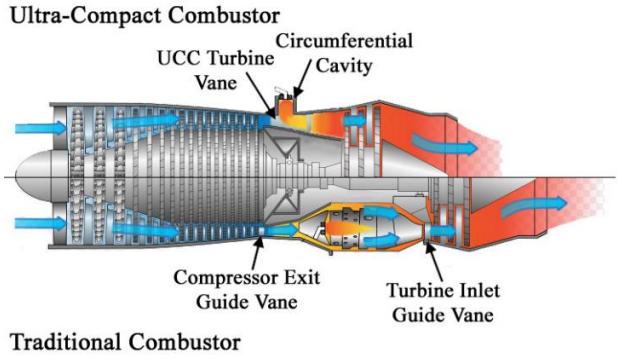

Figure 1: Engine with UCC compared to engine with traditional combustor [4]

The Air Force Institute of Technology (AFIT) has been actively researching ultra compact combustion since 2005. While originally designed to capitalize on the findings of Lewis [3], recent research by DeMarco [5] has shown that balancing centrifugal loading and fuel residence time within the combustor is necessary to achieve higher operating temperatures. The extent of this relationship and the specific flow phenomena driving it have not been investigated and requires further diagnostic measurements to do so.

Additionally, AFIT's UCC employs a combustor center body that facilitates rotational flow within the combustor. This unique component also serves as the compressor exit and turbine inlet guide vanes, helping to realize the desired length savings. As design improvements continue to increase the UCC's operating temperatures, cooling of this center body must be considered.

1.1 Research Objectives

The first objective of the present investigation is to determine the impact of passive cooling schemes for the combustor center body. Previous Computational Fluid Dynamics (CFD) investigations by Bohan et al. [6] and DeMarco et al. [7] assessed the viability of using direct ingestion of cooler incoming compressor air to reduce the temperature of the combustor center body which is exposed to hot reacting fuel. Their efforts explored several variations of vane internal and external geometry to achieve this result, but the impact of these schemes has not been experimentally evaluated. As such, data on the effectiveness of vane internal flow and external film-cooling to reduce the center body temperature must be collected to further the design of this component.

To continue to enhance UCC operating temperatures, the complex aerodynamic and combustion phenomena within the circumferential cavity must be understood. Previous numeric studies have shown that this combustor flow varies in both the radial and tangential directions.

However, previous experimental data such as thermocouple readings or an optical window that enabled visual access to 20% of the combustor volume have required the analyst to surmise combustor behavior in the unobserved regions. Therefore, a necessary task of the present investigation is to modify the existing UCC hardware by increasing optical access to enable further diagnostic measurements. This change will decrease data uncertainty and enable previously not understood flow behavior to be more accurately characterized.

The second objective of this research is to investigate the combustion cavity behavior that resulted in the findings of DeMarco et al. [8]. Their investigation found that lower tangential velocity, and thus centrifugal loading, within the combustion cavity increased UCC exit temperature. Fuel particle residence time is suspected to be the missing link between centrifugally enhanced combustion discovered by Lewis [3] and the observations of DeMarco et al., but no previous measurements have been able to confirm this hypothesis.

The next four chapters describe the support, research, and conclusions of these three objectives. First, Chapter Two details work conducted by previous researchers that has been used to guide the present effort. Chapter Three discusses the design and implementation of the experimental hardware used to investigate center body cooling schemes and UCC flow. Chapter Four discusses the data that was collected and the subsequent analysis efforts. Lastly, Chapter Five summarizes the results for all three objectives and lays the groundwork for future research.

1.2 Objective Summary

1. Determine the impact of passive cooling schemes for the combustor center body
2. Investigate the combustion cavity behavior that resulted in previously observed combustor exit temperatures
    a. Enabling Task: Modify the existing UCC hardware by increasing optical access to enable further diagnostic measurements

II. Background

Aircraft development is pushing for reduced engine sizes and the UCC promises to help realize this goal. While the UCC burns fuel in a different manner than traditional engines, it is based on the same basic combustion principles discussed in Section 2.1. Research on combustion principles specifically applied to the UCC are discussed in Section 2.2 and development of AFIT's UCC is detailed in Section 2.3. Improved combustor designs have led to increased operating temperatures requiring the cooling of the UCC center body which is discussed in Section 2.4. Lastly, infrared thermography (Sections 2.5) and chemiluminescence imaging (Section 2.6) are described as optical measurement techniques required for achieving the objectives stated in Chapter One.

2.1 Combustor Fundamentals

Modern turbine engines rely on combustors to add the requisite energy to power their thermodynamic cycle. Combustors achieve this energy rise through converting stored energy in a fuel's chemical bonds into heat via a chemical reaction called combustion. As such, to understand an engine's combustor, one must first understand the underlying combustion reaction [9].

At the most basic level, combustion is controlled by the chemical reaction in Equation 1, where the hydrocarbon fuel reacts with atmospheric air producing carbon dioxide and water while carrying through the diatomic nitrogen. This reaction is presented at an equivalence ratio of one (Φ=1 or stoichiometric) meaning the proportion of air to fuel is balanced such that all O_2 is completely reacted. The equivalence ratio can be calculated with Equation 2, noting that a Φ greater than one results in excess fuel (rich) and a Φ less than one (lean) results in a surplus of air. Aircraft obtain the necessary air for combustion from their surroundings and thus only have to

provide the fuel for combustion. As such, aviation combustors operate at lean conditions, on the order of Φ=0.3, to help ensure all fuel is completely reacted [1].

$$C_xH_y + a(O_2 + 3.76N_2) \xrightarrow{yields} xCO_2 + \left(\frac{y}{2}\right)H_2O + 3.76N_2 \quad (1)$$

$$\frac{\left(\frac{\dot{m}_{fuel}}{\dot{m}_{air}}\right)}{\left(\frac{\dot{m}_{fuel}}{\dot{m}_{air}}\right)_{stoic}} \quad (2)$$

The rate fuel reacts with air can be determined via Equation 3 first proposed by Arrhenius and taken from Turns [9]. The pre-exponential factor *A* is determined by the reaction's chemistry and is proportional to pressure for hydrocarbons. The exponent components are activation energy of the reactants, E_{act}, universal gas constant, *R*, and temperature, *T*.

$$k(T) = Ae^{\frac{-E_{act}}{RT}} \quad (3)$$

Chemical reaction rate in turn effects the speed at which the flame front propagates through the unreacted fuel and air mixture, called the flame speed, which can be broken into laminar S_L, and turbulent S_T speeds according to the regime of the combusting flow. Equation 4 shows the calculation for S_L where α is the thermal diffusivity, $\dot{m}_F$ is the average volumetric mass production rate of the fuel per unit volume, and ρ_u is the density of the reactants [9]. The laminar flame speed is purely a function of the thermal and chemical properties of the mixture and is independent of flow properties. Turbulent flames are driven by the same chemistry as laminar flames, but have the addition of turbulent eddies to distort the flame structure which increases flame speed. S_T can be calculated with Equation 5 where $\dot{m}$ is the reactant flow rate and $\bar{A}$ is the time-mean flame area. Calculating the later of these parameters is no straightforward task, thus Klimov [10] proposed a

relation between S_L and S_T based on empirical data, where v'_{rms} is the turbulence intensity as seen in Equation 6.

$$S_L = (-2\alpha\left(\frac{\dot{m}_{air}}{\dot{m}_{fuel}} + 1\right)\frac{\dot{m}_F}{\rho_u})^{1/2} \tag{4}$$

$$S_T = \frac{\dot{m}}{\bar{A}\rho_u} \tag{5}$$

$$S_T = 3.5S_L\left(\frac{v'_{rms}}{S_L}\right)^{0.7} \tag{6}$$

The air-to-fuel ratio affects the flame speed and is evaluated from both a global perspective, accounting for the total air and fuel mass flow rates in the combustor, as well as a local value, where the air-to-fuel ratio for a specific region of the combustor is considered. To mix the injected fuel as quickly as possible with the air to achieve the desired local air-to-fuel ratios, combustors employ a variety of techniques. One of the mixing tools employed is the fuel injection nozzle which uses swirl vanes to capture and rotate a portion of the combustor entry air around the fuel injection source quickly distributing the fuel [1]. High pressure fuel injection combined with small injection holes is also used creating a fine fuel mist.

Injected fuel must then undergo a phase change, heat to a sufficient ignition temperature, and completely react prior to exiting the combustor. Sufficient combustor residence time (the time a fuel particle takes to travel through the combustor) must be achieved for this process to complete prior to the end of the combustor. This process is dependent on the fuel-air mixture density, mass flow rate, freestream velocity and combustor geometry [9]. Figure 2 shows one effort taken to reduce traditional combustor length while maintaining sufficient residence time by leveraging secondary air introduction normal to axial flow. Doing so simultaneously decreases linear velocity

and shears the flow driving the formation of a recirculation region upstream of secondary air introduction.

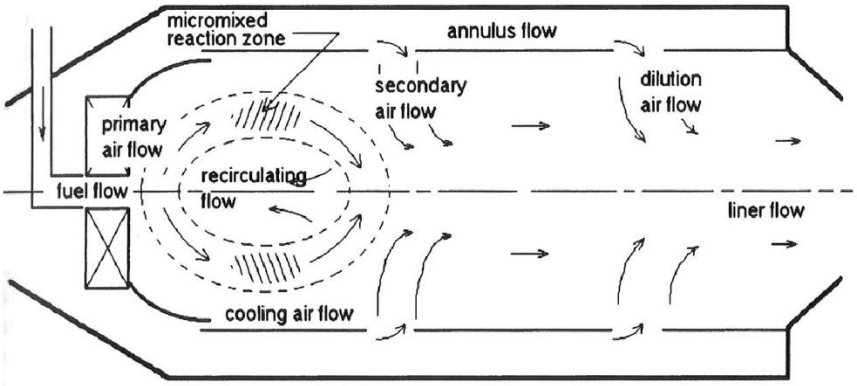

Figure 2: Combustor air introduction creating a recirculating flow field [1]

Yonzawa et al. [11] combines combustion time τ_c, air and fuel mixing time τ_m, and fuel residence time in the combustor τ_r, as components of Yonzawa's combustor efficiency parameter η_c seen in Equation 7. This parameter serves as one means to assess the quality of a combustor. By examination, combustor efficiency can be improved by increasing combustion time, air and fuel mixing time, or decreasing fuel residence time, provided fuel is still completely reacted prior to exiting the combustor.

$$\frac{\tau_c + \tau_m}{\tau_r} = \eta_c \tag{7}$$

The range of freestream velocities, turbulence levels and equivalence ratios over which a combustor can maintain stable operation is another metric against which combustor designs are measured. Bluff bodies are commonly employed to increase combustion stability and work by creating a recirculating region in the flow path. Incoming unburnt reactants are displaced around the body, detach from the surface, and come into contact with the higher energy recirculation zone behind the body where heat transfer begins to occur. The reactants quickly reach their ignition

temperature, combust, and then a portion of these products are entrained into the eddy and perpetuate the process. If the eddy gains less energy than it imparts to the incoming flow, a flameout will occur. The energy required to ensure stable combustion can be calculated via Equation 8 where V_∞ is the freestream velocity, δ_t is the thermal boundary layer thickness, and C_p is specific heat [12].

$$V_\infty[\delta_t(\rho * C_p)(T_{ignition} - T_{\infty)}] = \mathrm{E_{req}} \quad (8)$$

A common bluff body employed in afterburners is the V-gutter as shown in Figure 3. This design balances pressure loss, heat transfer to the bluff body and flame stability to create an ideal flame anchor in axial flow [12]. Another flame stabilization geometry is the backward facing step [13]. Lapsa and Dahm [15, 16] investigated the backward facing step stabilizing method in both a straight and curved combustor section seen in Figure 4. Premixed air and fuel were forced through a metal mesh, traveled through a segment of the test area, passed over the step and then ignited at the bottom of the step. Using the flat configuration as a baseline, the effects of centrifugal acceleration on step stabilized combustion were studied. Three phenomena were found to drive the flow behavior over the step: the first of which was the velocity difference between the main flow path and the velocity at the step face. This velocity gradient created a shear region which in turn created a recirculation region behind the step. Next, centrifugal forces on the fuel and air mixture caused stratification of the mixture where the heavier fuel was flung towards the outside radius displacing the lighter air which was pushed radially inward. Lastly, the fuel then combusted, decreasing in density and thus displaced radially inward by the then denser reactants. This final process created a density based instability that Lapsa and Dahm found to overwhelm the shear

driven instability within 1-2 step heights downstream. Shadowgraph images from the experiment help visualize the flame boundaries and can be seen in Figure 5.

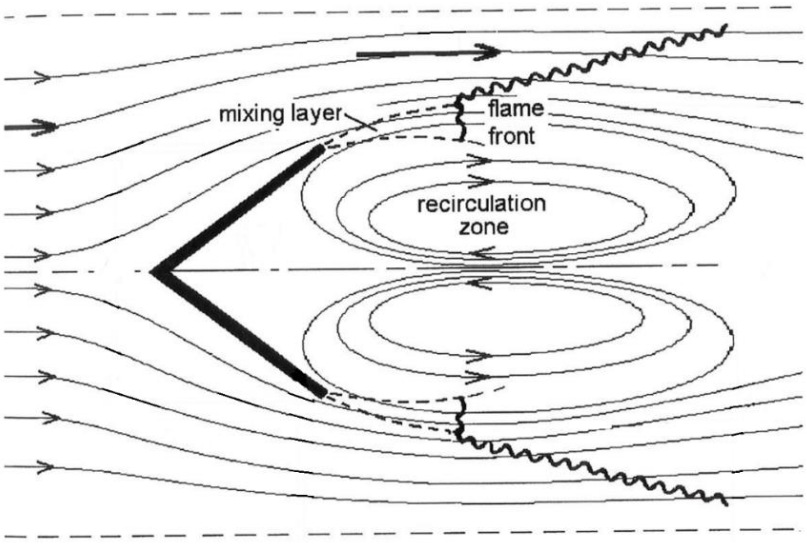

Figure 3: "V" shaped bluff body used to create recirculation zone [1]

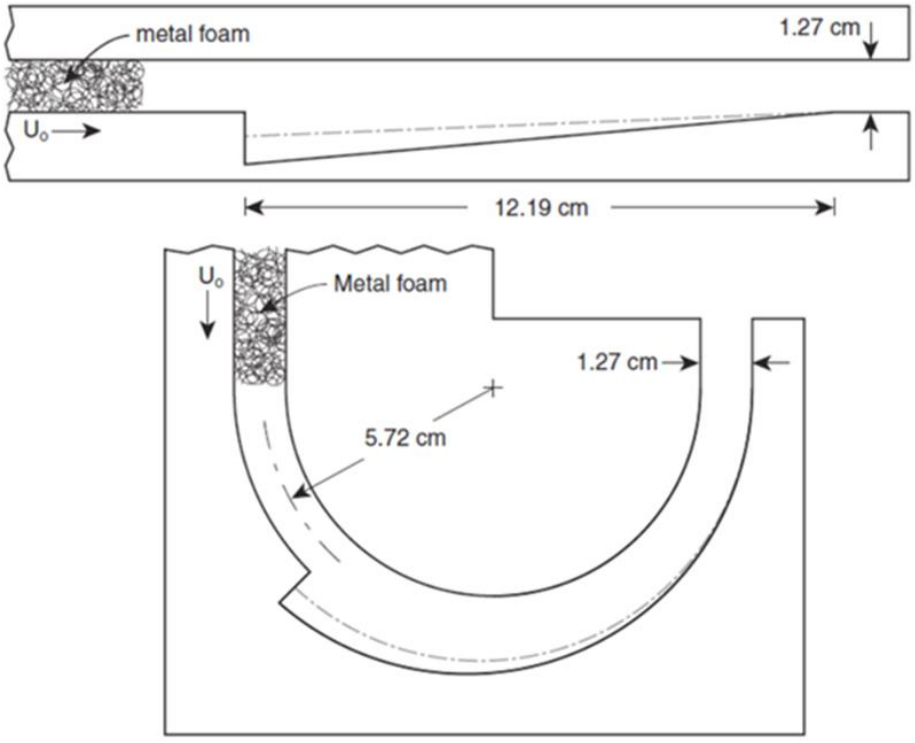

Figure 4: Backward facing step designs investigated by Lapsa and Dahm [15]

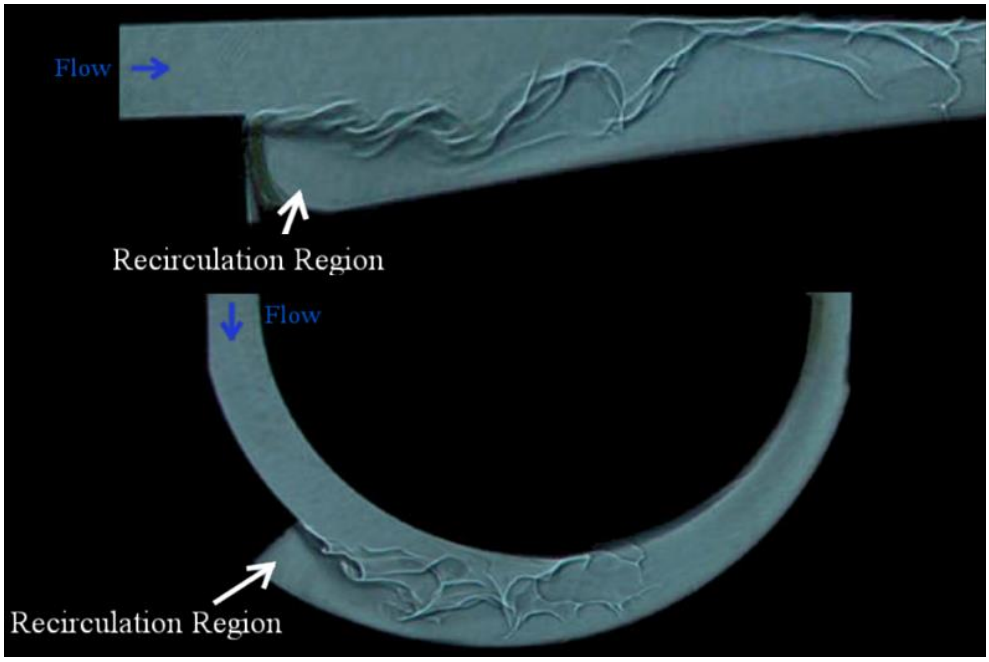

Figure 5: Backward facing step combustion shadow graphs with no centrifugal loading (top) and with centrifugal load (bottom) [15]

The last metric used to evaluate a combustor's performance that will be discussed in this review is temperature uniformity, typically measured with Pattern Factor, PF, shown in Equation 9. In this equation, the difference between the turbine inlet temperature, T_{t4}, maximum local value and average value is divided by the difference between the average turbine inlet temperature and combustor inlet temperature, T_{t3}. Uneven exit temperatures negatively impact turbine hardware life and performance. Legacy engines have a PF in the range of 0.25-0.45, but modern engines have a more restrictive 0.15-0.25 [1] in order to extend turbine hardware life.

$$PF = \frac{T_{t4max} - T_{t4avg}}{T_{t4avg} - T_{t3}} \tag{9}$$

2.2 The Ultra Compact Combustor

The UCC was designed to capitalize on the enhanced rates of flame propagation in a centrifugally loaded combustion system as first observed by Lewis [3]. Lewis found that the flame

within a closed pipe filled with pre-mixed air and propane that was rotated about its center like a propeller propagated faster than the theoretical turbulent flame speed. He used the non-dimensional "g-load" to described the centrifugal force exerted on the fuel and air mixture which is shown in Equation 10 where V_{tan} is the tangential fluid velocity, r is the distance from the axis of rotation, and g_c is the force due to gravity [16]. Below 200 g's, Lewis did not note an increase in flame speed, but at 500 g's he found the flame speed to increase by the square of the centrifugal force applied. This trend continued until 3,500 g's, where it abruptly reversed until blowout. Equation 11 is the empirically derived relation between g-load and flame speed and Figure 6 shows this trend overlaid on Lewis' experimental data.

$$g_{Load} = \frac{V_{tan}^2}{r * g_c} \tag{10}$$

$$S_B = 1.25\ (ft/s)\sqrt{g_{Load}} \tag{11}$$

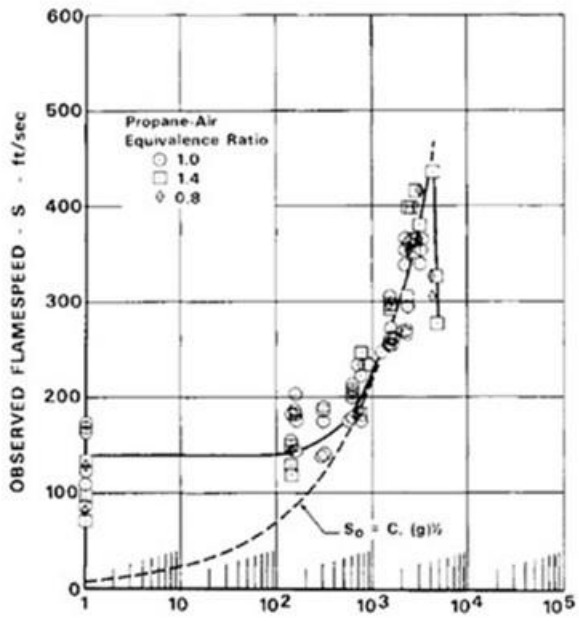

Figure 6: Experimental observations of Lewis [3]

Lewis offered the “bubble transport theory” as an explanation of the observed increase in flame speed. Figure 7 presents a visual of this theory where the shaded circle is the flame bubble, the dashed line represents the flame expansion after a time step Δt, resulting from turbulent flame propagation, and the circle with a plus is the location of the flame bubble at Δt. The left hand graphic shows a scenario at less than 200 g’s, where the flame bubble is displaced less than the flame expansion due to turbulent flame propagation. The middle graphic depicts a g’s of 500-3,500 where the centrifugal body forces are pushing the flame bubble beyond the turbulent flame propagation region, increasing the observed flame speed. The last image has the same g’s as the previous case, but with a much higher turbulent flame speed. Even though the flame bubble has displaced as far as case two, the observed flame speed does not increase with g’s because of the high baseline propagation rate.

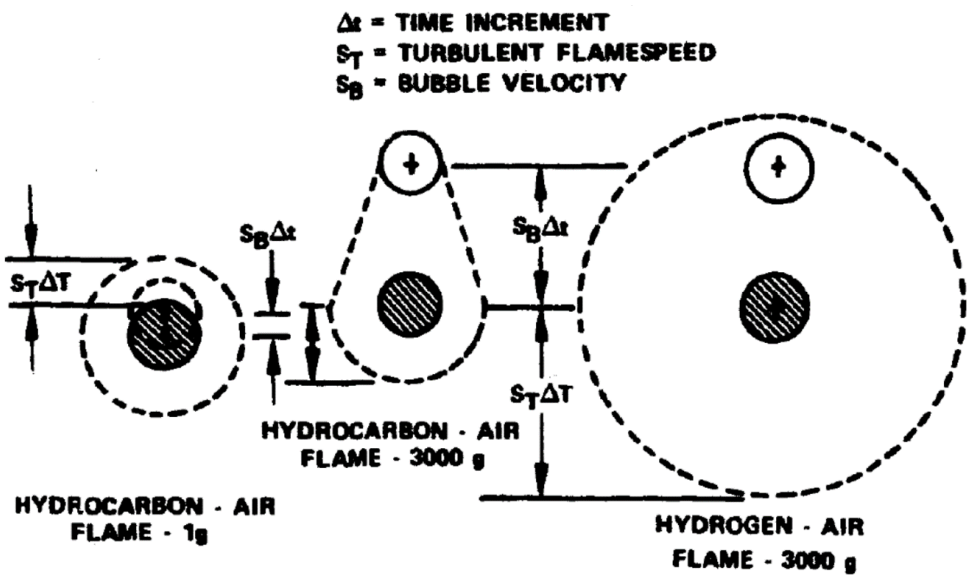

Figure 7: Visual depiction of the bubble transport theory [3]

Briones et al. [17] conducted a numeric investigation to further explorer the work of Lewis. CFD results agreed with the Lewis’ findings showing increased observed flame propagation with centrifugal loading until 3,000 g’s where the trend reverses, with further acceleration leading to

flameout. Figure 8 depicts flame propagation with no centrifugal acceleration and ignition occurring at t=0. The flame then begins to move forward driven by the turbulent flame speed, gas expansion due to heating, and induced Rayleigh-Taylor instabilities at the flame front due to a density gradient. At t=8 ms, the flame front becomes corrugated and in the next 6 ms stretches to the point of breaking up and allowing pockets of unburnt mixture to penetrate into the hot gas region. While an initial retreat of the flame occurs, the pre-heating of this mixture quickly causes it to ignite, accelerating the flame forward.

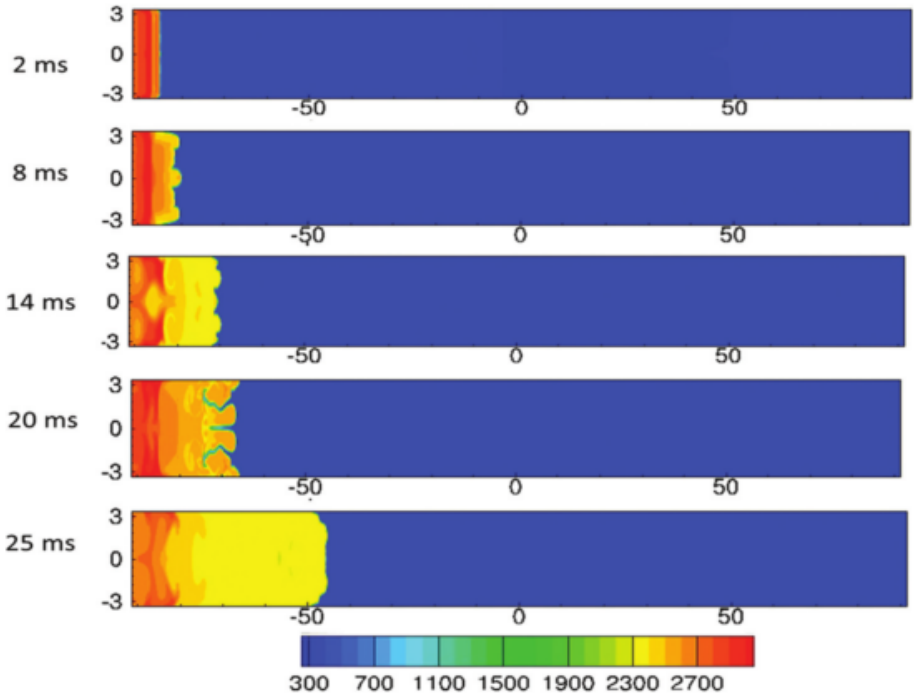

Figure 8: Progressive temperature contours of propane and air premixed flame with no centrifugal loading (dimensions in centimeters) [17]

Effects of centrifugal force, quantified as a g-load to match Lewis, can be seen in Figure 9 presented at a uniform time step of t=8 ms. All accelerated flames, except the highest case, exhibit a similar structure having a protruding convex flame region that becomes progressively more corrugated with increased acceleration. When this corrugation becomes excessive, penetration of

unburnt mixture quenches the reaction as seen at the 3,000 g-load case. Briones proposed that Rayleigh-Taylor instabilities resulting from the centrifugally induced density stratification are driving this observed flame propagation increase [17]. It is important to note that while the proposed mechanism is different than the bubble transport theory of Lewis, both agree on the resulting effect.

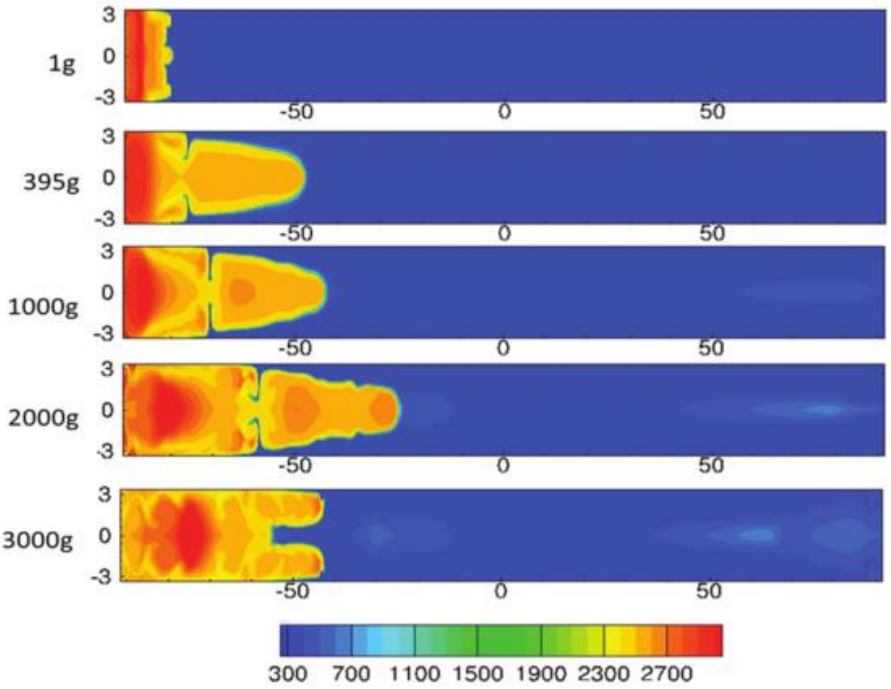

Figure 9: Temperature contours of varied g-load propane and air premixed flame at t=8 ms (dimensions in centimeters) [17]

Zelina et al. [2] created a combustor that applied centrifugal loading, via circumferential flow coaxial to the inlet flow axis, to investigate rotational combustion operability. By conducting a series of lean blowout tests at a variety of equivalence ratios, the area of stable combustion, related to equivalence ratio and centrifugal loading, was determined. The results of this study are presented in Figure 10, indicating a strong relationship between equivalence ratio and maximum centrifugal loading that can be applied prior to flameout.

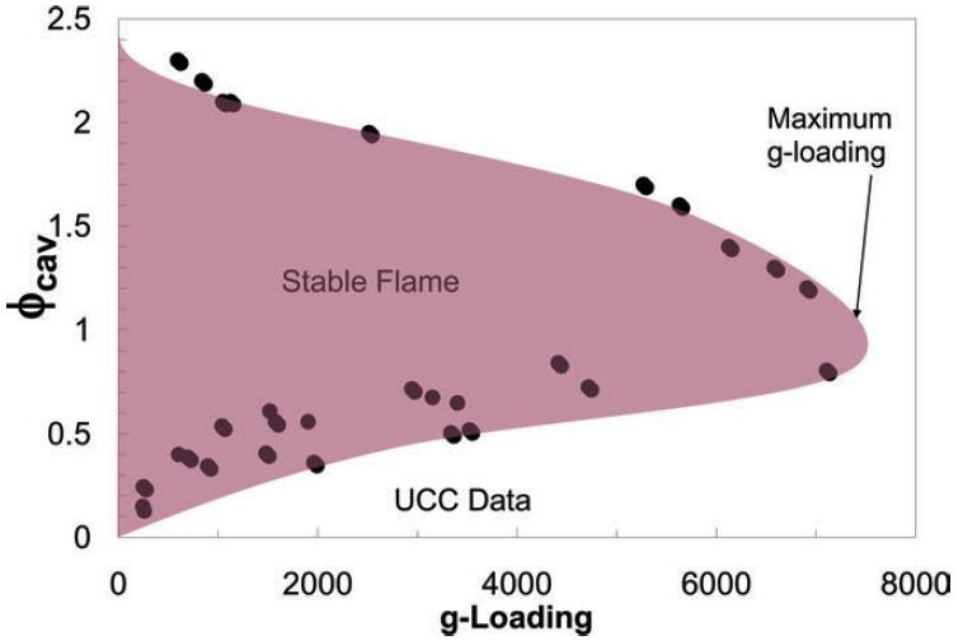

Figure 10: UCC operability limits as a function of equivalence ratio and centrifugal force [2]

2.3 AFIT's Investigation of UCC Dynamics

AFIT began research on the UCC in 2005 with Moenter [18] conducting a numeric investigation of centrifugal combustion. Thomas [19] and LeBay [20] leveraged these numeric findings to construct sector rigs which were experimentally investigated with a variety of optical techniques. A fully annular UCC was conceptualized by Bohan and Polanka [4] and computationally analyzed in both a representative engine and AFIT laboratory configuration. Their design introduced a Hybrid Guide Vane (HGV) which fulfilled the roles of the compressor exit and turbine inlet guide vanes as well as well as serving as the secondary combustion zone. The HGV was located in the center of the combustor and entrained the primary zone flow as it moved radially inward. However, this configuration created non-ideal pattern factors as the hot products were not fully migrating towards the inside diameter. Figure 11 shows the extent of this non-uniformity where the total exit temperature varies by nearly 1,000 Kelvin across the radial span.

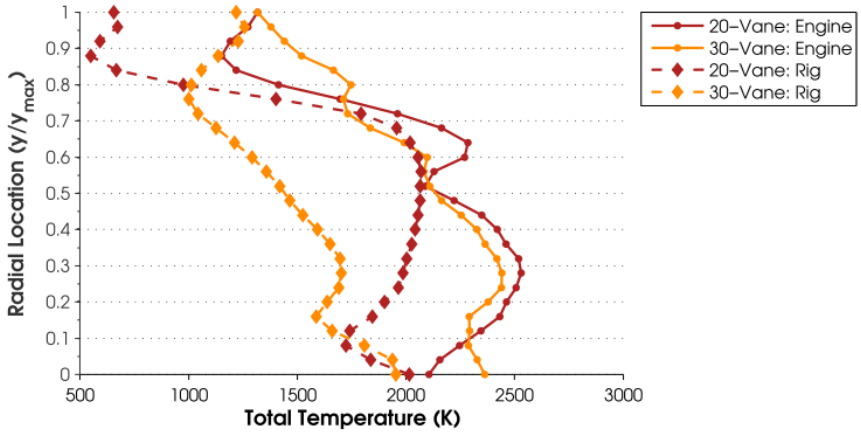

Figure 11: Circumferentially-averaged numeric total temperatures at UCC exit [4]

Leveraging the results of this study, a sub-engine scale fully annular test rig was designed, built, and tested by Wilson et al. [21] to replace the previous sector models. The designed HGV consisted of six vanes that wrapped 160° degrees around a center body and can be seen in Figure 12 with the air/fuel injection ring that formed the perimeter of the circumferential cavity depicted to indicate placement. Two sources of air were supplied to this configuration as seen in Figure 13; the core flow which fed directly into the HGV vane passages and the cavity flow which was supplied from a secondary air source and was fed into the cavity.

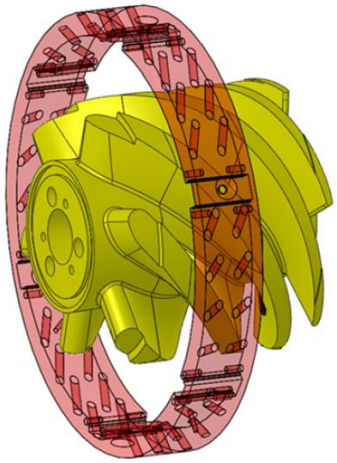

Figure 12: HGV with air/fuel injection ring depicted to indicate placement [21]

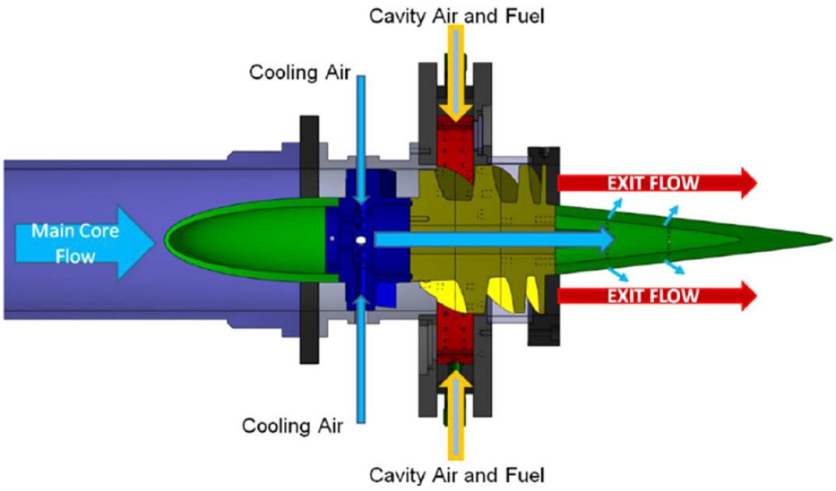

Figure 13: Separate air source UCC configuration [21]

Recognizing that an engine integrated UCC would have to operate on a common air source, Conrad et al. [22] developed a fixed position flow splitting diffuser that was intended to control the airflow to the core and cavity. The resulting experimental configuration can be seen in Figure 14 and Figure 15. Rotation in the combustion cavity was achieved via the angled holes in the air injection plate which imparted a tangential velocity to the air passing through it. Fuel was injected at the outside diameter of the combustion cavity, normal to the primary axis, at six discrete locations. A core restrictor plate designed by Cottle et al. [23] was required to achieve the desired core to cavity flow splits. While the diffuser was further refined by Cottle and Polanka [27, 28], operational control was limited to one flow split as the diffuser geometry was fixed.

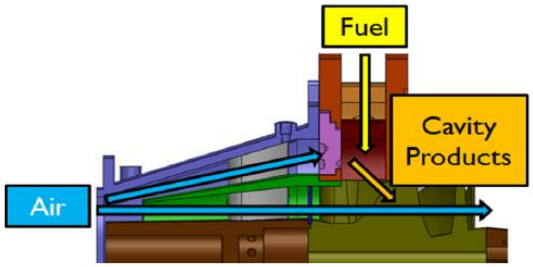

Figure 14: Single air source configuration with flow splitting diffuser [25]

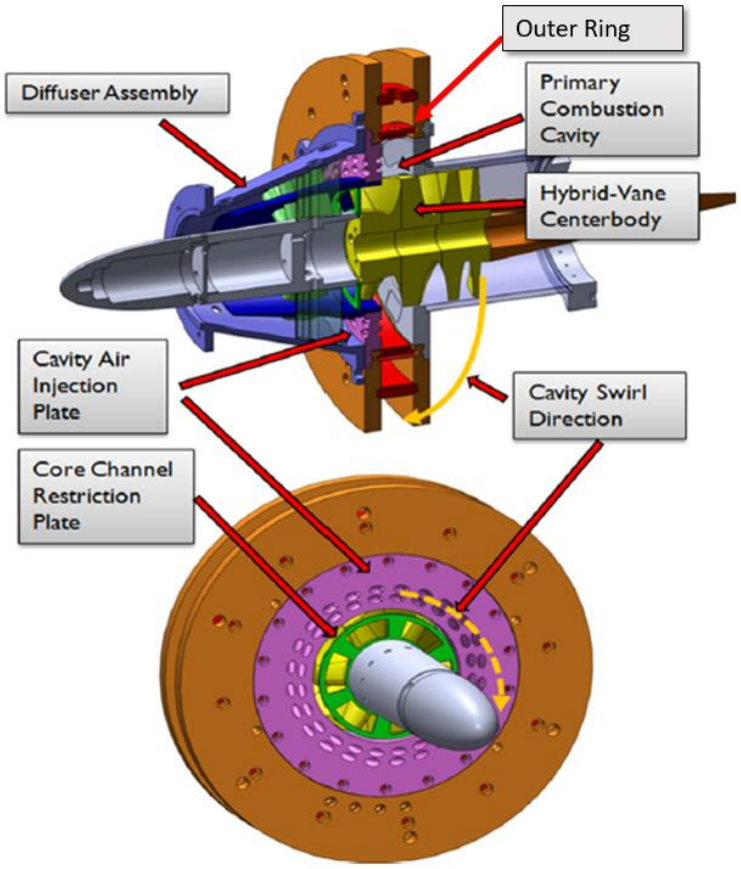

Figure 15: Single air source UCC configuration [25]

To address this limitation, Bohan et al. [26] developed a variable position diffuser that enabled real time control of flow splits to the cavity and core, which is discussed in greater detail in Section 3.1.1. Bohan et al. [27] employed Chemiluminescence Imagery (CI), discussed further in Section 2.6, to analyze flame movement and luminance intensity across an 80° segment of the combustion cavity at a variety of operating conditions. Bohan et al. noted two unique frequencies: one that was indicative of a revolving flame front and one that indicated a uniformly pulsing flame. Due to the limited window of observation, the flow behavior in the remaining segments of the cavity could not be determined. To answer this unknown, a goal of the present investigation is to

reconfigure AFIT's UCC hardware to accommodate further optical measurements to better understand rotating combustion dynamics in the UCC.

Testing by Bohan et al. [27] also indicated that radial fuel injection in the outer ring both created a high fuel concentration along the outside diameter of the cavity and slowed the circumferential motion of the flow. Accordingly, the outer ring was redesigned (shown in red in Figure 15) incorporating six backward facing steps, each with step face injection locations for air and fuel to increase the tangential velocity in the cavity and dissipate fuel rich regions along the outside diameter. The steps were also intended to increase combustion stability as shown by Lapsa and Dahm [15, 16]. As air entering the cavity would then come from both the air injection plate and step faces, half of the air injection plate holes were covered to increase velocity through the remaining holes. Testing of this new configuration revealed limited operability which was believed to result from inadequate recirculation at the backward facing steps. Their hypothesis was that the fluids exiting through the step face decreased the velocity gradient at the step thus weakening the shear driven recirculation.

To improve the range of flow conditions over which stable combustion could occur, a new outer ring consisting of twelve backward facing steps with two fuel injections points on each step face and three air injection points on every other step was created as seen in Figure 16. DeMarco et al. [8] then created operability maps at several different mass flows which altered the flow splits between the core, air injection plate, and 12-Step outer ring while holding a constant global equivalence ratio of 0.36. An example of their findings can be seen in Figure 17, where the horizontal axis shows the percentage of total airflow going to the core, and the vertical axis shows the percentage of cavity airflow (cavity airflow equals total airflow minus core airflow) sent to the front air injection plate. As fuel mass flow rate was held constant, local cavity equivalence ratio

was determined by the core flow split and is shown horizontally above the plot. DeMarco et al. found three distinct zones on the operating map: a diffuser limited area where the desired flow split could not be achieved with the variable position diffuser due to pressure balances (shown in blue), a flameout region where sustained combustion would not occur (shown in red), and an area of stable combustion. The experimentally found flameout zone boundary occurred whenever 9% or greater of the total airflow was sent to the 12-Step outer ring. By positioning a series of thermocouples at the exit plane of the UCC, an average exit temperature was found for each operable test condition which is indicated in the text box next to the green circles.

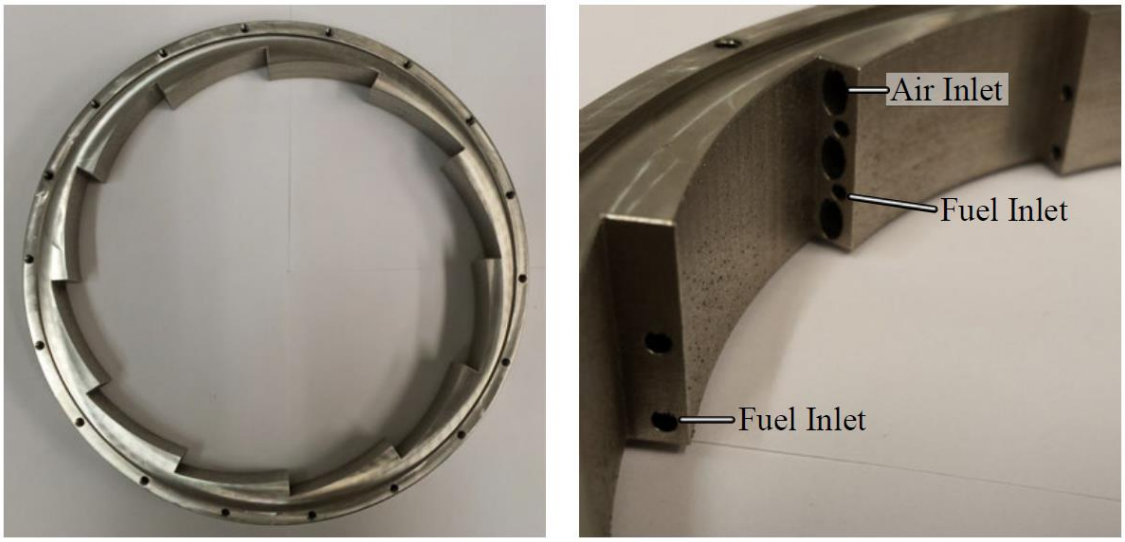

Figure 16: 12-Step outer ring configuration and step configuration [5]

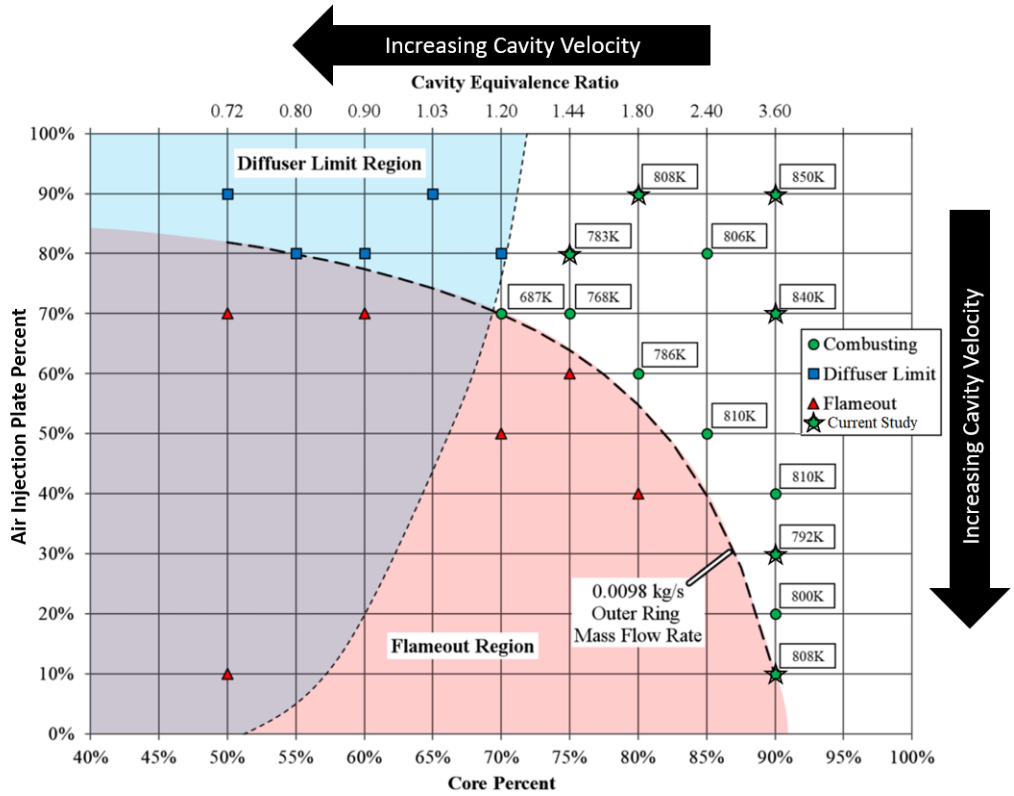

Figure 17: 12-Step average exit temperature operational map at 0.108 kg/s total airflow [8]

The operating map of DeMarco et al. [8] also provides an understanding of combustion cavity tangential velocity. The slowest tangential velocity was in the top right corner and increased as either core flow percentage decreased, as more airflow was then sent to the swirling cavity flow, or front air injection plate percentage decreased, as more air was sent to the 12-Step outer ring which injected air in an almost entirely tangential direction. Combining these velocity trends with the observed exit temperatures indicated that highest combustion exit temperature occurred at the lowest tangential velocities (equating to the lowest centrifugal acceleration). This finding is contrary to their initial goal of using high centrifugal acceleration to enhance combustion. They attributed this finding to increased residence time at lower tangential velocities leading to more complete fuel combustion. Investigating their hypotheses and gaining insight into the combustion

phenomena driving their observed exit temperatures is a necessary step to advancing AFIT's UCC operating temperatures, and as such is a goal of the present investigation.

2.4 Turbine Blade Cooling

Gases exiting the combustor are commonly above the material operating temperature of the turbine blades. In order to maintain their operability, a variety of cooling techniques are employed such as thermal barrier coatings, internal flow cooling leveraging micro-channels, internal air impingement, and exterior film-cooling. Cooling air is taken from the compressor of the engine creating an inefficiency in the engine cycle, but ensures adequate pressure to maintain an interior to exterior flow path in the turbine blades. Figure 18 shows an internal turbine blade cooling scheme proposed by Han et al. [28] where cooler compressor air enters at the blade root, travels through internal channels, and exits the blade through film-cooling holes or slots. Turbulence promoters such as dimples and shaped roughness elements are used to increase the heat transfer from the metal to the cooling air in addition to pin fins that assist in drawing heat away from the blade surface and into the internal coolant flow.

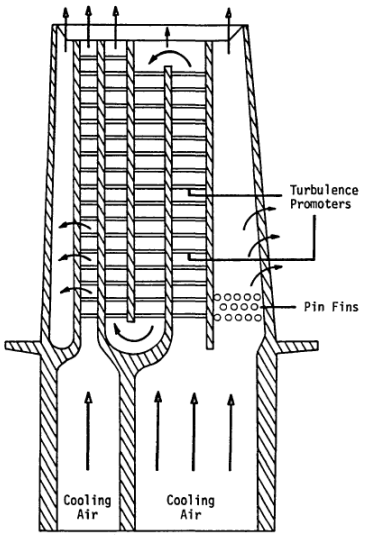

Figure 18: Internal turbine blade cooling [28]

Film-cooling uses a series of small holes or slats to eject the higher pressure internal air creating a cooler air buffer between the hot freestream gases and the turbine blade surface. This can be seen in the right hand image Figure 19. The geometry of the film-cooling holes such as coolant injection angle, compound angle, and Pitch Spacing (*P/D*) has a large impact on the effectiveness of the injected air.

Bogard and Thole [29] describe Blowing Ratio, *M*, as one means of characterizing the coolant jet and represents the ratio of coolant to free stream mass flux as shown in Equation 12, where ρ is the density of the coolant, *c*, or freestream, ∞, and *V* is the corresponding velocity. Blowing ratio can be altered by changing hole placement, as interior and exterior pressure varies across the airfoil, or by changing the hole size. Smaller holes will increase the exit velocity and can be used to increase the blowing ratio in areas of fast freestream flow.

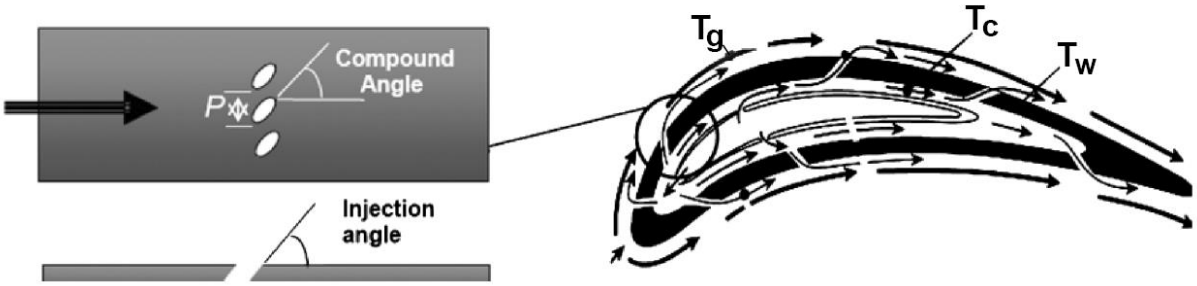

Figure 19: Turbine blade cross section depicting film-cooling airflow [29]

$$M = \frac{\rho_c V_C}{\rho_\infty V_\infty} \tag{12}$$

Bogard and Thule [29] describe a variety of means to characterize the effects of film-cooling, one of which is the adiabatic effectiveness denoted with the Greek symbol η. The calculation of adiabatic effectiveness is shown in Equation 13, where T_∞ is the freestream temperature, T_{aw} is theoretical adiabatic wall temperature, and $T_{c,exit}$ is the internal coolant exit

temperature. The effects of varying blowing ratio on the adiabatic effectiveness was investigated by Baldur et al. [30] and their results for a 30° injection angle hole are shown in Figure 20. As blowing ratio increased, the location of maximum effectiveness, indicated by the white triangle, moved downstream and its area reduced in size. Large blowing ratios resulted in detached jets, which can be seen as areas of low film-cooling adiabatic effectiveness immediately downstream of the coolant hole, which decreased the impact of film-cooling.

$$\eta = \frac{T_\infty - T_{aw}}{T_\infty - T_{c,exit}} \tag{13}$$

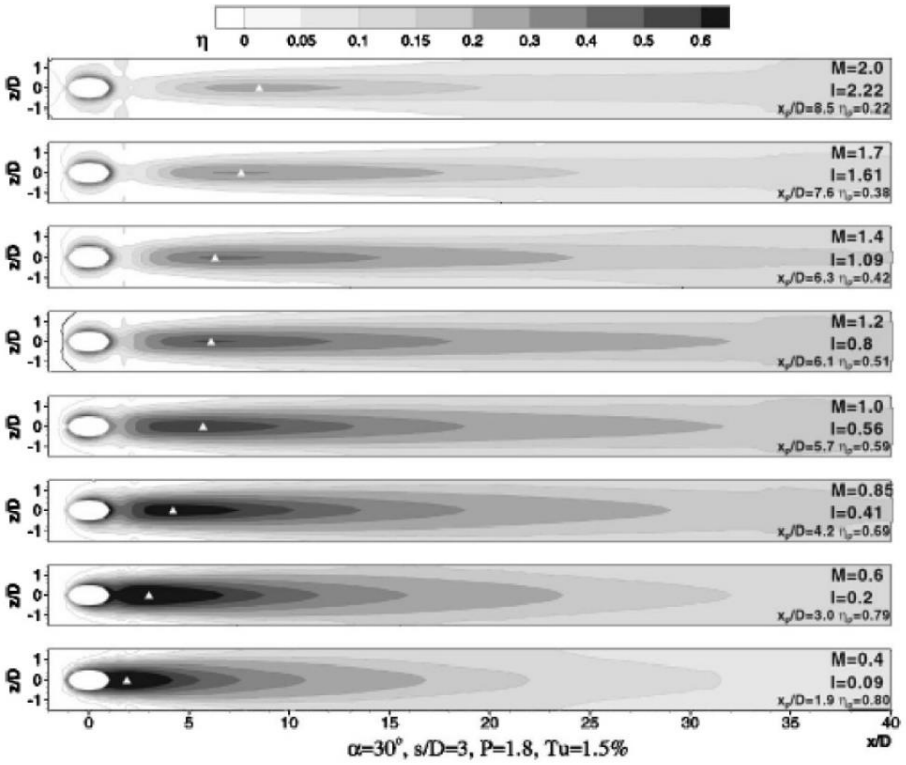

Figure 20: Film-cooling adiabatic effectiveness at various blowing ratios [30]

Variations to whole geometry can vary the injection angle, compound angle, or shape of the hole can alter flow behavior at the surface. Baldauf et al. [30] compared two angles of injection, 30° and 90º, for a cylindrical hole and their results can be seen in Figure 21. Greater effectiveness

was achieved at lower injection angles due to a more attached coolant jet at the vane surface while normal injection led to more separation.

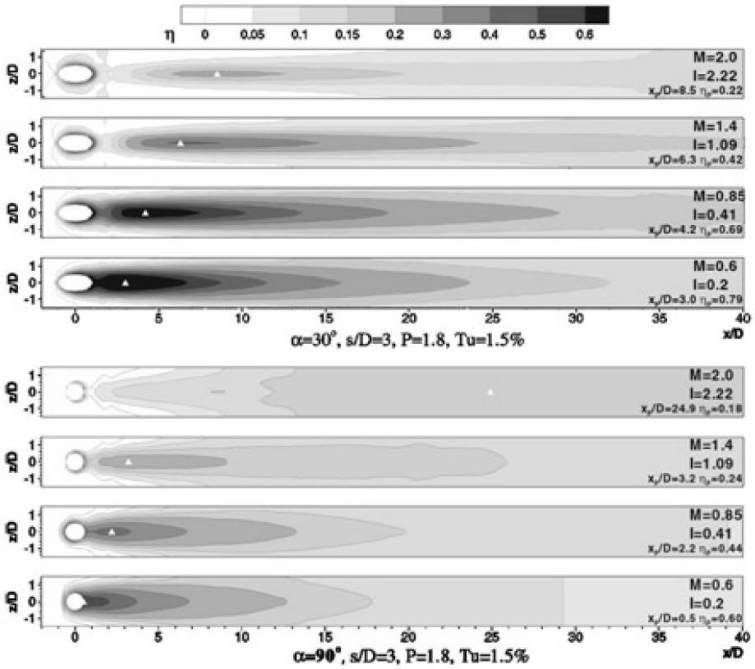

Figure 21: Impact of injection angle on film-cooling effectiveness [30]

Bogard and Thole [29] describe a variety of means to characterize the effects of film-cooling, one of which is the overall effectiveness denoted with the Greek symbol ϕ. This parameter considers the net effect of internal and external cooling by including the temperature of the metal surface as shown in Equation 14, where T_∞ is the freestream temperature, T_m is the metal temperature, and T_{ci} is the internal coolant temperature. Baldauf et al. [30] used this parameter to examine a cross sectional cut along the centerline of an attached (a), reattached (b), and detached (c) coolant jet which can be seen in Figure 22.

$$\phi = \frac{T_\infty - T_m}{T_\infty - T_{ci}} \tag{14}$$

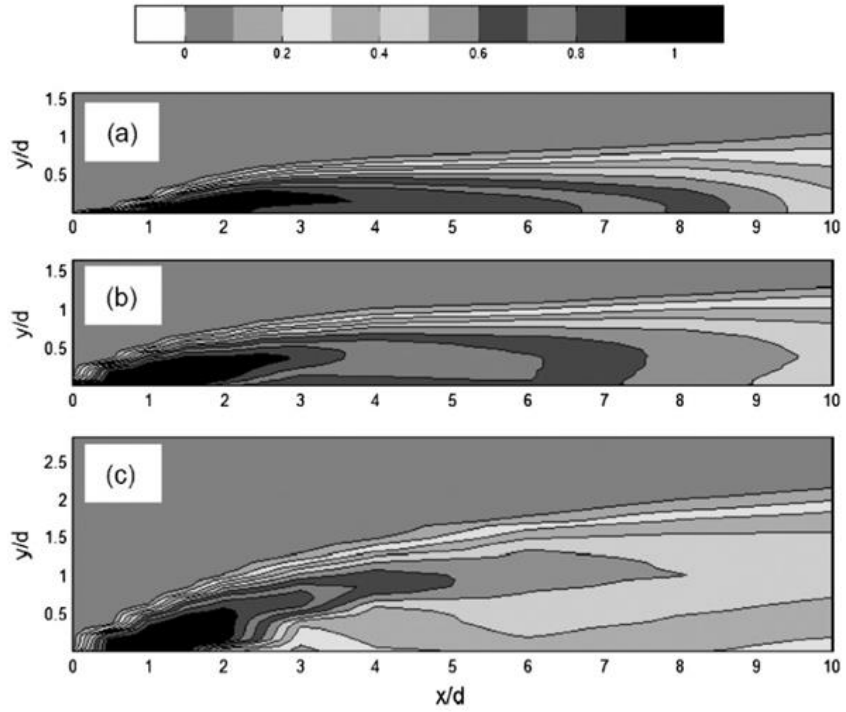

Figure 22: Overall effectiveness along the centerline of attached (a), reattached (b), and detached (c) coolant jet [30]

In turbine hardware where velocity through individual coolant holes is difficult to quantify, the internal to external vane pressure differential in conjunction with hole discharge coefficients and coolant density can be used to determine coolant exit velocity [31]. Discharge coefficient, C_d, is the ratio of actual to ideal discharge which is defined in Equation 15 where A is the hole area, ρ is the coolant density, and ΔP is the pressure differential between the vane interior and exterior. By applying the continuity equation, the mass flow of the jet can be found using Equation 16. Gritsch et al. [32] investigated discharge coefficients for film-cooling holes with varying injection and compound angles. A sample of their findings for a coolant jet aligned with the freestream and having an injection angle of 30º is shown in Figure 23.

$$C_d = \frac{\dot{m}}{A\sqrt{2\rho\Delta P}} \tag{15}$$

$$\rho V = C_d\sqrt{2\rho\Delta P} \tag{16}$$

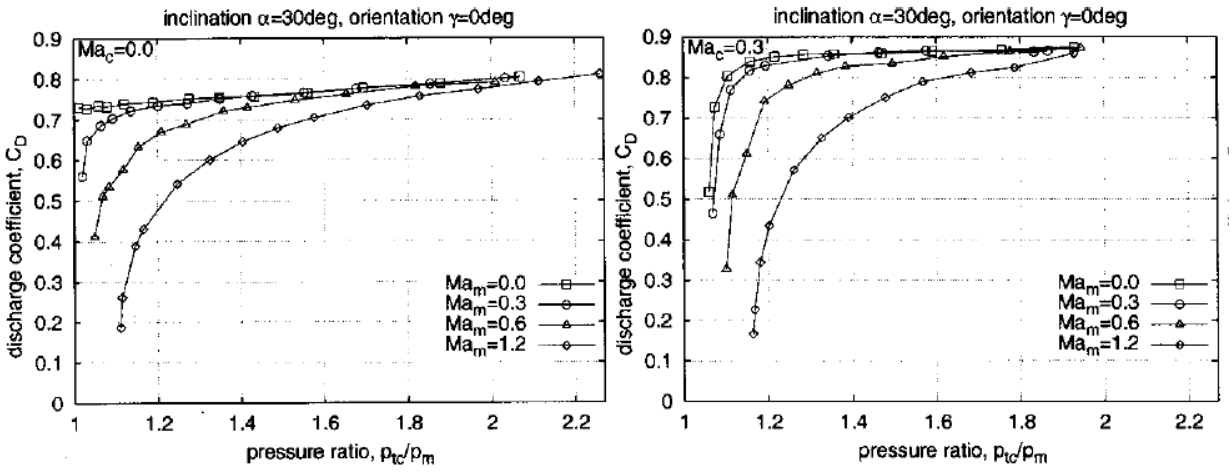

Figure 23: Discharge coefficients for a film-cooling hole at various freestream Mach numbers with coolant Mach number zero (left) and 0.3 (right) [32]

2.4.1 Passive Vane Cooling of HGV

As the heat release capacity of AFIT's UCC continues to develop, cooling of the HGV will become an important consideration. Bohan et al. [6] recognized the leading edges of the HGV were located upstream of the combustion cavity (Figure 24) and as such, if openings were placed at the stagnation region of the vanes, it would be possible to ingest cool core flow for internal and film-cooling. Three vane configurations were conceptualized: one that was completely hollow, one with a central plug that extended through the span of the vane, and one with a plug as in the second configuration, but positioned closer to the inlet. All configurations had a trailing edge slot and the resulting geometries can be seen in Figure 25. Suspecting that the vane internal to external pressure differential would vary with chord length, but not the magnitude of the difference, film-cooling holes were placed in pairs along the vane surface as seen in Figure 26 to assess where outward coolant flow would be possible.

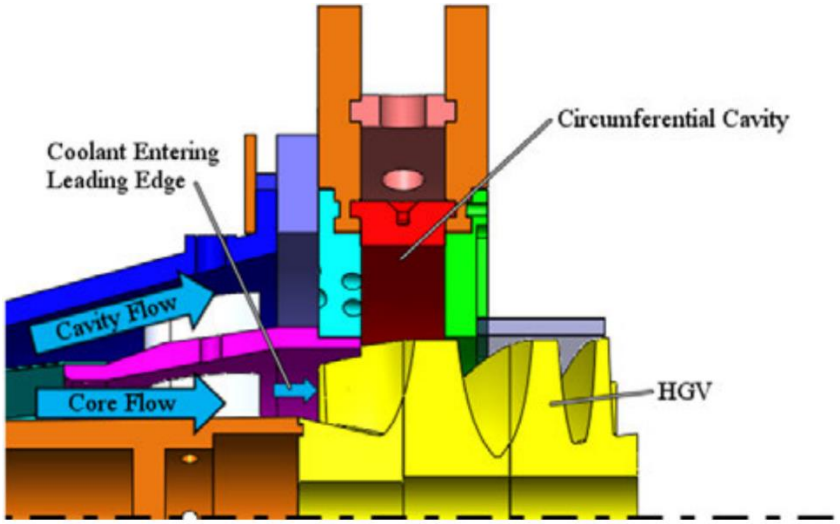

Figure 24: Cross section of AFIT's UCC detailing HGV leading edge location [5]

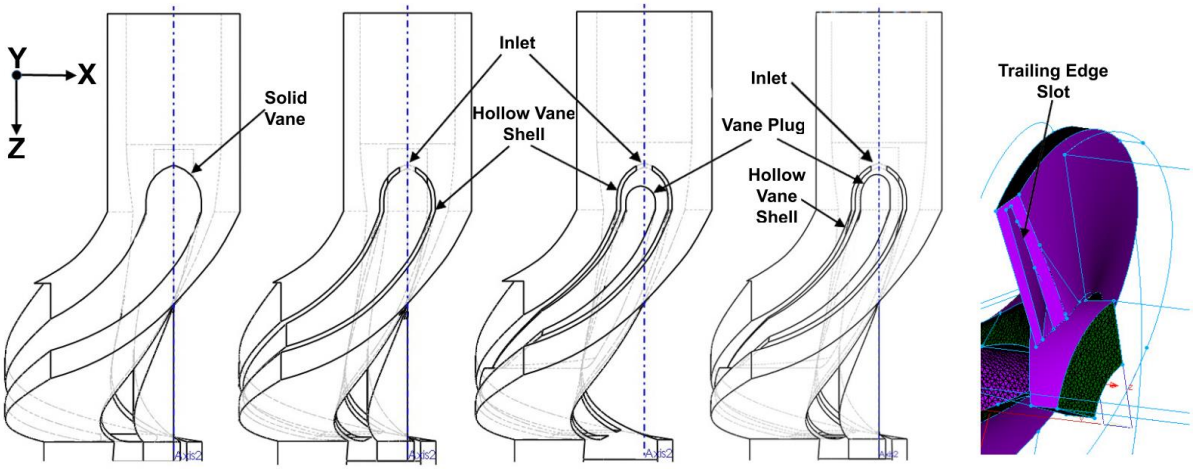

Figure 25: Cooled HGV configurations [6]

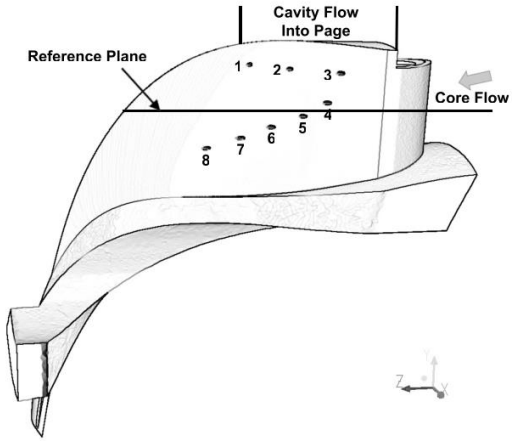

Figure 26: Film-cooling hole placement on cooled HGV [6]

Using CFD, Bohan et al. [6] evaluated the various cooled vane configurations to determine vane pressure distributions, mass flow rates through the vane, and temperature distributions on the vane surface. Of the various internal geometries considered, the vane with an internal plug, and exit slot with an area equal to 56% of the inlet area produced the necessary internal pressure rise for film-cooling in the least amount of axial distance. Figure 27 shows the pressure distribution for this case indicating at approximately 50% chord length the requisite pressure differential existed for film-cooling. This configuration allowed 22% of the core flow to travel through the vane. Temperature distributions across the cooled vane were on average lower compared to the solid vane. The portion of the vane situated within the circumferential combustor experienced the hottest temperatures, but was still lower than the solid vane as seen in Figure 28.

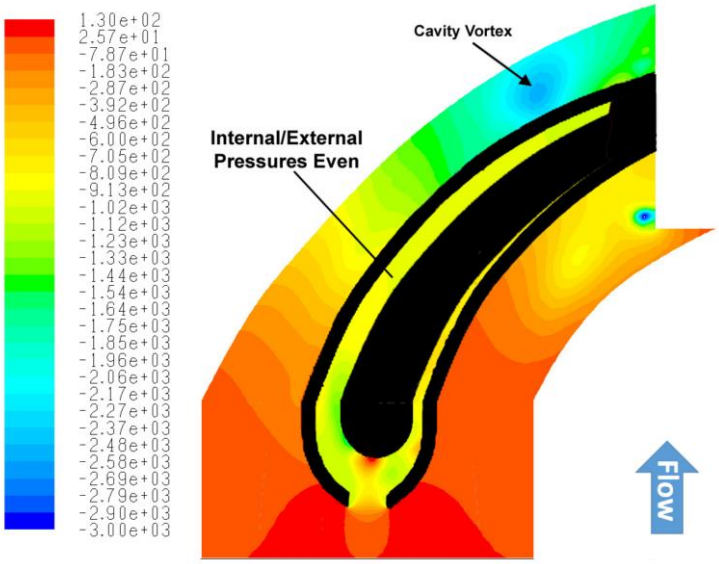

Figure 27: Pressure in and around the hollow vane with internal plug [6]

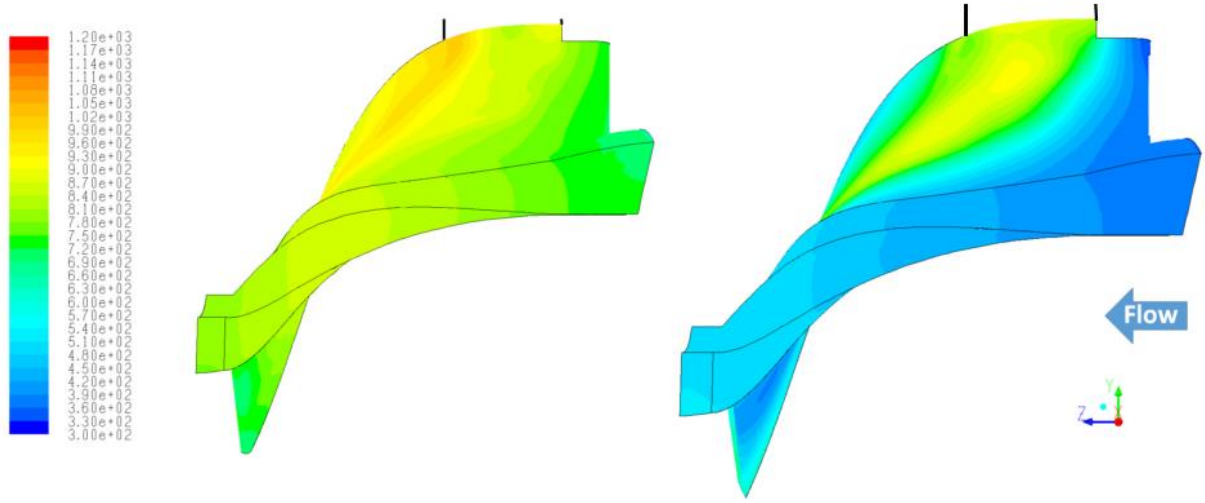

Figure 28: Surface temperature distribution on the solid vane (left) and cooled vane with internal plug (right) [6]

DeMarco et al. [7] built a cooled HGV based on the findings of Bohan et al. [6] that was composed of five cooled vanes and one solid vane. While each cooled vane was different, they shared similar features enabling the impact of several internal geometry and film-cooling designs to be examined. Table 1 details the variations of the design parameters for each vane configuration. Vanes E, A, and C all employed film-cooling with varying exit areas of 0.587 cm^2, 0.487 cm^2, and no trailing edge slot respectively. Vane D had the same geometry as Vane E, with the exception of no film-cooling holes. Lastly, Vane B had the same geometry as Vane D, but with the internal plug positioned closer to the vane inlet.

Table 1: Variations in cooling schemes for the experimental HGV [7]

Vane	Plug Distance (mm)	Cooling Holes	Exit Area (cm^2)
A	5.84	Yes	0.477
B	2.29	No	0.587
C	5.84	Yes	None
D	5.84	No	0.587
E	5.84	Yes	0.587
S	N/A (Solid Vane)		

All of the film-cooled vanes used 0.508 mm diameter holes with a cooling hole configuration as shown in Figure 29. Percent radial span and axial chord were used by DeMarco et al. [7] as non-dimensional means of measuring hole location. These values represent the ratio of the hole's distance from the axis of revolution to the total radius of the HGV and the ratio of the hole's downstream axial length from the leading edge of the vane to the vane's total axial length, respectively. A more common practice for reporting features on an airfoil is to use percent airfoil span (the location of the feature as measured from the inner radius of the airfoil divided by the total width of the airfoil). Hole 1 was located at the 87% radial span. The next six holes were placed in pairs at the same axial distance and at 87% and 60% radial span. Next, a row of six cooling holes were placed at 87%, 82%, 76%, 70%, 64% and 60% radial span, which corresponds to 79%, 68%, 56%, 45%, 34% and 23% airfoil span, and 86% axial chord. Lastly, a final pair of cooling holes were located at 87% and 60% radial span. The airfoil had an axial location dependent width, which will be discussed in detail in Section 3.1. To simplify discussion the percent airfoil spans were calculated at the row of film-cooling holes and the pairs of coolant holes were stated as having the same percent airfoil span as the inner and outer most coolant holes from that row.

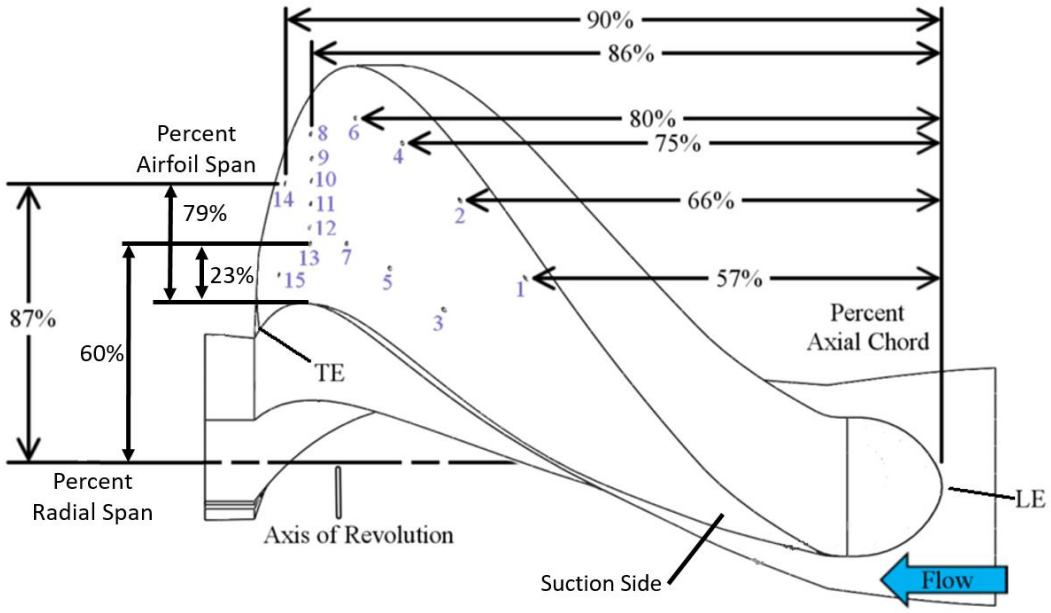

Figure 29: Film-cooling hole location on experimental HGV [7]

DeMarco et al. [7] positioned film-cooling holes to assess the impact on vane internal to external pressure difference. As such, the holes employed were not intended to be ideally positioned for surface cooling, but were spread out to cover more of the surface. They chose a Pitch Spacing, *P/D*, of 6 for the row of six film-cooling holes, limiting the coverage area for these jets. Therefore large surface temperature reductions were not expected.

Additive manufacturing was chosen as the means to build the experimental hardware, but required the addition of internal support material for fabrication. As such, 2 mm diameter pins spaced 3 mm apart were placed internally as seen in Figure 30. DeMarco et al. [7] then used CFD to investigate the impact of the added support material on vane cooling, choosing to limit the scope of their investigation to variations of Vane A from Table 1. The specific test conditions are shown in Table 2. Their computational domain consisted of a 60° sector model of AFIT's UCC, employing the stepless outer ring with radial fuel injection and 8 of the 48 holes in the air injection plate, and was evaluated at the flow conditions listed in Table 3.

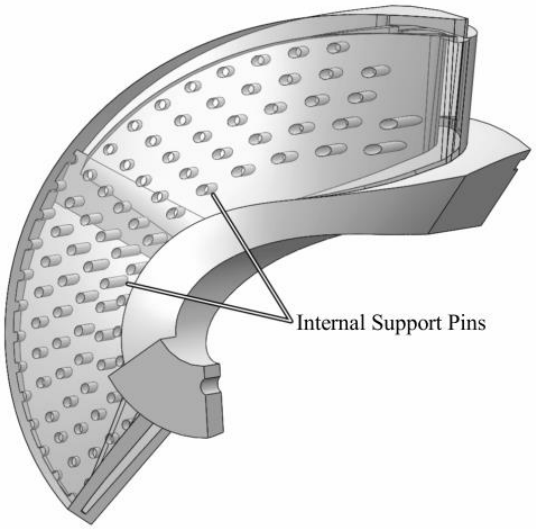

Figure 30: Support material placement for additive manufacturing [7]

Table 2: Variations on Vane A geometry computationally analyzed [7]

Case	Plug Distance (mm)	Cooling Holes	Exit Area (cm^2)	Internal Structure
1		Solid Vane		
2	5.84	No	0.477	No
3	5.84	Yes	0.477	No
4	5.84	Yes	0.477	Yes

Table 3: Inlet conditions for the computational domain modeling 60° of the combustor [7]

Boundary	Mass Flow (kg/s)	Gauge Total Pressure (Pa)
Cavity Air Inlet	0.0054	4800
Core Inlet	0.0126	4800
Fuel Inlet	0.00025	5200

Numeric results indicated the addition of support material caused a more rapid pressure rise, shifting the location of greater internal to external pressure (a necessary trait for film-cooling) upstream by 15% axial chord. However, by the trailing edge slot, the pressure differential was less for the vane with support material compared to that without. The pressure as a function of axial chord location is shown in Figure 31 with the location of cooling holes denoted.

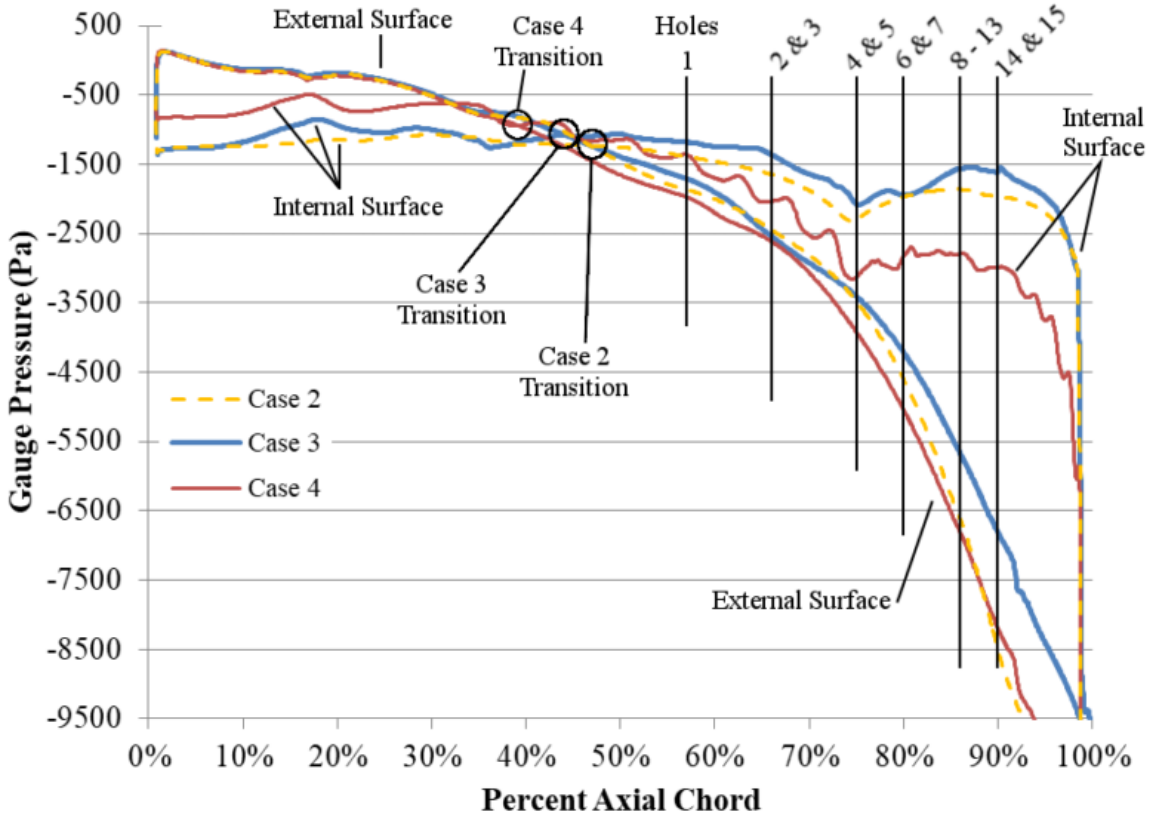

Figure 31: Pressure distribution as a function of axial location for three variations of Vane A geometry [7]

For the angled cylindrical cooling holes employed, Bogard [29] states a blowing ratio of 0.6 is most effective, with a significant drop in effectiveness occurring at 0.85. DeMarco et al. [7] determined the blowing ratio at the 15 film-cooling holes, shown in Table 4, and found values for all cases were on average larger than desirable. With no support pins, the resulting average *M* was 0.86, while for the case with the internal support pins the average *M* was 0.72. The reduced blowing ratio with an internal structure was due to a lower average pressure differential.

Table 4: Blowing ratio of film-cooling holes for test Cases 3 and 4 [7]

Hole	Percent Axial Chord	Percent Radial Span	Case 3 Blowing Ratio	Case 4 Blowing Ratio
1	57%	87%	0.66	0.62
2	66%	87%	0.64	0.44
3	66%	60%	0.85	0.68
4	75%	87%	0.65	0.45
5	75%	60%	0.75	0.54
6	80%	87%	0.69	0.67
7	80%	60%	0.80	0.94
8	86%	87%	0.74	0.60
9	86%	82%	0.96	0.73
10	86%	76%	1.03	0.80
11	86%	70%	1.07	0.86
12	86%	64%	0.93	0.97
13	86%	60%	1.10	0.84
14	90%	87%	0.81	0.73
15	90%	60%	0.85	0.89

Using the unreacted air temperature of 300 K as the coolant temperature and the peak combustion temperature of 2200 K as the freestream temperature, overall effectiveness was calculated by DeMarco et al. [7] and can be seen in Figure 32. The greatest surface temperature existed at the interface of the vane with the combustion cavity which then extended axially downstream as a hot streak. On the solid vane, the hot streak extended axially downstream moving initially towards the inner radius until changing paths toward the outside radius near the trailing edge. The film-cooled vane experienced the same initial hot streak movement until the row of six cooling holes which had the effect of pushing the hot streak to the outer radius. The support material for additive manufacturing served as pin fins and transferred energy from the suction surface to the coolant and subsequently to the pressure side of the vane. This conduction path resulted in an average coolant exit temperature increase of 190 K from the vane inlet temperature.

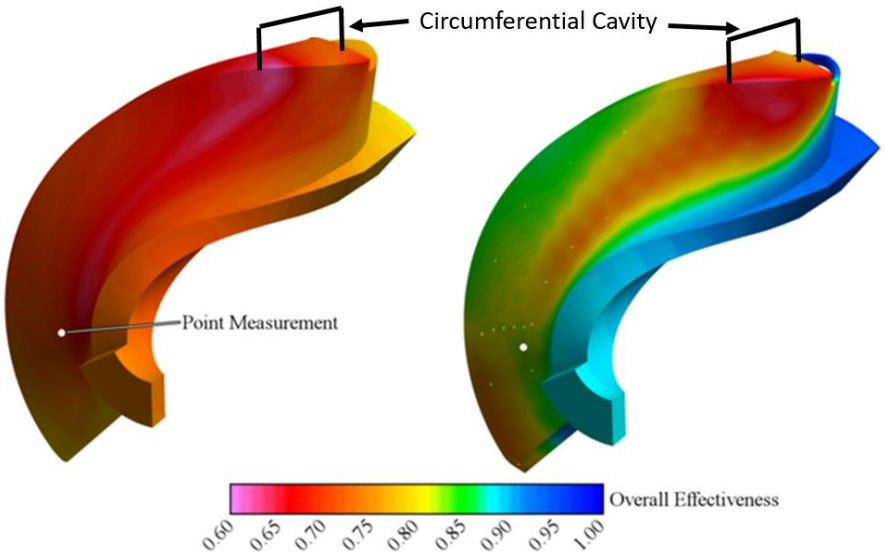

Figure 32: Overall cooling effectiveness for Case 1 and 4 [modified from 7]

Their completed part can be seen in Figure 33. Bohan [33] then experimentally validated the computational results of DeMarco et al. [7] using thermocouples, pressure transducers and Infrared (IR) thermography (which will be discussed in greater detail in Section 2.5) to compare Vane A and Vane S. Thermocouple data confirmed the effectiveness of the cooling scheme as temperatures were consistently lower on Vane A compared to Vane S. Temperatures predicted by CFD were greater for Vane S and lower for Vane A which Bohan attributed to 3D printing variations from the modeled geometry caused by expansion joints in the physical hardware, variation in material properties from the numeric model, and discrepancy in flow conditions. This last issue is a result of using a periodic computational domain which simulates six identical vanes which differs from the manufactured HGV that consists of six different vanes. The vane internal pressure change from the stagnation region of the inlet to the pressure reading at 85% axial chord distance matched CFD within approximately 5%. Comparing vane passage pressure was more difficult as the measurement location varied between the two analysis methods. As such the values

did not compare well, but experimental values were consistently lower than internal pressure validating the possibility of film-cooling. IR thermography data was not usable as damage to the emissive treatment applied to the surface, shown in Figure 34, resulted in significant variation in surface emissivity. To continue to advance the HGV cooling designs, the performance of all five vane configurations must be analyzed. As such, resolving the emissive treatment failure and collecting IR thermography, pressure, and thermocouple data on all five vane configurations is a goal of the present investigation.

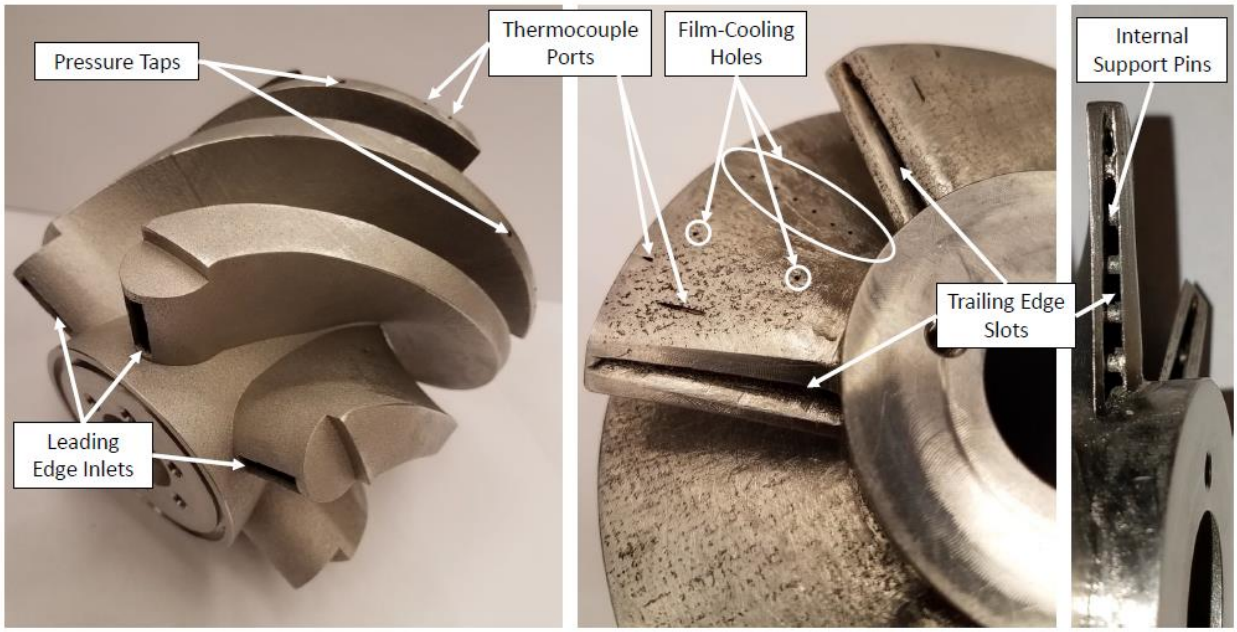

Figure 33: 3D printed cooled HGV [33]

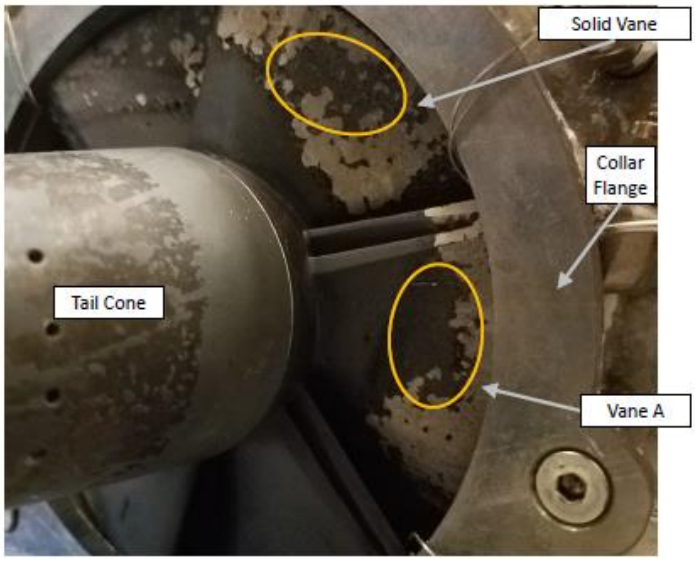

Figure 34: Paint failure on HGV trailing surface [33]

2.5 Infrared Thermography

Infrared (IR) thermography is an unobtrusive surface temperature measurement technique that was needed to quantify the effects of the passive cooling schemes for the HGV. It employs a standard camera configuration with a photodetector capable of detecting IR electromagnetic radiation to optically image a surface, resulting in high spatial resolution thermal data [34]. The camera's lens is used to collect, focus, and collimate light onto the detecting element (a two-dimensional detector matrix). A common type of detector is the photodetector which relies on the incoming photon's energy to liberate electrons which can be directly measured. Photodetectors provide very high sensitivity and quick response time, but only if the correct detector material is chosen. A very common selection is mercury cadmium telluride (HgCdTe) due to its economy, ability to detect in both the mid and longwave infrared spectrum, high quantum efficiency (incident photon to converted electron ratio), and ability to operate at a temperature attainable through thermoelectric cooling [35]. Most cameras have a fixed photodetector; therefore, it is important to

know what wavelengths, λ, are of interest to the user prior to selecting a camera as detectivity for a given detector is highly dependent on wavelength as shown in Figure 35.

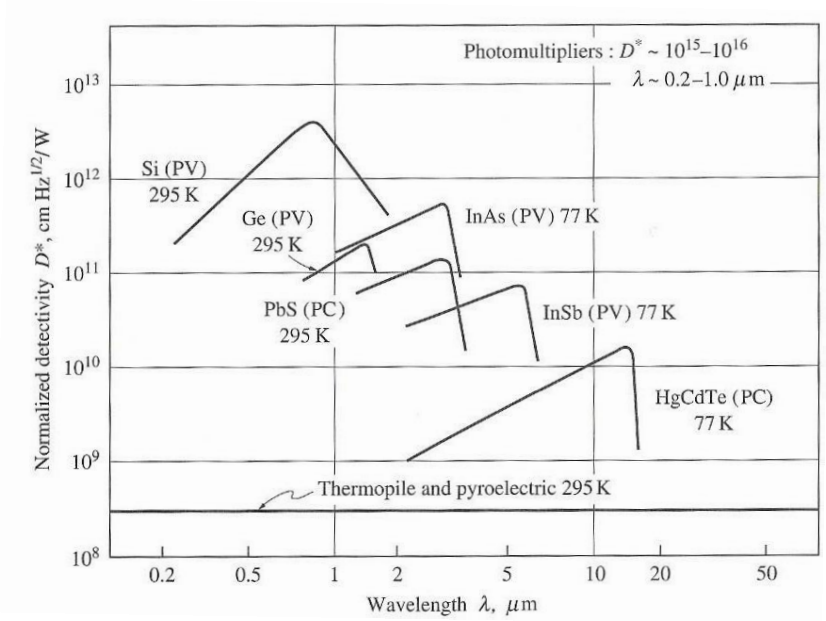

Figure 35: Photodetector detectivity versus wavelength [34]

The net energy reaching the camera is a function of the emission of the imaged object, reflections off of the imaged object from other emitting surfaces, and emissions from the gases between the object and the photodetector. Emissions from the object's surface, *E*, can be described with Planck's Law for a greybody given in Equation 17 with constants defined in Equations 18 and 19, where h is Planck's constant, k is Boltzmann's constant, and C_0 is the speed of light in a vacuum.

$$E_\lambda = \frac{C_1}{\lambda^5(\exp\left(\frac{C_2}{\lambda T}\right) - 1)} \tag{17}$$

$$C_1 = 2\pi h c_0^2 = 3.742 * 10^8\ Wm^3 \tag{18}$$

$$C_2 = \frac{hc_0}{k} = 1.439 * 10^4\ mK \tag{19}$$

Reflections from an object's surface are difficult to characterize as their intensity is a function of both the surface of interest and the surroundings. Kirchhoff's Law of Thermal Radiation states that for a gray diffuse surface, emissivity is equal to absorptivity meaning the higher the emissivity of a surface, the less it will reflect. While investigating paint applications to alter emissivity, Coblentz and Hughes [36] found that the application of surface coatings could effectively be used to change the surface's emissivity and reflectivity thereby maximizing or minimizing said property as desired.

Emissions from and absorption by the gases between the camera and surface being imaged can distort or block the emissions from the desired surface. Exemplifying this is a case study provided by FLIR, a large manufacturer of IR cameras, where one of their clients wanted to image the interior of a furnace while in operation [37]. The various combustion reactions occurring between the furnace wall and the camera entirely obscured the desired area as seen in the left image of Figure 36. FLIR capitalized on the fact that the furnace wall's emissions approximate a greybody, that is they emit over a broad spectrum with a peak emission wavelength driven purely by temperature, while the combustion reactions emitted at discrete wavelengths based on their chemical composition and temperature. By applying an optical bandpass filter that blocked the specific wavelengths associated with combustion, only the furnace emissions reached the camera as shown in the right hand image of Figure 36.

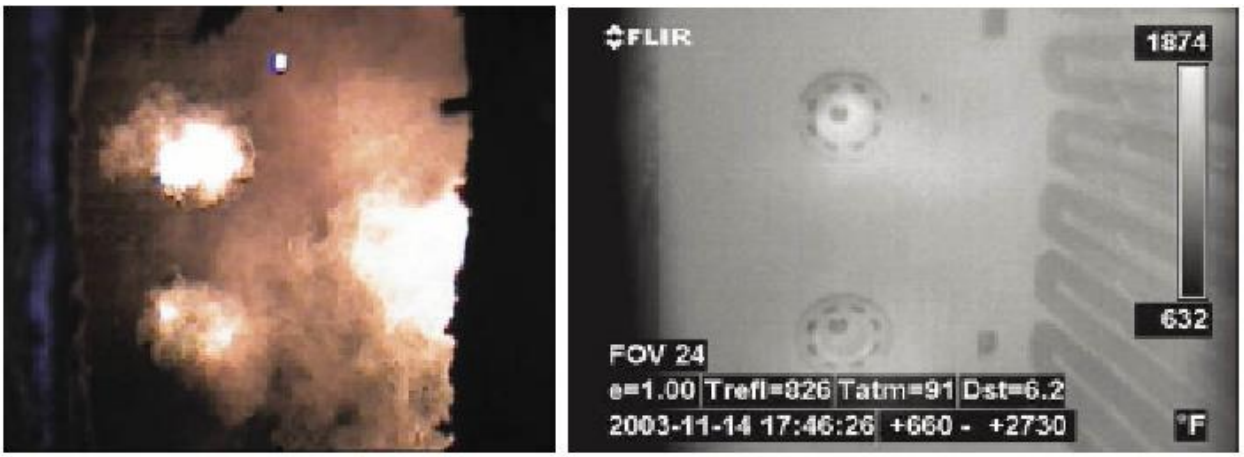

Figure 36: IR image without (left, converted to GRB color) and with flame filter (right) [37]

To gain optical access to a combustion environment, a window is employed to allow the desired electromagnetic radiation to pass through. Transmissivity of a material is dependent on wavelength, meaning that while common glass may appear clear in the visible spectrum, at other wavelengths it is opaque. As such, quartz or sapphire are commonly employed as both materials are transmissive in the visible and near visible wavelengths where substantial combustion energy is emitted. Details on the transmissivity of fused quartz can be seen in Figure 37.

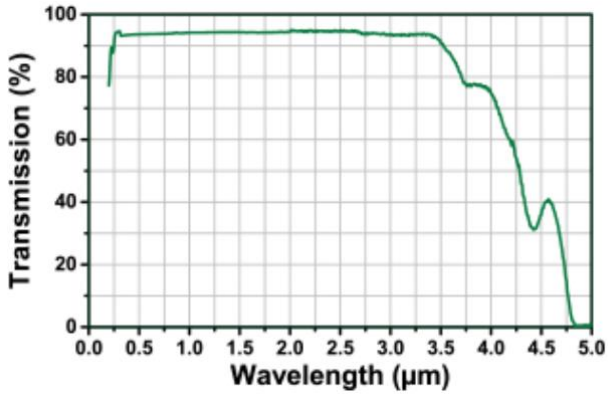

Figure 37: Fused quartz transmittance versus wavelength [38]

To obtain a temperature measurement from an IR image, a method to correlate the electromagnetic intensity received by the camera to a temperature at the surface is needed. Martiny et al. [39] proposed in situ calibration, where thermocouples are placed on the imaged surface and

in view of the camera, providing the connection between the optical measurement and temperature. Vorgert [40] applied this calibration method to correlate the fourth order emissive behavior of the interrogated surface to camera "counts," or unitless measurements of photodetector excitation.

2.6 Chemiluminescence Imagery

Chemiluminescence Imagery (CI) was employed to characterize the flame movement and location within the circumferential cavity to understand the objective of what parameters resulted in the higher UCC exit temperatures. It is an optical analysis technique where the electromagnetic emission of molecules as they undergo a chemical, or energy level change, are recorded. This process can be leveraged for combustion diagnostics by applying a bandpass filter to a camera to observe the emissions of specific molecules. OH radicals are commonly observed as they indicate locations of chemical reactions and have a peak intensity at a wavelength of 308 nm. CH radicals, with a peak intensity at 431 nm, are also of interest and indicate the boundaries of a flame. Dr. Larry Goss of ISSI created a post-processing technique that tracks these natural emissions as they move across a fixed reference frame allowing two dimensional flame velocity to be determined. His program identifies strongly luminescing particles and tracks them through successive frames resulting in flame velocimetry data. This process is nearly identical to particle image velocimetry, a well-established flow field measurement technique, which is thoroughly described by Adrian [41]. Critical to this analysis is the assumption that luminance intensity is one dimensional (does not vary with depth) and camera speed is much faster than the turbulent flame speed. The later requirement is achieved by ensuring particle movement does not exceed seven pixels of movement between frames. Bohan et al. [27] employed CI to determine flame velocity and luminance frequency in a portion of a circumferential cavity as discussed in Section 2.3.

Critical to tracking luminescing particles is the ability to isolate them from the background image. This is done with a Laplacian convolution filter, which is the 2nd spatial derivative of an image. This process highlights regions of rapid change and which, in the case of CI, are luminescing particles traveling through the flow field [42]. Equation 20 shows the general form of the Laplacian for an image with pixel intensity *I(x, y)*.

$$L(x,y) = \frac{\partial^2 I}{\partial x^2} + \frac{\partial^2 I}{\partial y^2} \tag{20}$$

The convolution filter is the means by which the Laplacian is calculated and consists of the monochromatic image of interest and a much smaller "kernel," both of which can be seen in Figure 38. The kernel is overlain on the image, the aligned cells are multiplied, and then each of the resulting values are summed, creating a value for that kernel placement. A sample depicting this calculation when the kernel is placed in the bottom right of the image can be seen in Equation 21. The kernel is then moved over the image such that it resides in every position where it entirely overlaps the image. If the image has *M* rows and *N* columns and the kernel has *m* rows and *n* columns, the values from the convolution will form an (M-m+1) by (N-n+1) matrix.

I_{11}	I_{12}	I_{13}	I_{14}	I_{15}	I_{16}	I_{17}	I_{18}	I_{19}
I_{21}	I_{22}	I_{23}	I_{24}	I_{25}	I_{26}	I_{27}	I_{28}	I_{29}
I_{31}	I_{32}	I_{33}	I_{34}	I_{35}	I_{36}	I_{37}	I_{38}	I_{39}
I_{41}	I_{42}	I_{43}	I_{44}	I_{45}	I_{46}	I_{47}	I_{48}	I_{49}
I_{51}	I_{52}	I_{53}	I_{54}	I_{55}	I_{56}	I_{57}	I_{58}	I_{59}
I_{61}	I_{62}	I_{63}	I_{64}	I_{65}	I_{66}	I_{67}	I_{68}	I_{69}

K_{11}	K_{12}	K_{13}
K_{21}	K_{22}	K_{23}

Figure 38: An example image (left) and kernel (right) for a convolution filter [42]

$$O_{57} = I_{57}K_{11} + I_{58}K_{12} + I_{59}K_{13} + I_{67}K_{21} + I_{68}K_{22} + I_{69}K_{23} \tag{21}$$

As the Laplacian convolution filter is evaluating gradients in the image, it can be very sensitive to noise. As such a Gaussian filter is often first applied to smooth the image. Given that the convolution operation is associative, the Gaussian smoothing filter can be convolved with the Laplacian filter, resulting in a hybrid filter termed "Laplacian of Gaussian" or LoG. In application, the LoG will produce no response in a constant intensity image, a positive value in a dark to light transition, and a negative value in light to dark transition. Figure 39 shows the LoG response at the step junction between two uniform, but different, intensity regions. Values for this are: zero at the long distance as no gradients are present, positive approaching the step, zero near the middle of the step, and negative leaving the step.

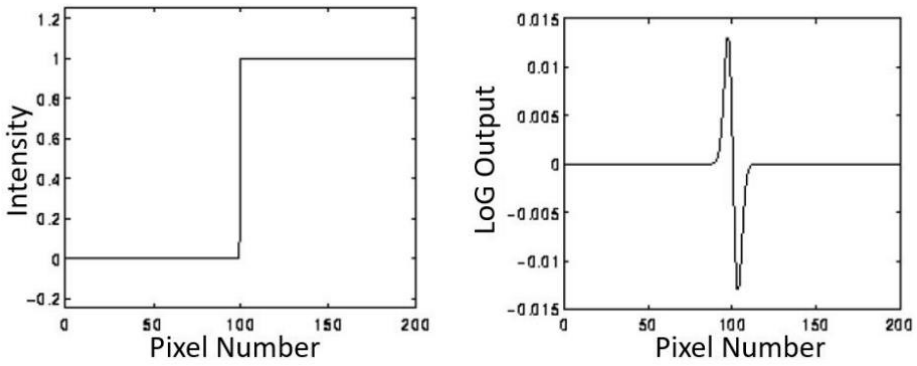

Figure 39: LoG filter response (right) to an intensity step (left) with Gaussian σ=3 pixels [42]

Once the LoG filter has been applied, an image cross correlation technique is applied to determine the flow velocity. This technique compares sequential video frames using statistical methods that results in a signal peak identifying the particle displacement. Accuracy of the resulting data is dependent on particle size and displacement between frames.

III. Methodology

AFIT's UCC was tested in the Combustion Optimization And Laser (COAL) laboratory using a variety of point and optical measurements to further investigate passive cooling of the HGV and flow dynamics within the circumferential cavity. This chapter details the UCC experimental configuration that was used for testing (Section 3.1), the supporting experimental facilities (Section 3.2), operation of the UCC and the data acquisition process (Section 3.3), unique instrumentation that was used to evaluate the cooled HGV (Section 3.4), and setup of the optical tools used to investigate cavity flow physics (Section 3.5).

3.1 UCC Experimental Configuration

In order to collect data on the five cooled HGV configurations and circumferential cavity flame dynamics, AFIT's UCC was employed which can be seen in Figure 40. Air entered the UCC from the left hand side of the image and went into the variable diffuser designed by Bohan et al. [26] which slowed the fluid and split the airflow between two paths. Airflow located towards the inner radius, referred to as core flow, traveled directly into the passages of the HGV which was located in the center of, and extended axially up and downstream from the combustion cavity. Airflow on the outer radius of the diffuser, referred to as cavity flow, traveled through the air injection plate which had 24 holes arrayed circumferentially around the combustor's central axis. Airflow exiting the air injection plate entered the circumferential cavity, which was 2.54 cm in axial length, 3.74 cm outboard of the HGV tips, and 17 cm in diameter. Additional air and fuel were introduced through the 12-Step outer ring and the resulting flow burned in the circumferential cavity while rotating with an axis of rotation coaxial to the centerline of the combustor. After

progressing radially inward to the HGV, this mixture then entrained into the core flow, traveled through the vane passages, and exited into the exhaust enclosure.

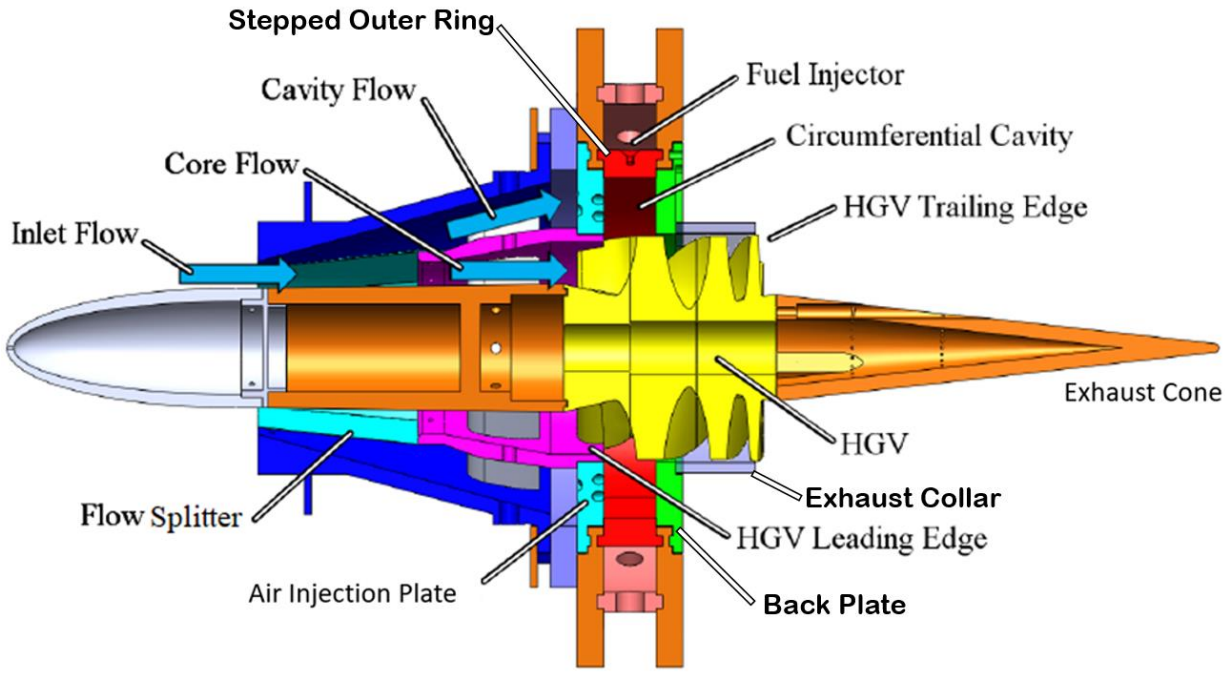

Figure 40: AFIT's UCC experimental hardware [adapted from 8]

3.1.1 Variable Position Diffuser

The variable position diffuser designed by Bohan et al. [26] relied on a pressure differential to generate the flow split between the core and air injection plate. Mechanically, the variable position flow splitting mechanism used eight pushrods driven by a common actuation assembly to open or close overlapping metal "feathers" which can be seen in Figure 41 and Figure 42. For digital control, a Raspberry Pi Model 2 was used to generate g-code, which was sent to an Arduino to convert into grbl language, which a grblShield then converted to electric pulses to move a stepper motor connected to the driving belt shown in Figure 42.

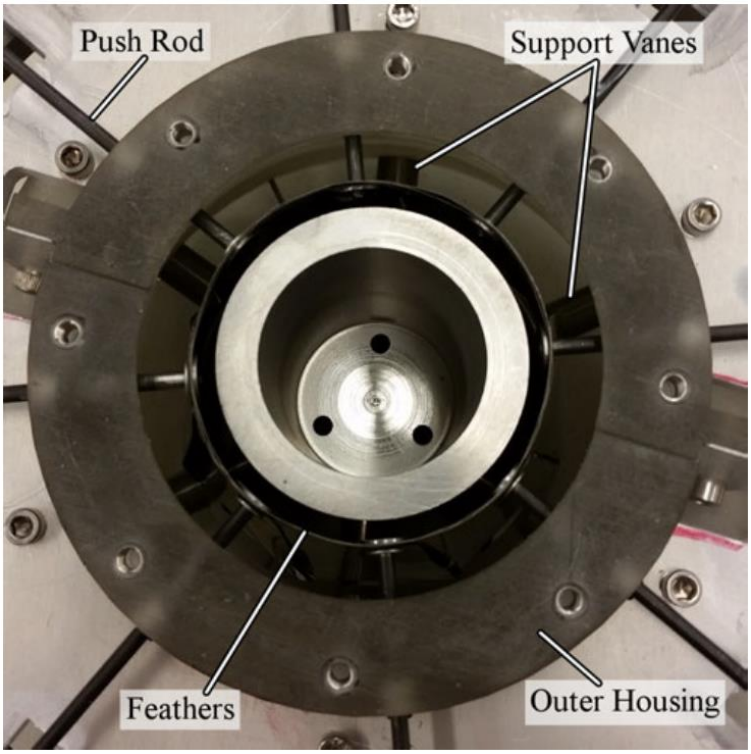

Figure 41: Variable position diffuser [33]

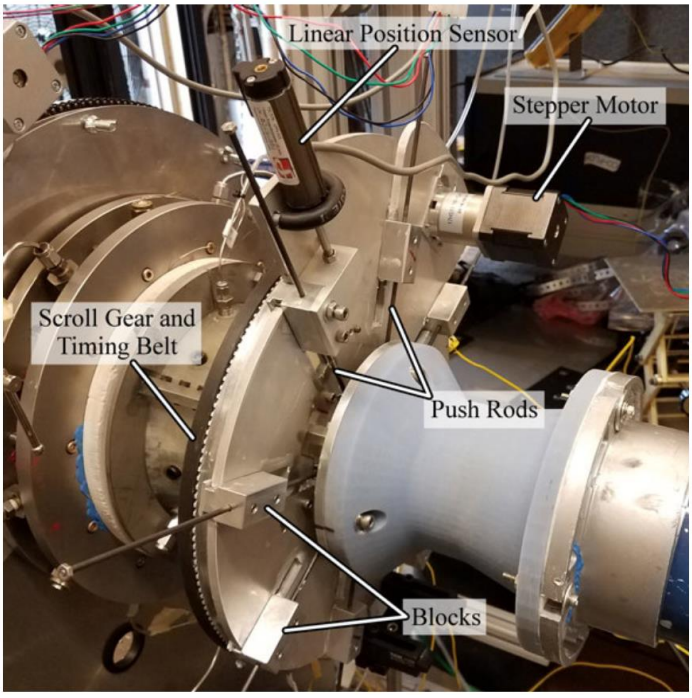

Figure 42: Variable position diffuser installed with external hardware detailed [8]

The differential between static and total pressure of the core flow was measured and used to determine the diffuser position required to achieve the desired air mass flow split. This was calculated by first determining the average core velocity required to achieve a specific core mass flow using Equation 22 where $\overline{U}_{core}$ is the average core velocity, $\dot{m}_{core}$ is the desired core mass flow, ρ is the core air density, and A is the core cross sectional area.

$$\overline{U}_{core} = \frac{\dot{m}_{core}}{\rho A} \tag{22}$$

Next, the required velocity at an interior mounted pitot tube was determined using a fully developed turbulent profile assumption and Equations 23 and 24, where U is the velocity of the airflow at the pitot probe, U_τ is the friction velocity (found using Equation 24), κ is the Von Karman constant (= 0.41), y is the half height of the channel, ν is the kinematic viscosity of air, and B (= 5.2) is the log-law constant.

$$\frac{U - \overline{U}_{core}}{U_\tau} = \frac{1}{\kappa} \tag{23}$$

$$\frac{U}{u_\tau} = \frac{1}{\kappa} ln\left(\frac{y u_\tau}{\nu}\right) + B \tag{24}$$

Bernoulli's equation, Equation 25, then provided the pressure differential required to achieve $\overline{U}_{core}$.

$$\Delta P = \frac{\rho \overline{U}^2{}_{core}}{2} \tag{25}$$

As solving these sets of equations in real time was challenging for the digital control system employed, a MATLAB script was created by Bohan [33] which allowed the user to input the

incoming air mass flow rate and then calculated the necessary pressure differentials for a variety of airflow splits. The diffuser position was then adjusted until the required pressure differential was achieved. Given that the diffuser achieved flow splits based on a pressure differential, certain combinations of mass flow, flow splits, and combustion dynamics resulted in unattainable diffuser positions. A sample of this region for a given total mass flow can be seen in Figure 17 as the light blue section.

3.1.2 Circumferential Cavity

The circumferential cavity was the primary combustion zone that housed the rotating flame and can be seen in Figure 43. The front of the cavity was formed by the air injection plate which had 24, 0.493 cm diameter, holes angled 55° relative to the combustor's primary axis, imparting a tangential velocity component to the flow, and a 10° radially outward component. The outside perimeter was formed by the 12-Step outer ring, which was shown in Figure 16, that introduced fuel and air tangentially. Fuel for the 12-Step outer ring came through 12 fuel plugs threaded through the outside diameter and air entered through a plenum created between the 12-Step outer ring and a large exterior ring. The fuel and air mixture then rotated in the circumferential cavity with an axis of rotation coaxial to the centerline of the engine, combusting and moving radially inward towards the HGV. Once the flow reached the HGV, it was entrained into the core flow, and exited the UCC. The rear of the cavity was formed by the back plate.

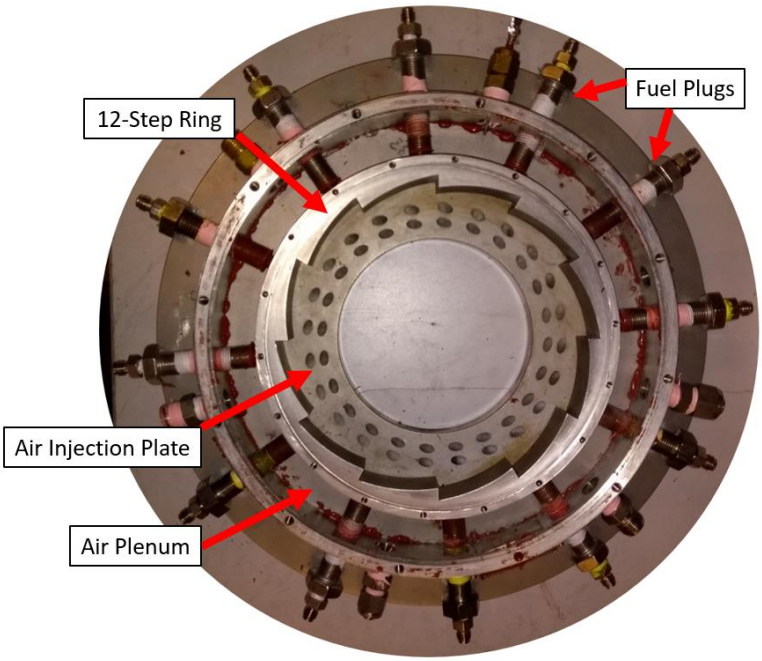

Figure 43: Circumferential cavity with back plate and HGV removed

3.1.3 Hybrid Guide Vane

A 10.16 cm long HGV composed of six vanes wrapped around a solid center body was positioned central to the circumferential cavity. This component served as a secondary combustion zone and altered the flow exhaust angle. Two HGV configurations were used for this study, one with all solid vanes, shown in Figure 45, that was used for the CI study as part of Objective 2. The other HGV contained six different vanes with various cooling arrangements to answer Objective 1. This vane was shown in Figure 33 and will be discussed in greater detail in Section 2.4.1. All vanes were based on a common exterior geometry. The solid center body the vanes were wrapped around had a diameter of 6.09 cm at the front, 5.08 cm at the rear, with a curved radius reduction in the center as shown in Figure 45. This profile was intended to slow the flow in the vane passages while transiting the circumferential cavity to reduce the Rayleigh losses. The six vanes wrapped 160º around this solid center with an axial chord length of 8.89 cm and a maximum thickness of

3.18 cm. An exhaust cone was attached to the downstream center of the HGV to lessen the geometric change at the experimental combustor exit as shown in the side view of Figure 44.

Figure 44: Solid HGV geometry [5]

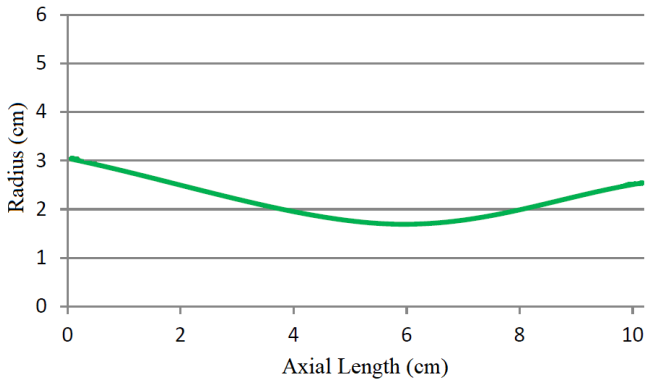

Figure 45: HGV center body radius (modified from [43])

3.1.4 Exhaust System

An exhaust system downstream of the UCC exit provided the necessary ventilation for experimental operation and Figure 46 details the initial configuration used. As many of the

experimental techniques required optical access to the trailing edges of the HGV, direct coupling of the exhaust system to the UCC was not possible. Instead, the UCC was placed in an enclosure that was fully sealed except for an opening above the test section. This configuration allowed the greater draw of the ventilation system (0.24 kg/s, nearly twice the flow rate through the UCC) to create a low pressure region inside the enclosure, ensuring all exiting combustion products were drawn into the exhaust system.

Figure 46: COAL lab initial exhaust enclosure and optical access point [33]

With the exhaust duct located in line with the exhaust cone on the UCC, optical access with the initial exhaust enclosure was limited to off-axis measurements only. This design was undesirable as it limited the amount of data that could be gathered from a single viewpoint. To correct this, the back wall of the exhaust enclosure was redesigned by extending it further downstream and then coupling the exhaust duct to the top of the enclosure as seen in Figure 47.

This enabled optical access coaxial to the UCC exit greatly improving the field of view. Optical access was obtained with a sapphire window (6.35 cm in diameter) for IR imaging and fused quartz (10.16 cm square) for CI for the reasons discussed in Section 2.5.

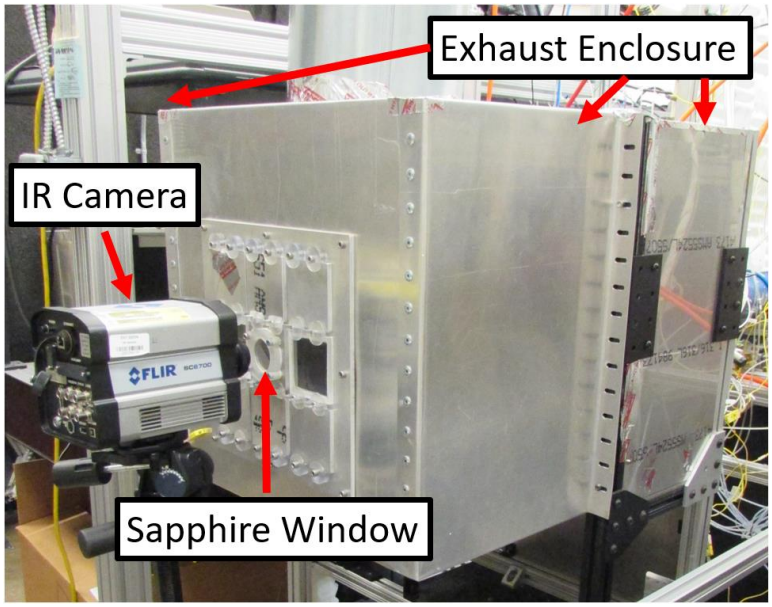

Figure 47: Reconfigured COAL lab exhaust enclosure and IR camera setup

3.2 Experimental Facilities

Data was collected from the UCC configuration described in Section 3.1 using the test facilities in AFIT's COAL laboratory. Air was supplied from a dedicated Ingersol Rand H50A-SD 50 hp compressor, equipped with an air dryer to remove moisture. Upon entering the lab, the air supply was split between a 7.62 cm, 3.81 cm, 1.91 cm, and an auxiliary line numbered one through four in Figure 48. A common AFIT air supply was also available, but not used as its flow capacity was variable depending on demand in other labs. Lines one through three were controlled, in order of flow path, by a manual ball valve, computer controlled pneumatic solenoid valve, and computer commanded mass flow controller (Flowserve MaxFlo 3 valve and FT2 Fox Thermal Instruments flow meter, respectively). The mass flow controller was commanded as a "percent of full scale" (i.e. a command of 20 would mean 20% of the mass flow controller's maximum flow

of 50 kg/min). A Eurotherm 2404 PID controller provided the interface between the flow meters and the LabVIEW experimental system control. The auxiliary airline supplied an MKS flow meter used for ignition air.

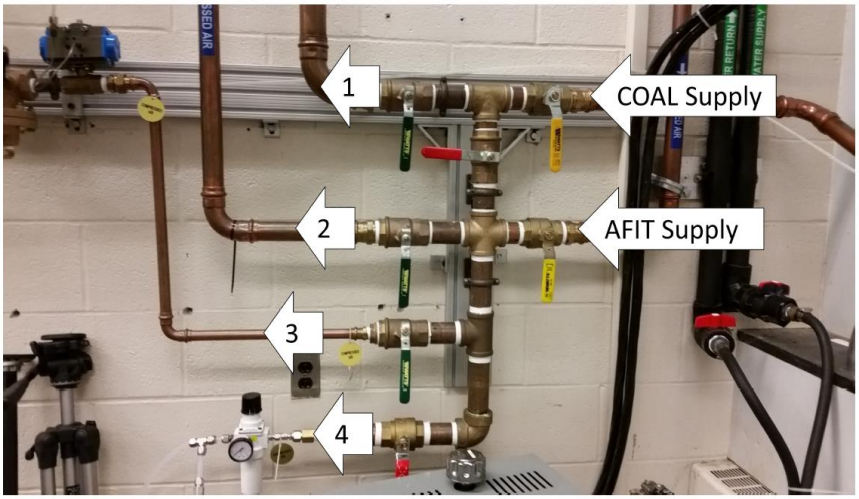

Figure 48: COAL lab initial air distribution system [33]

Two types of fuel were used during testing: ethylene and propane. Ethylene was only used as part of the startup sequence during which two digital MKS type 647C controllers, one for each gas, sent 20 SLPM of air and 2.8 SLPM of ethylene past an automotive spark plug and into the circumferential cavity as shown in Figure 49. Propane was supplied from four 150 gal tanks (Figure 50) and was routed through two Zimmerman LPG electric heaters (Figure 51) to ensure vaporization prior to entering the building. An Alicat MCR-250SLPM-D-40X55 mass flow controller was integrated into the LabVIEW rig control Virtual Instrument (VI) and supplied fuel to the 12 fuel plugs feeding the 12 cavity steps.

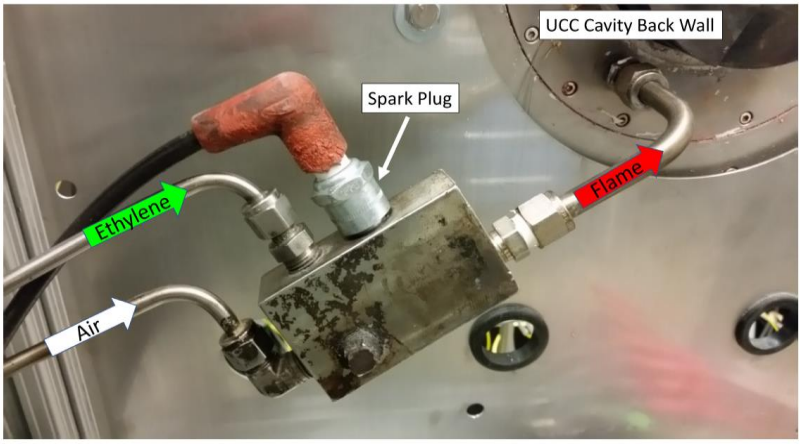

Figure 49: UCC ignition system [33]

Figure 50: COAL lab fuel facility [33]

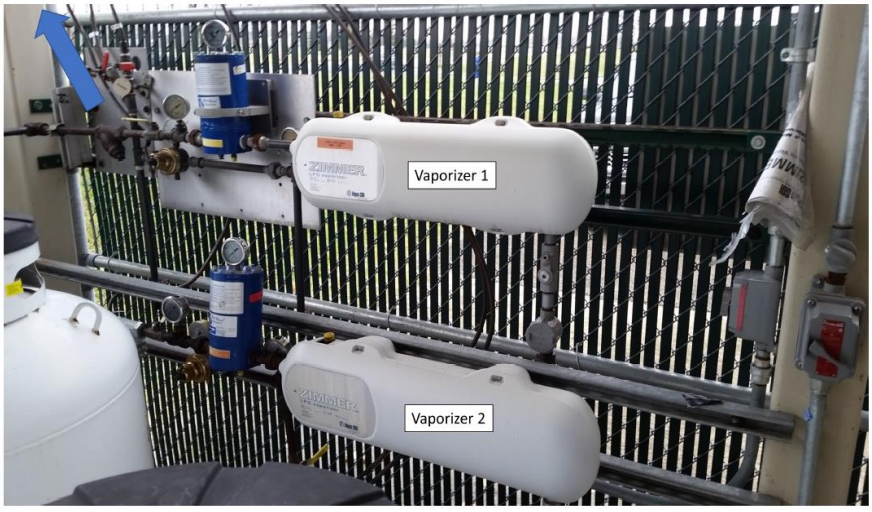

Figure 51: COAL lab fuel vaporizers [33]

During preliminary testing a 20% greater flow of air and ethylene was used for ignition, however, the momentum of the resulting jet was great enough to travel through the air injection plate and into the variable position diffuser. This eventually caused the plastic material used in the diffuser's construction to ignite, resulting in the damage shown in Figure 52. Two measures were taken to prevent a repeat occurrence of this phenomenon: first, the interior of the diffuser was coated with a thin film of two part epoxy rated for 150 °C, and secondly the flow rate of the igniter jet was reduced to the values mentioned in the previous paragraph to limit the igniter jet penetration.

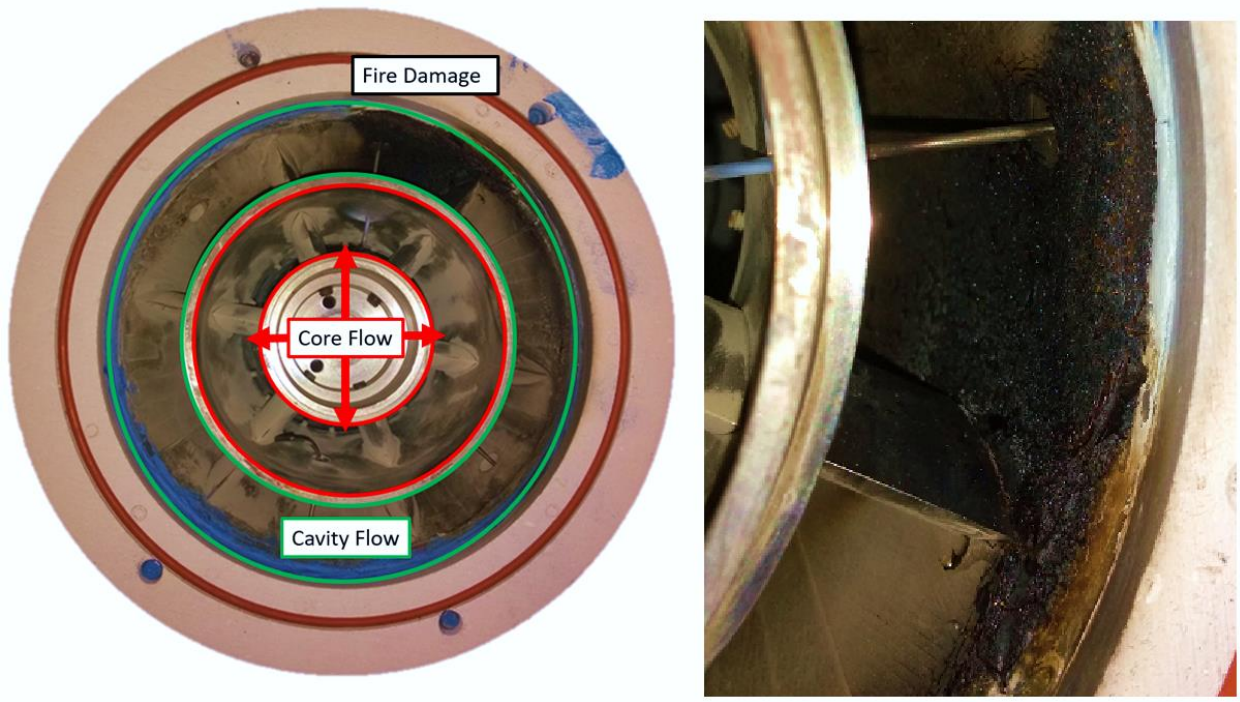

Figure 52: Fire damage from ignition jet viewed from the downstream side of the diffuser

The 7.62 cm line was used as the primary air inlet to the UCC and the 3.81 cm line was initially used to supply air to the 12-step outer ring. For ignition the primary air inlet was set to 10% of full scale, step air was set to 1% of full scale, fuel flow was set to 20 SLPM, and the

diffuser was opened to 2.5 mm. Once combustion stabilized, the flow parameters were incrementally changed until the desired operating conditions were achieved.

3.3 Operation and Data Acquisition

AFIT's UCC was controlled and monitored through the COAL lab primary operation station pictured in Figure 53. Detailing the image labels in a counter clockwise direction: the 8-channel MKS controller regulated the ethylene and airflow to the igniter jet, the airflow readouts depicted real time commanded and actual inlet pipe flow rates, the LabVIEW VI served the dual purpose of controlling experimental operation and recording thermocouple and pressure transducer data, the Brooks controller was used as an alternate fuel mass flow controller, the Raspberry Pi operated the variable position diffuser, and the camera monitor provided visual confirmation of experimental operation. The employed VI recorded temperature and air mass flow rates at 10 Hz and fuel mass flow and pressure readings at 1 Hz.

Figure 53: COAL lab primary operation station [5]

A representative operating condition selected from DeMarco et al. [29] was tested and data was recorded for five minutes to evaluate the mass flow controller's ability to maintain a commanded value. The 7.62 cm line was set to 5.44 kg/min and was found to have an average value of 5.3 kg/min. It had a standard deviation of 0.09 kg/min resulting primarily from a sinusoidal fluctuation, shown in Figure 54, at a frequency of approximately 0.1 Hz. The fuel mass flow controller was set to 1.21 g/s and averaged 1.12 g/s with a standard deviation of 0.09 g/s.

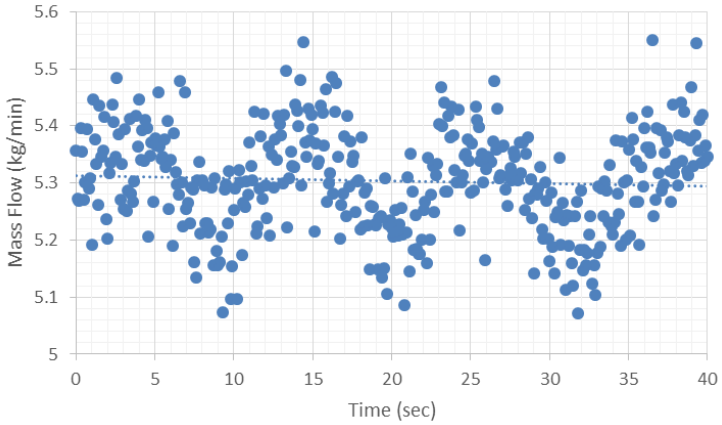

Figure 54: 7.62 cm airline actual mass flow at a commanded value of 5.44 kg/min

Lastly, the secondary airline was set to 1.0 g/sec yielding an actual flow that fluctuated between zero and 2.1 g/sec. This resulted in a mean value of 1.2 g/sec and standard deviation of 0.9 g/sec. To achieve this flow rate, the mass flow controller was set to 0.36% of its full scale value which resulted in the observed flow fluctuations. DeMarco [8] showed that cavity flow dynamics were highly dependent on step airflow, therefore the fluctuation was deemed unacceptable. To correct this issue, the 3.81 cm airline was replaced with the 1.91 cm line, which had a mass flow controller rated for a lower maximum flow, and subsequently retested. This resulted in an average value of 1.2 g/sec with a standard deviation of 0.2 g/s, an improved outcome.

3.4 Experimental Evaluation of Cooled HGV Designs

The first set of experiments conducted were designed to evaluate five concepts for cooling the HGV which were described in Table 1. Each of these designs had an opening in the stagnation region of the airfoil that would ingest air upstream of the combustor and route it internally for cooling. All five of these concepts were built into one HGV (with a sixth solid vane to provide a baseline) which was shown in Figure 33. This HGV was then installed into the UCC described in Section 3.1 and shown in Figure 40. Data was first acquired using a stepless outer ring with radial fuel injection (see Cottle et al. [25] for detailed description) to match the CFD investigation of DeMarco et al. [7]. However, testing challenges, discussed later in this section, necessitated the 12-Step outer ring be used to collect the data presented in this study.

IR thermography was employed to obtain temperature data as it provided the needed spatial resolution. To implement this measurement technique, matte black paint was applied to the trailing edge surface of the HGV for reasons discussed in Section 2.5. *VHT FlameProof* paint was selected as it had an advertised operating temperature of 1336 K once the provided curing instructions had been completed. The HGV was then installed into the UCC and tested five times at the same condition of DeMarco et al. [7] which was shown in Table 3. Each condition was held for five minutes and the UCC was allowed to cool to room temperature between runs.

It was found that the curing instructions as printed on the paint can were ineffectual and resulted in rapid paint blistering as seen in Figure 55. After several unsuccessful variations on the curing scheme were attempted, the author discovered that using the temperature and time combinations found in Table 5, and allowing the HGV to cool to room temperature between cycles, produced a durable painted surface. The temperatures in this table are presented in Fahrenheit as that is the operational units on the curing oven that was used. These values were based on

discussion with other *VHT FlameProof* users on various online discussion forums. Surface preparation was also critical, requiring sandblasting to obtain a bare metal surface as well as a metal etching solution (Klean Strip) to remove surface oxidation and corrode the grain boundaries allowing better adhesion.

Figure 55: Paint condition post test for five consecutive trials

Table 5: Curing times and temperatures for applied paint

Time	Temperature
15 min	250 ºF
30 min	600 ºF
60 min	800 ºF
30 min	1000 ºF

A FLIR SC 6700 IR camera was employed to capture the IR data. This camera used an Indium Antimonide (InSb) photodetector which was ideally suited for the midwave IR spectrum. Additionally, three internal, optical bandpass filters were selectable by the user of which the coated sapphire through flame narrow band filter was implemented. This filter was 90% transmissive from 3.85 µm to 4.00 µm and was manufactured by *Spectrogon* under the product number "BP-3900-200." A panchromatic image of the camera's view can be seen in Figure 56.

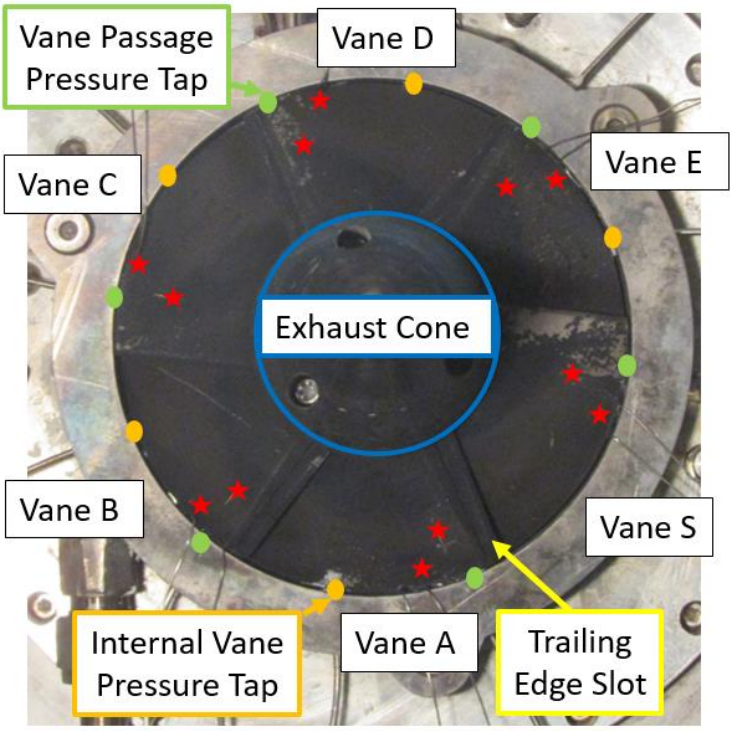

Figure 56: Imaged HGV surface with pressure tap and thermocouple (red stars) locations highlighted

Figure 56 also indicates the location of point measurement devices employed. K-type thermocouples with a diameter of 0.078 mm (indicated with red stars) were placed in channels located at 23% and 81% airfoil span and 4.19 mm and 11.9 mm from the trailing edge, respectively, to serve as calibration points for the infrared image. The thermocouple temperature uncertainty was at most ±6.4 K for the test cases which was determined using the manufacturer's specification of ± 0.75% of indicated temperature. Internal vane static pressure was measured through 1.59 mm pressure tap holes located at 85% axial chord, placing them nearly in line with the row of six cooling holes. The pressure taps were connected to a DTC Initium Pressure Scanner which provided the digital data stream with an accuracy of ± 35 Pa. Passage static pressure was measured through the same sized ports at the same axial location, but were offset by 30° locating them halfway between the vane tips.

The test condition of DeMarco et al. [7] was rerun with full instrumentation and the updated paint. A review of the IR image indicated that the vanes in the lower half of the UCC exhaust (at 4, 6 and 8 o'clock positions) were emitting significantly more than those in the upper half as seen in image A of Figure 57. For a sense of scale, the white region represents approximately 16,000 camera counts and the lowest intensity region (purple) is approximately 2,000 camera counts. While temperature distribution was expected to vary based on the vane cooling scheme employed, the extent of the disparity exceeded expectations. As such the HGV (image B), diffuser (image C), and the outer ring (image D) were each individually rotated and the test condition was rerun to determine if the temperature distribution was a function of the cooling scheme or related to the UCC hardware orientation. Qualitative analysis showed the vane surface temperature was a strong function of the outer ring orientation which, after cleaning the fuel and air lines and ensuring fuel delivery was uniform, had no discernable cause. As such, the outer ring developed by Cottle et al. [25] was exchanged for the 12-Step outer ring with the belief that this would more equitably distribute the fuel within the combustion cavity.

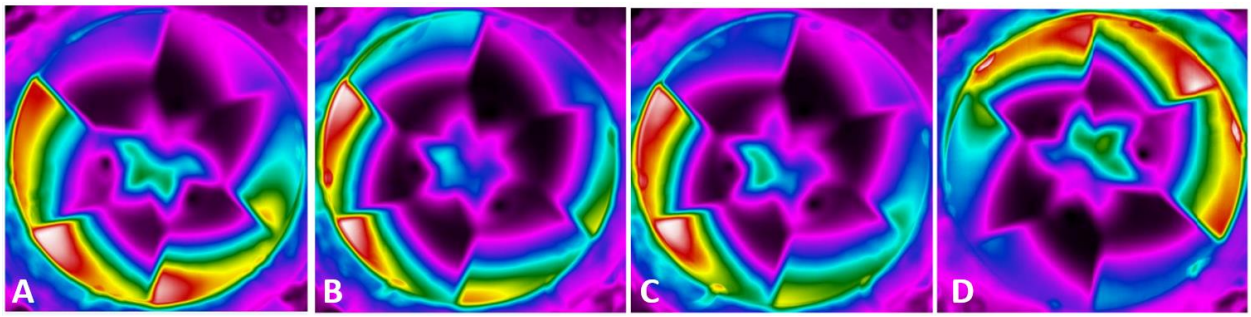

Figure 57: IR image of HGV trailing edges from initial image (A), with the HGV rotated 120° clockwise (B), diffuser rotated 180° (C), and the outer ring rotated 180° (D)

Data was then gathered on the cooled HGV in the reconfigured UCC at five operating conditions (initial ignition and then increasing the fuel flow by 0.3 g/s four times) each held for five minutes to create an IR image calibration curve using the method described in Section 2.5. As

the thermocouples had a different emissivity than the painted HGV surface, the direct pixel associated with the end of a thermocouple could not be used for calibration. Instead, a representative three by three pixel grid with the central pixel located four pixels upstream of the end of the thermocouple was selected and the nine "counts" values average. A graphic of this grid can be seen in Figure 58. Note: this image only approximates the raw data as the graphics file format employed created artificially higher resolution. By splitting each test case into two segments, using data from 3-4 and 4-5 minutes from each run, the five test conditions and twelve thermocouple measurements yielded 120 thermocouple reading/IR intensity data pairs.

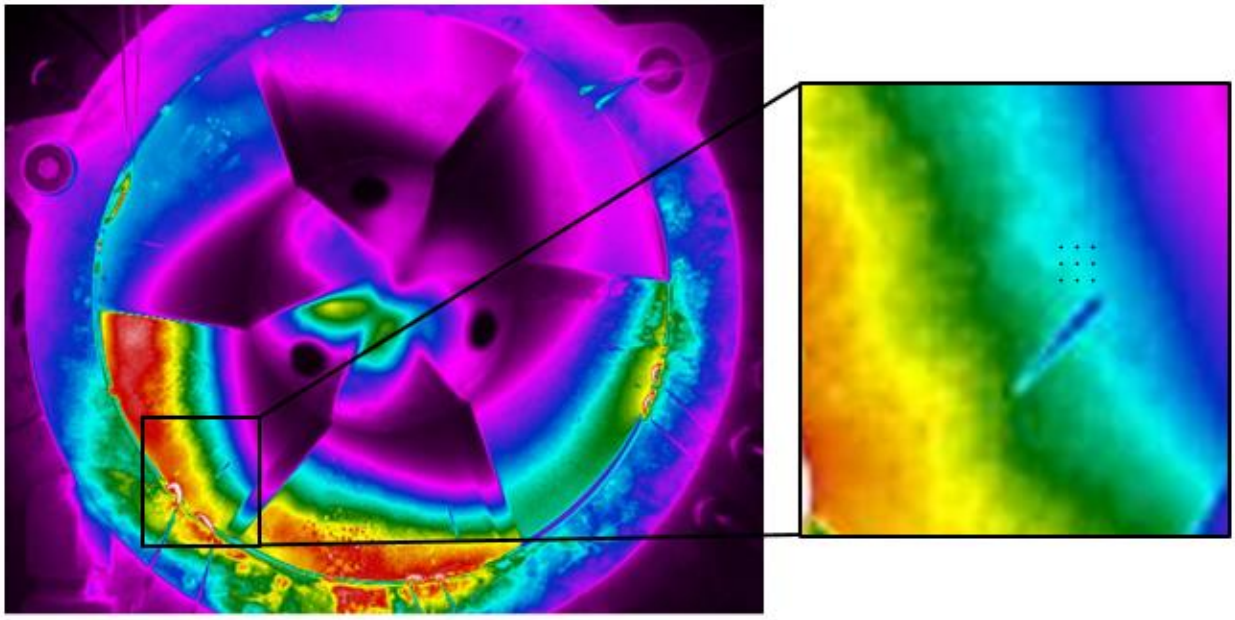

Figure 58: IR image and three by three pixel grid used to determine representative thermocouple intensity reading

Initially, twelve calibration curves were created, one for each thermocouple location. Eleven of the resulting curves had coefficients of determination exceeding 0.993 with the last having a value of 0.913. Next, the data from both thermocouples on a given vane were combined creating six calibration curves (one for each vane). A larger spread of coefficients of determination resulted compared to the analysis from a single thermocouple, ranging from 0.996 to 0.758. Vanes

with lower agreement between the two thermocouples had similar, but offset curves which coincided to areas with large temperature gradients. On these vanes, the representative pixel location was moved by up to two pixels which resulted in a better correlation for each vane. Lastly, all thermocouple-IR intensity data pairs were used as one data set and a curve fitted against it as shown in Figure 60. By taking the root sum squared of the difference between the 120 observed data points and the temperature predicted from the curve fit, the mean absolute difference between the thermocouple and curve fit was found to be 10.8 K.

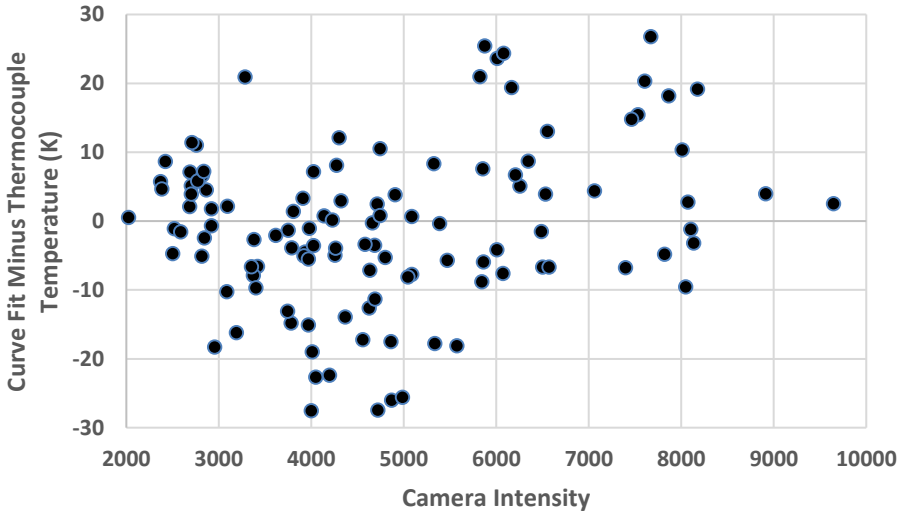

Figure 59: Residual data for IR camera calibration

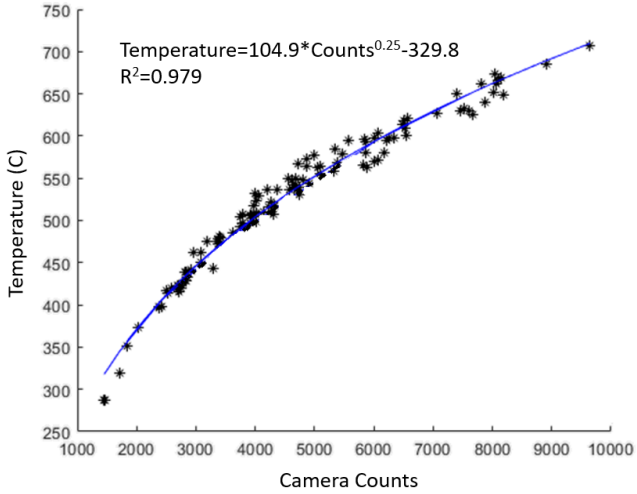

Figure 60: Calibration curve from functionality test

Next, the test condition from DeMarco et al. [8] was run with the addition of 1.2 g/s step airflow and the calculated calibration curve was applied to the IR camera image shown in Figure 61. Here color has been used to indicate surface temperature where red represents the hottest areas and blue the coldest. At the center of the image is the exhaust cone which is surrounded by the trailing edges of the six HGV vanes. Results of this initial run indicated that the temperature exiting the UCC was not uniform around the HGV. Hotter gases exited in the lower right position (Vane S).

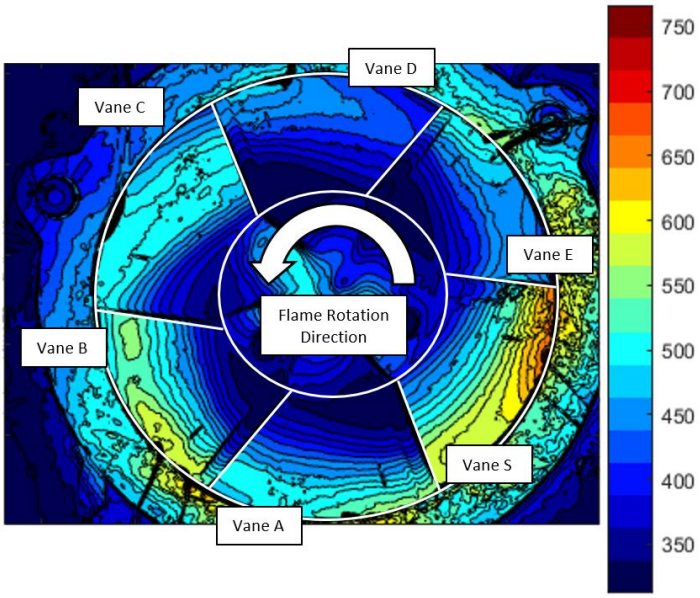

Figure 61: Calibrated IR image of Case 2

To verify whether this temperature distribution was a function of the cooling scheme or the physical orientation of the HGV in the UCC, the HGV was rotated 120 degrees and retested. Data from the rotated HGV at the same test condition is shown in Figure 62. This figure revealed that while the qualitative temperature patterns rotated with the vanes, the hottest temperatures remained in the same quadrant of the rig. Therefore, direct comparisons between the temperatures of different vanes would not be possible as the magnitude of the combustion gas temperature was dependent on its orientation. However, as temperature trends rotated as expected, qualitative comparisons of observed temperature patterns on the vane surface were possible between cases.

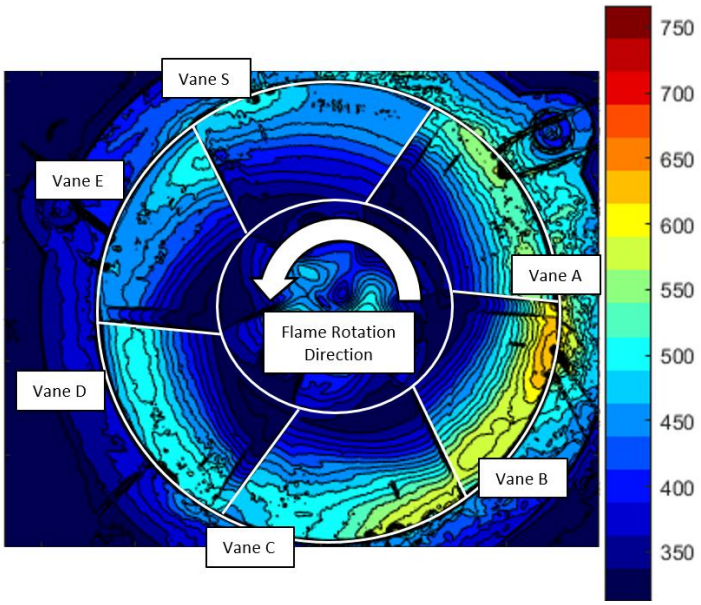

Figure 62: Calibrated IR image of Case 2 after HGV was rotated 120 degrees counterclockwise

To analyze the surface temperature distributions, data from three discrete axial chord locations (84%, 88%, and 93%) was evaluated for each of the vanes as shown in Figure 63. These locations were selected to capture the effect of the row of six cooling holes located at 86% axial chord and to understand the impact of the exit slot on the cooling in the aft end of the HGV. Data are plotted from 23% to 79% airfoil span on each vane to both bracket the region cooled by the cylindrical holes and to quantify the largest heat load area on the airfoil. It is important to note only half of the first region is subject to film-cooling (from 86% to 88% axial chord).

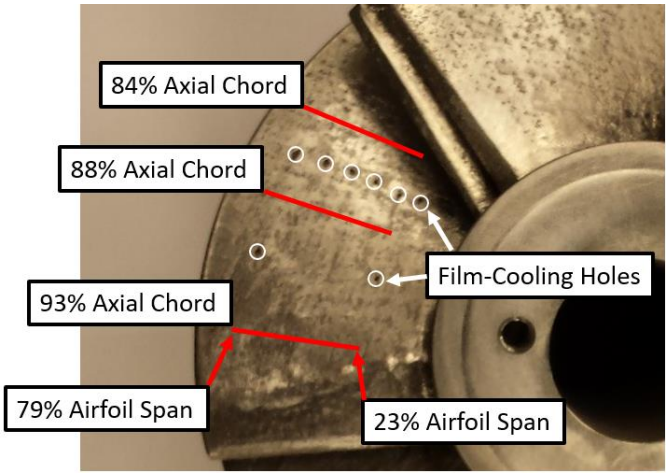

Figure 63: Axial locations of radial temperature readings

Fifteen operating conditions were examined that varied core, fuel, step, and air injection plate flow between three different values each. Changing fuel, step, and air injection plate flow altered the cavity dynamics creating an undesirable effects such as altering which vane passages experienced the hottest temperatures. Having a temperature dependence on cavity dynamics in addition to vane cooling was undesirable and as such, these parameters were held constant while core mass flow was varied as shown in Table 6. Core flow, which largely dictated the mass of airflow through the vane, was set to either 0.0656, 0.0756 or 0.0856 kg/s (referenced as Case 1, 2 or 3) to expand upon the DeMarco et al. [7] condition of 0.0756 kg/s. Airflow to the steps was held constant at 1.2 g/s providing the highest combustion stability while staying within the operable limits of the mass flow controller. The air injection plate was supplied 0.015 kg/s and the fuel flow was set to 0.0021 kg/s.

Table 6: Experimental test conditions for evaluating the cooled HGV

Case	Core Flow (kg/s)	Air Injection Plate (kg/s)	Step Air (kg/s)	Fuel (kg/s)
1	0.0656	0.015	0.0012	0.0021
2	0.0756			
3	0.0856			

3.5 Optical Investigation of Cavity Flow Characteristics with 12-Step Outer Ring

The second set of experiments conducted were design to understand the flow behavior within the circumferential cavity that drove the exit temperatures observed by DeMarco et al. [8]. Chemiluminescence imagery represented the ideal measurement technique for analyzing this flow as it provided high spatial and temporal resolution in addition to the ability to apply optical filters to examine different facets of the flame. Six test conditions, taken from the test matrix of DeMarco et al. [8], were evaluated and are shown in Table 7. These were selected to cover a wide range of previously observed UCC performance, from maximum exit temperature to highly unstable combustion. In the following sections, the modifications made to AFIT's UCC to enhance optical access to the circumferential cavity (Section 3.5.1) and the setup of the camera system employed (Section 3.5.2) are detailed.

Table 7: Experimental flow splits and equivalence ratios at total airflow of 0.108 kg/s

Core Percent	Air Injection Plate Percent	Cavity Equivalence Ratio
75	80	1.44
80	90	1.80
90	30	3.60
90	70	3.60
90	90	3.60
90	10	3.60

3.5.1 Modification of UCC Hardware to Accommodate Further Measurements

Previous variations of AFIT's UCC had at most 80° of optical access (Figure 64) to the circumferential cavity, an insufficient amount to analyze behavior in the entire annulus. As such, the entire back plate, which formed the rear enclosure to the circumferential cavity, was redesigned by Major Brian Bohan, Lieutenant DeMarco, and the author to maximize optical accessibility. Quartz was selected for the material as its transmissivity was suitable for the visible and ultraviolet spectrums where OH and CH luminesce. One solid piece, 4.78 cm thick, was designed to be sufficiently rigid to prevent deflection and thus cracking, have a large thermal capacity to retard temperature change and the associated thermal expansion, and cover the length of the HGV to fulfill the role of the exhaust collar. The installed final design can be seen in Figure 65.

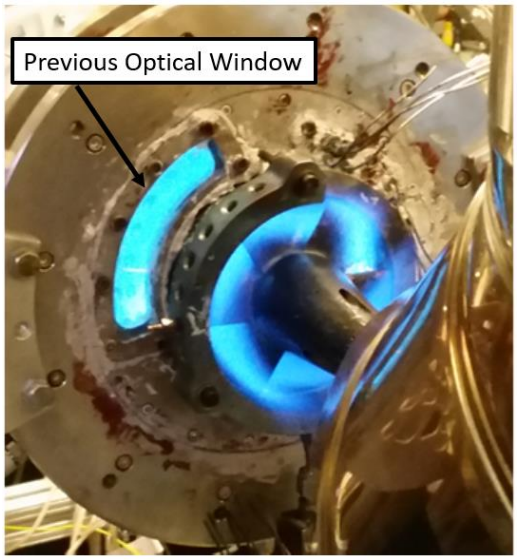

Figure 64: Previous UCC optical access to the circumferential cavity

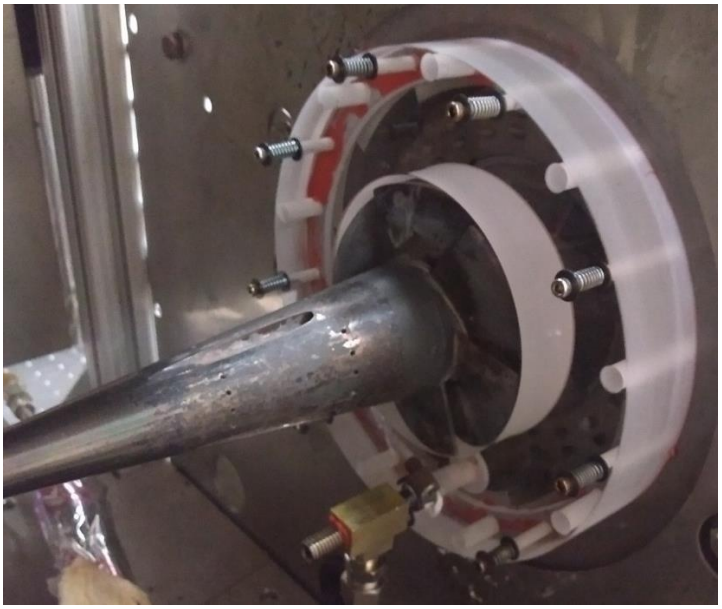

Figure 65: Installed quartz back plate

All dimensions were given clearance to ensure that thermal expansion of the quartz was not impeded by attached metal components. The need to mount the back plate to the UCC while still permitting thermal expansion was achieved with the use of springs and washers to disperse the load as shown in Figure 66. A compressive fitting was also used to fasten the igniter plug in position.

Figure 66: Bolt with spring used to mount back plate

Data were collected utilizing the modified UCC hardware enabling analysis of cavity velocities and combustion location. However, intermittent incomplete combustion in the circumferential cavity that continued to burn in the secondary zone (the HGV vane passages) and beyond created a challenge when trying to determine flow path and fuel residence time. These emissions had a strong radially outward component causing them to travel along the downstream

side of the back plate, partially blocking the circumferential cavity. Figure 67 shows this phenomenon occurring during UCC operation on the original hardware and with the updated quartz back plate.

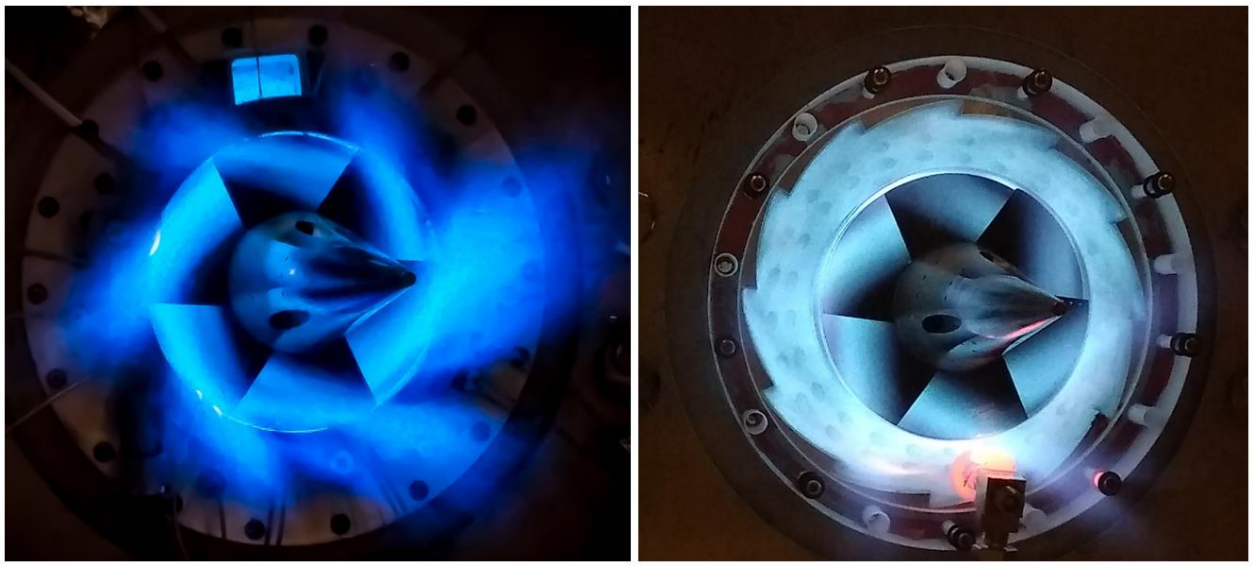

Figure 67: Flames exiting the HGV on the original UCC (left) and UCC with the redesigned, quartz back plate (right)

To prevent the exiting flame from obscuring the combustion occurring in the circumferential cavity, a hollow conical exhaust collar was added to the rear side of the back plate. The exhaust collar was mounted to the exhaust enclosure floor and held against the back plate using two mounting rods, so as not to create additional stress on the quartz. The interface between the exhaust collar and quartz was sealed with a Fiberfrax gasket and high temperature RTV which also prevented direct contact between the two components. A converging shape was selected to clear the line of sight of any optical measurements. To prevent this hardware from becoming a nozzle, the degree of taper of the exhaust collar was selected to match that of the exhaust cone, creating an approximately constant flow area. The modified UCC with the quartz back plate and exhaust cone can be seen in Figure 68.

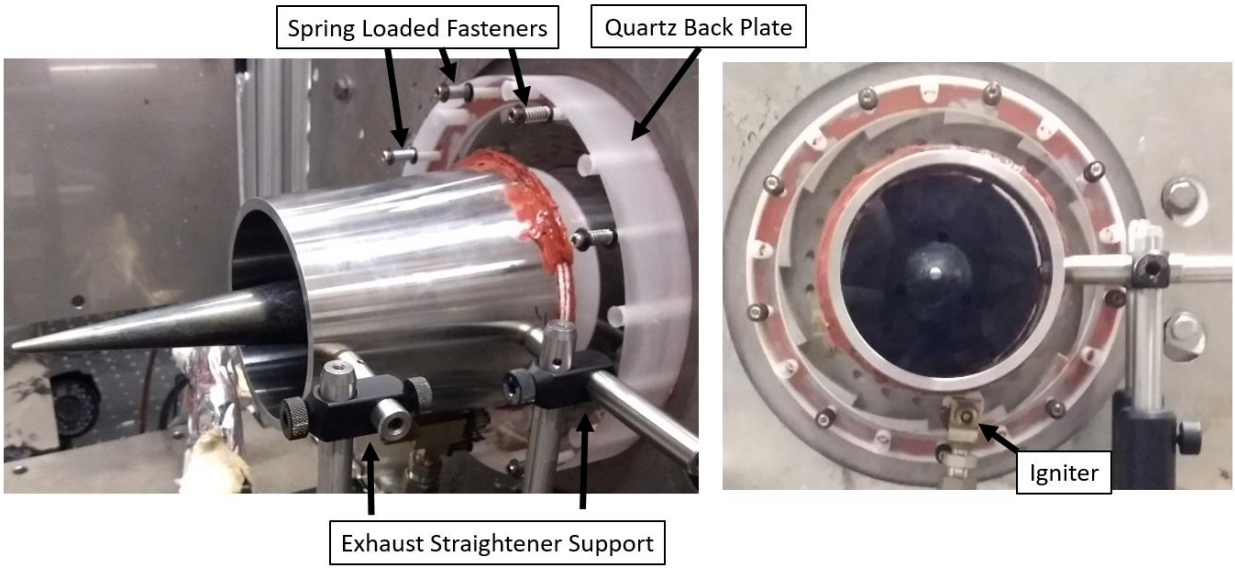

Figure 68: Modification of UCC hardware to enable further diagnostic measurements

The efforts detailed in this section complete the task of modifying AFIT's UCC to accommodate further diagnostic measurements. Optical access to the circumferential cavity was increased over four-fold enabling a more complete picture of the rotating flame's behavior. Additionally, the design and installation of the quartz back plate has enabled it to undergo hours of testing without breaking, representing a tool of continued value to AFIT's UCC research.

3.5.2 Chemiluminescence Imagery Experimental Setup

Flow was analyzed using high speed CI of OH and CH radicals with the camera setup shown in Figure 69. Optical access to the exhaust enclosure was achieved with a sapphire window. A bandpass filter, to block all but the emissions of interest, was attached to the end of the focusing lens. As emissions of both CH and OH are low in intensity, a LaVision High-Speed Intensified Relay Optic (HS-IRO) S20, 25 mm, 10 ns, two-stage image intensifier was used to amplify the images using 68% of max gain (81 counts/electron). The visible image produced on the IRO's phosphor screen was then recorded with a Phantom v16 high-speed camera at 10,000

frames/second using a 1280x800 pixel resolution and 99 µs exposure. The camera's exposure was specifically selected to exceed that of the IRO to ease synchronization requirements. To synchronize the camera and IRO, a LaVision control box was used and set to a 5 ns delay and 5,000 ns gate.

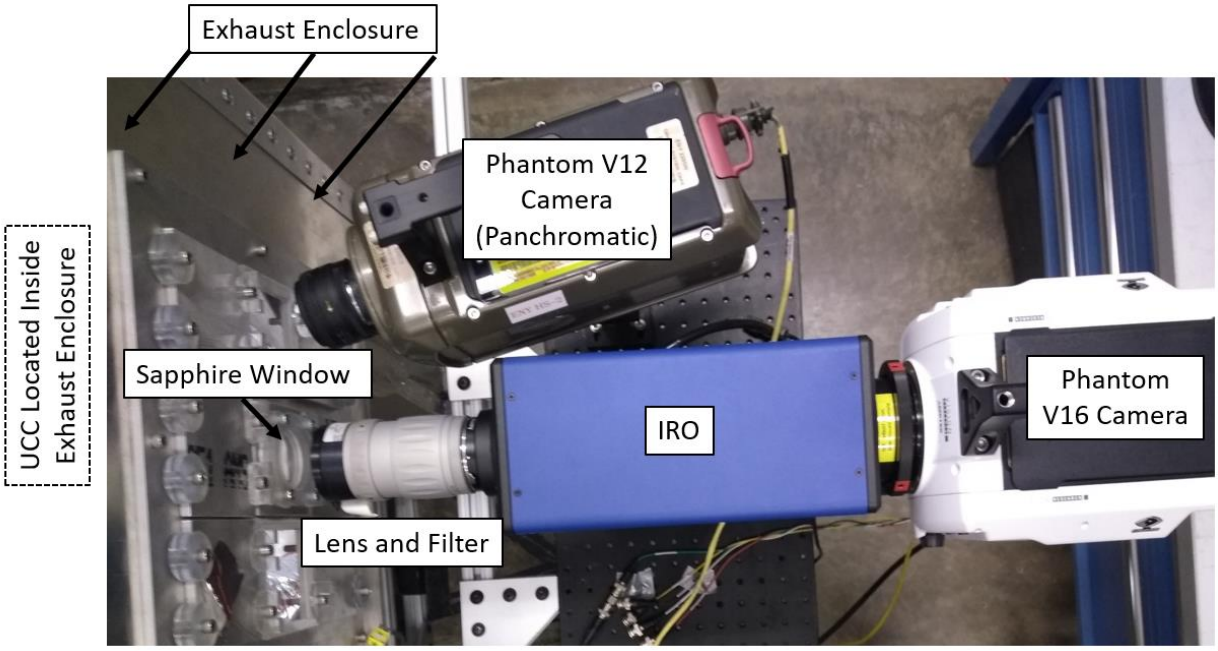

Figure 69: High speed OH radial CI camera setup

Additionally, a Phantom v12 high-speed camera was used to capture panchromatic data at 400 frames/second. With the slower frame rate and employment of an end trigger, this camera captured data on qualitative flame behavior such as initial combustor ignition and flameout conditions.

The six test conditions were each evaluated two times, one without the flow collar and one with. For the first of these, the camera was positioned looking directly down the exhaust cone. 5,000 CI and 4,000 panchromatic frames were taken at each condition with the OH filter, capturing the configuration seen in the left hand image of Figure 70. The visible features include the: air injection plate which can be seen as the ring with circularly arrayed angled holes furthest back in

the image, 12-step outer ring of which the side profile of the 12 steps can be seen, HGV and exhaust cone which are in the center of the image, and ignition source which is at the bottom of the image. A representative CI capture can be seen in the right hand image of Figure 70 with features of interest highlighted for ease of identification. Full annular images were not obtained due to camera alignment challenges. As previously mentioned, incomplete cavity combustion resulted in continued reaction in the HGV, indicated by the dashed line areas in the right hand image. These reactions intermittently extended downstream between the quartz and the camera interfering with the data of interest in the cavity. However, the emissions from the vane exit were readily distinguished from the cavity flow as they had nearly ten times greater velocity and were filtered out as part of the data analysis process.

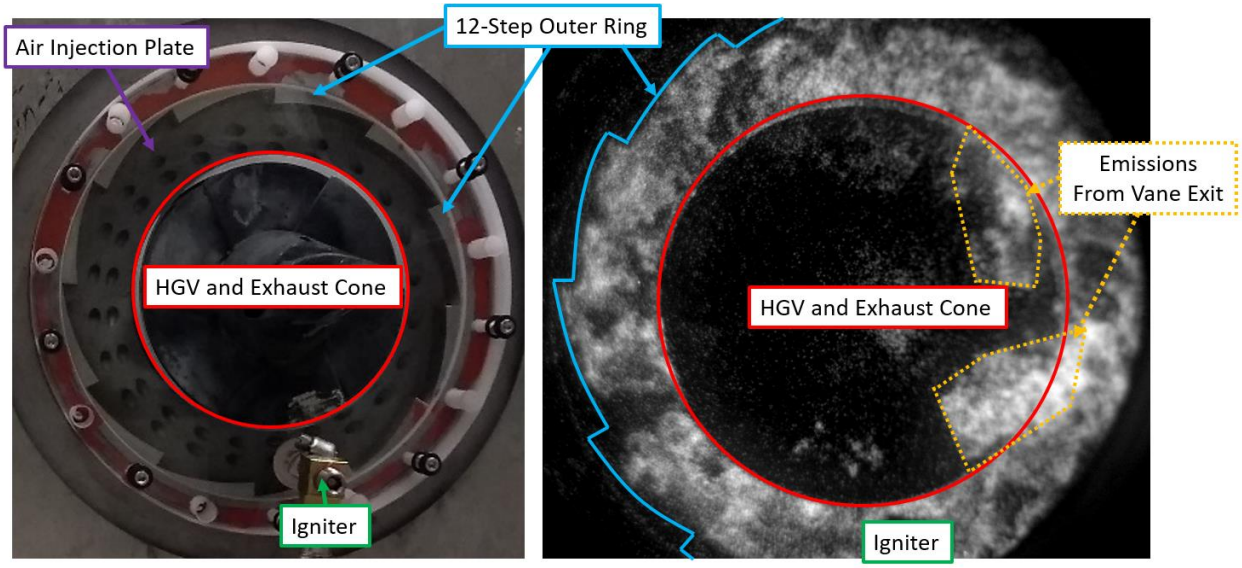

Figure 70: Approximate camera view of the circumferential cavity (left) and sample CI image (right)

All six flow splits were retested with the exhaust collar added, however, flameout occurred while trying to reach the 75/80 and 90/10 conditions. Although camera alignment was corrected, a limited field of view through the sapphire window to the exhaust enclosure prevented the camera

from imaging the entire cavity. As such, the camera was repositioned to look 5° off-axis of the exhaust cone and its resulting view can be seen in Figure 71. Data was collected with the OH filter and a subsequent test sequence with the CH filter both using the camera settings described at the start of this section. Local velocities were then calculated by Dr. Goss using the statistical cross correlation technique described in Section 2.6. The basic principle of this process can be understood by examining Figure 72. Knowing the time step between two frames and the corresponding displacement of a luminescing particle, the velocity can be determined. The accuracy of the calculated velocity was provided by Dr. Goss and was purely a function of physical pixel size. For the camera settings used in this study, the resulting uncertainty was 0.19 m/s.

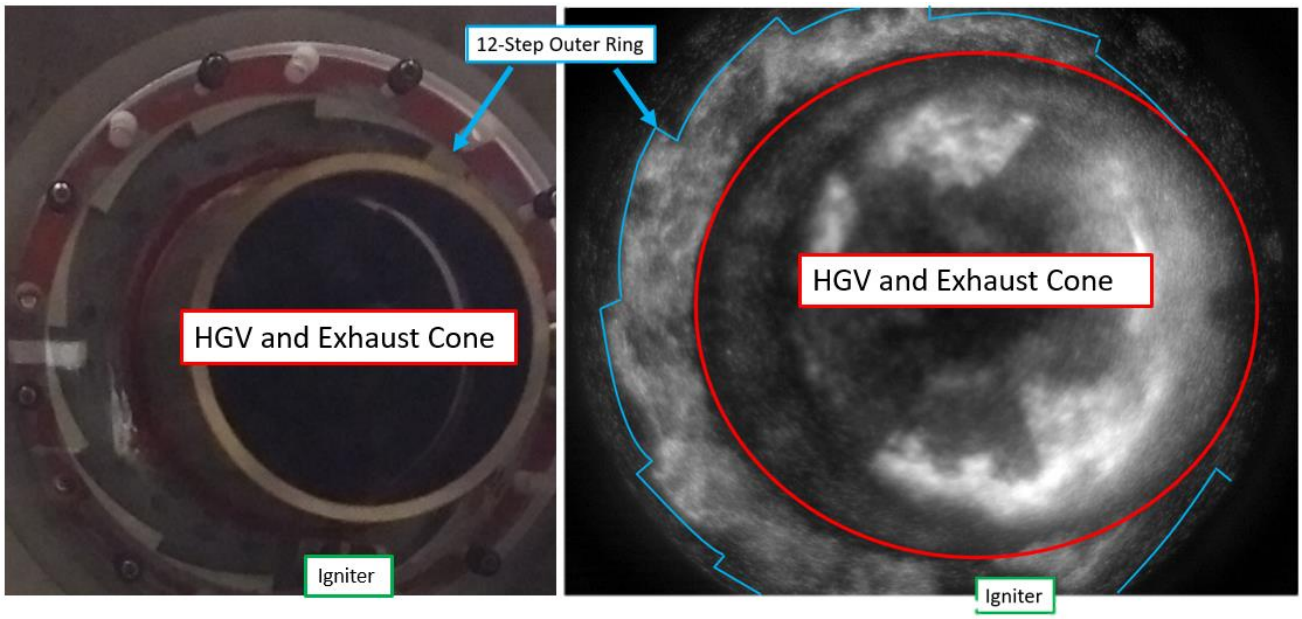

Figure 71: Panchromatic image (left) and CI image (right) of UCC with added exhaust collar detailing captured features

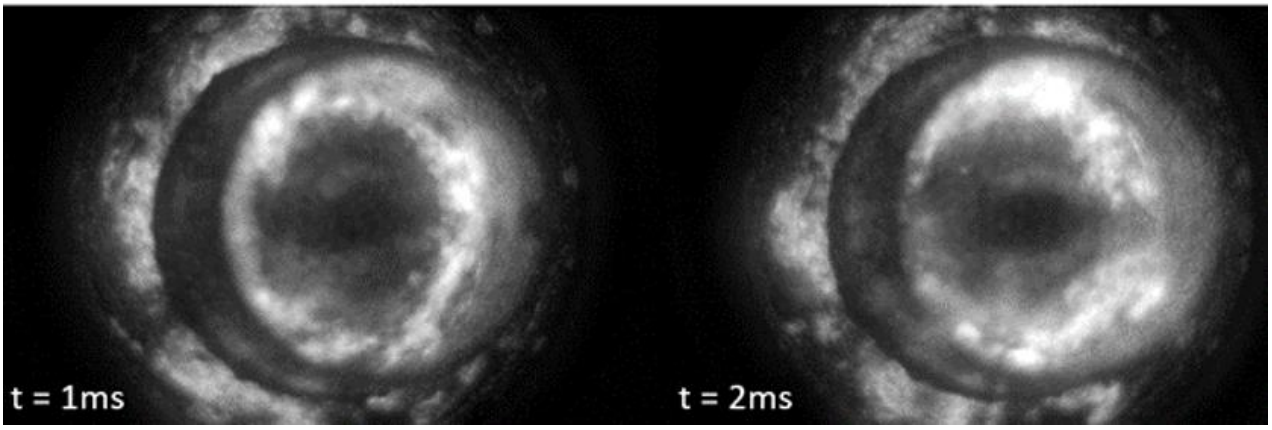

Figure 72: Two CI frames with one ms time step showing flame movement in circumferential cavity

IV. Results

The UCC employs a unique combustor center body to facilitate circumferential combustion. As operating temperatures continue to increase, cooling of this added hardware must be considered. Section 4.1 details the analysis performed on a passive cooling scheme to meet this need. Previous studies have found what operating conditions maximized AFIT's UCC exit temperatures, but were not able to link those findings to cavity flow dynamics. Section 4.2 reports on this study's effort to characterize combustion behavior and its relation to the previously observed exit temperatures.

4.1 Analysis of Cooled HGV Design Parameters

The first analysis in the current study examined the five cooled HGV configurations developed by DeMarco et al. [7], which are shown in Table 8, using AFIT's UCC as a combustion source. Three experimental cases were run each having a different core mass flow while holding the cavity air and fuel flow constant which were shown in Table 6. The temperature distribution on the surface of different vanes (measured across three locations shown in Figure 63) and internal to external pressure differentials were compared to understand the impact of specific design features. Section 4.1.1 introduces the temperature trends observed as well as the normalization process employed to non-dimensionalize the results. Section 4.1.2 discusses the impact internal vane cooling had on external temperature distribution. The impact of core mass flow on vane cooling effectiveness is discussed in Section 4.1.3. The effect of geometry on vane internal pressure rise and the resulting change in blowing ratio is discussed in Section 4.1.4. Section 4.1.5 investigates the impact of the employed film-cooling configuration on surface temperature distribution and Section 4.1.6 investigates the impact of altering the internal plug location.

Table 8: Variations in cooling schemes for the experimental HGV [7]

Vane	Plug Distance (mm)	Cooling Holes	Exit Area (cm^2)
A	5.84	Yes	0.477
B	2.29	No	0.587
C	5.84	Yes	None
D	5.84	No	0.587
E	5.84	Yes	0.587
S	N/A (Solid Vane)		

4.1.1 Observed Temperature Trends and Data Normalization

As discussed by DeMarco et al. [7] and shown in Figure 32, combustion products progressed downstream from the combustion cavity and formed a hot streak on the vane surface which at first moved both radially inward and axially downstream. Their CFD analysis showed the hot streak remaining near the 45% airfoil span as it moved downstream with a slight radially outward trend toward the vane's trailing edge on the solid vane. The film-cooled vane from their study exhibited the same hot streak trend until the row of six film-cooling holes, at which point the hot streak moved radially outward.

Experimentally, these radial temperature trends and the hot streak location are shown in Figure 73 (a magnified portion of Figure 61). The coldest temperatures were located near the center of the image at the hub of the HGV as the hot, radially outboard combustion products had not fully penetrated the cooler core flow. The vanes showed the hot streak entering the field of view around the 75% airfoil span and then moved toward the outside diameter, closely matching the previous numeric investigations. However, the experimental hot streak for all the vanes was located radially closer to the outside diameter.

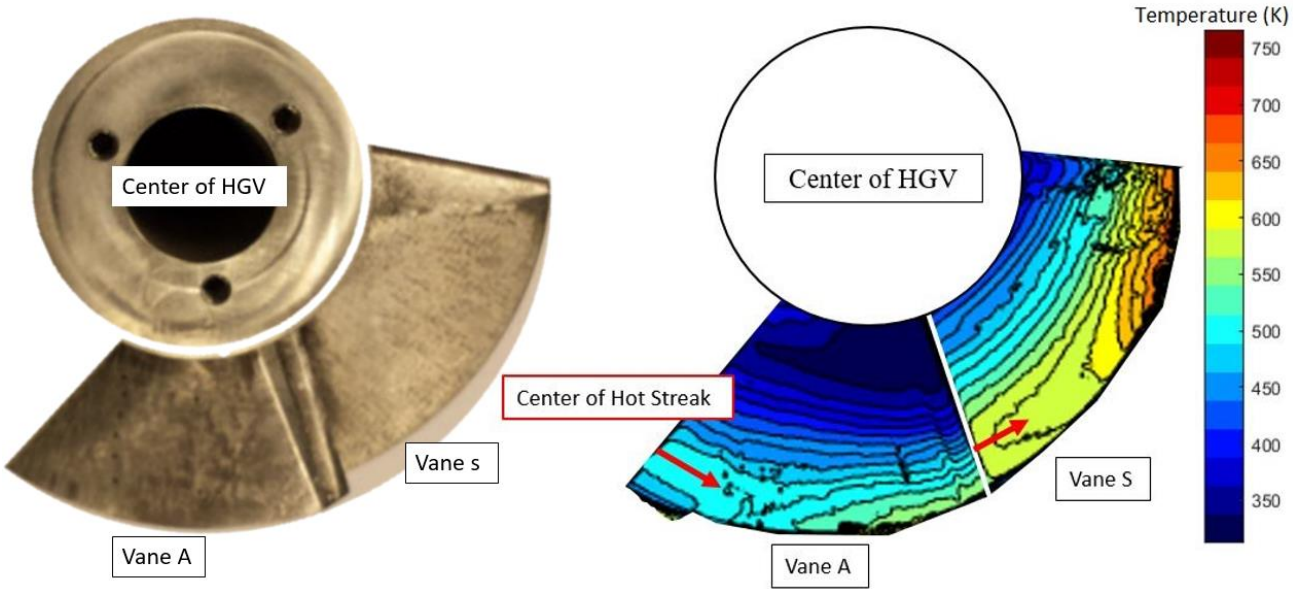

Figure 73: HGV hardware of Vanes A and S (left) and IR image (right) at Case 2

As indicated in Section 3.4, there were variations in the combustion dynamics within the cavity as well as an interaction between the core flow and the cavity flow that further complicated testing. However, to enable qualitative impacts, the actual magnitude of the hot gases (and subsequently the surface temperature) was factored out by normalizing by the average temperature between 23% and 79% airfoil span of the Case 2 condition at 84% axial chord. This value was determined for each vane and treated as a reference temperature, thus normalizing all temperature values (for all three cases) for that vane. Thus, a normalized temperature less than one indicates a lower temperature than the average temperature at 84% axial chord at Case 2 conditions.

The temperature trends for Vane A and S at 84% and 88% axial chord are plotted in Figure 74 as their normalized values and provide an understanding of the general temperature patterns observed. The lowest temperatures occurred closest to the ID which can also be seen in Figure 73. Moving radially outward, progressively higher concentrations of hot cavity gases raised the temperature which reached a maximum value at approximately 75% airfoil span. Radially outward of this location, the temperature remained primarily steady.

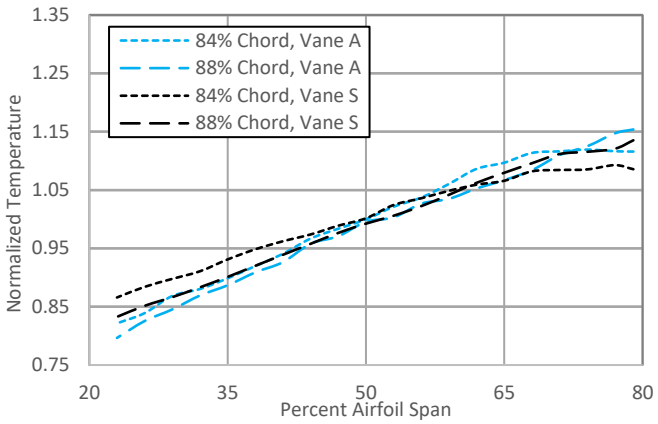

Figure 74: Vane A and S radial temperature distributions for Case 2 at 84% and 88% axial chord

4.1.2 Impact of Internal Vane Cooling

The first comparison of interest was evaluating the impact of internal coolant on the surface temperature distribution. While the normalization process eliminated the substantial change in temperature magnitude between the two vanes seen by DeMarco et al. [7], what was apparent was the average axial rate of temperature change for Vane A was greater than Vane S as seen in Figure 74. This was driven by the active cooling within Vane A showing, as expected, that internal airflow was an effective means to reduce the vane surface temperature.

This figure also indicates Vane A exhibited no greater temperature difference from the 84% to 88% axial chord position (before and after the row of six coolant holes) than Vane S. This similarity was due to the limited area of impact from the film-cooling, affecting only the 86%-88% axial chord area at a *P/D* of 6, and slightly below optimal blowing ratio which will be discussed further in Section 4.1.4. Figure 75 depicts the vane surface heat transfer reported by DeMarco et al. [7] and provides an understanding of the limited area of impact of the film-cooling scheme employed.

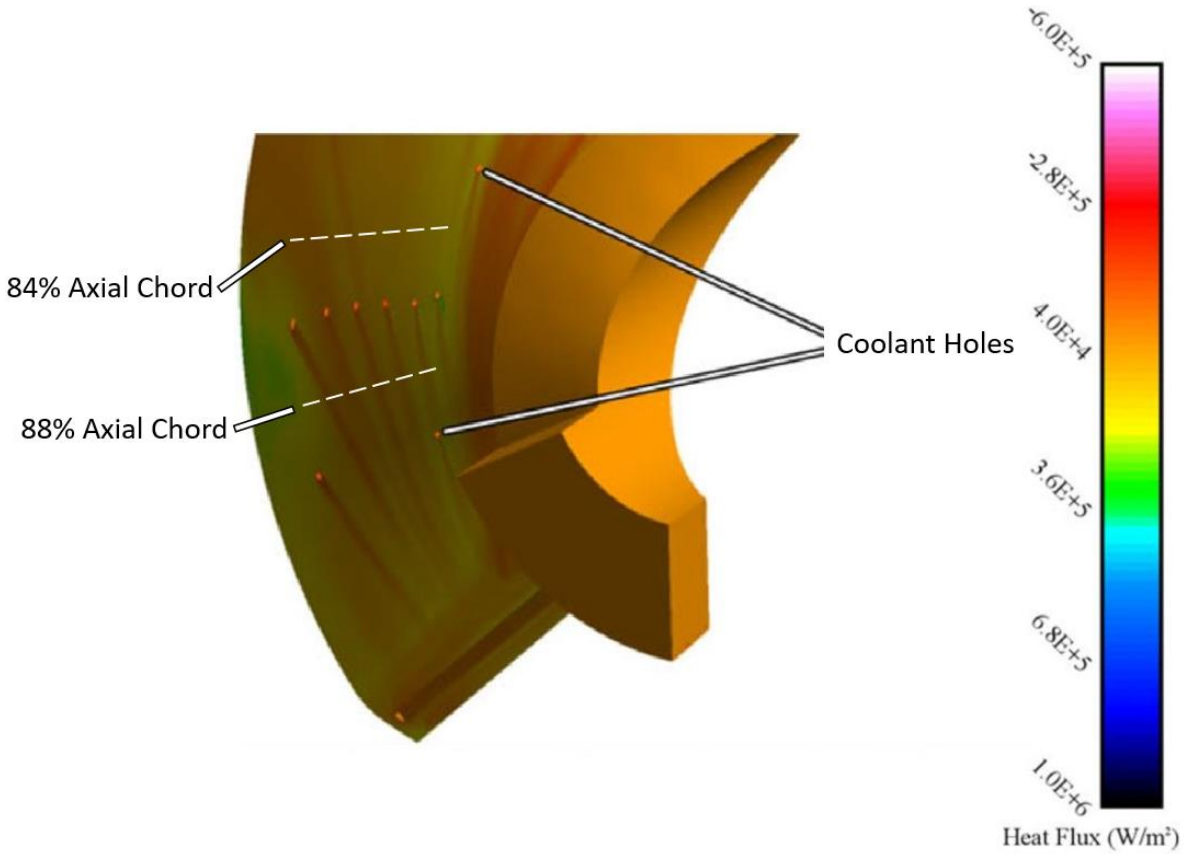

Figure 75: Coolant hole area of effect shown as vane heat flux contours [7]

4.1.3 Impact of Core Mass Flow

In the next comparison, Vane E (which had a trailing edge slot and film-cooling) was examined to understand the impact of varying core mass flow on vane surface temperature. Figure 76 and Figure 77 shows the impact of increasing the core mass flow from 0.065 kg/s (Case 1) to 0.085 kg/s (Case 3). This same data is shown in Figure 78 as differentials that were calculated by taking the normalized temperature at 84% axial chord and subtracting the normalized temperature at 88% axial chord from it (the difference across the row of six film-cooling holes) as well as subtracting the 93% axial chord from the 84% axial chord. The normalized temperature distributions at each axial station remained consistent as the core flow rate changed, indicating that the freestream and cooling characteristics remained similar.

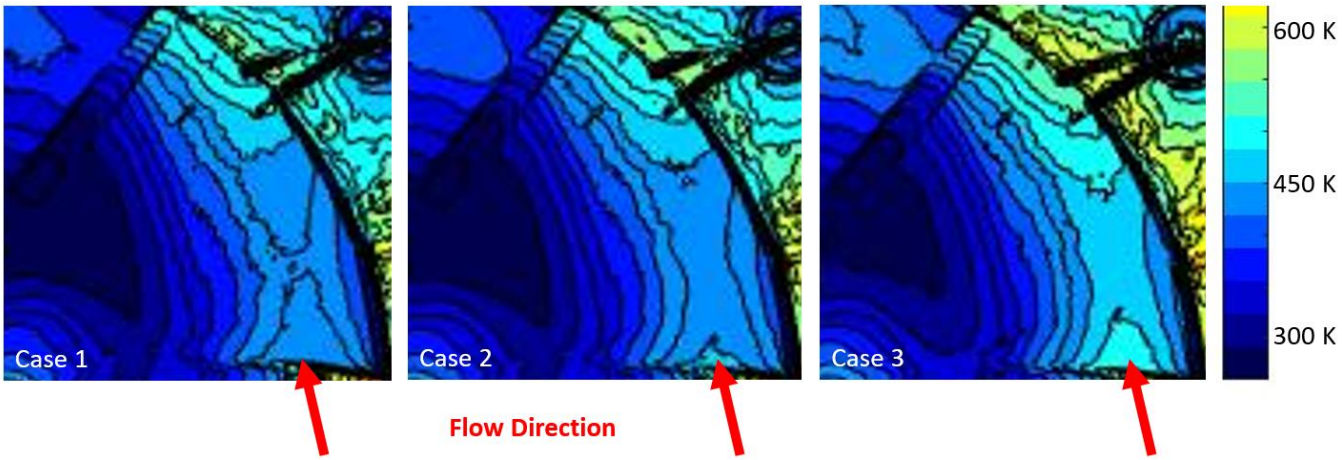

Figure 76: Vane E surface temperature from Case 1, 2, and 3

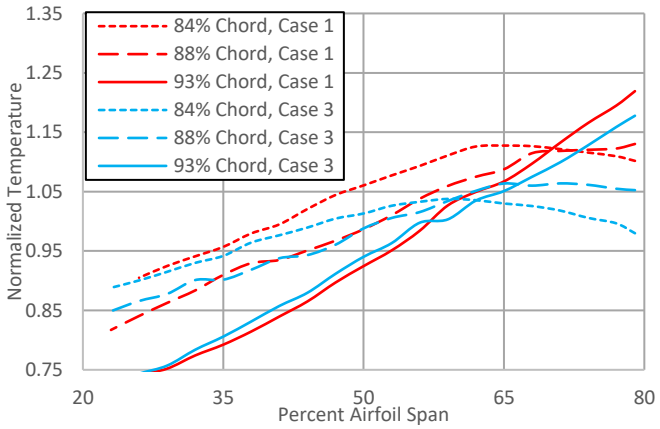

Figure 77: Vane E radial temperature at three axial chord locations

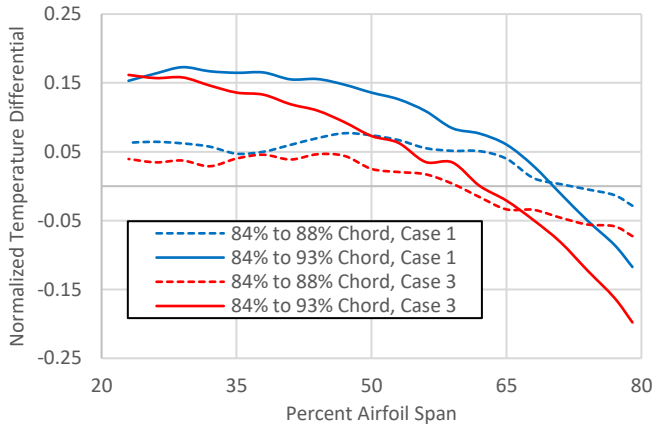

Figure 78: Vane E radial temperature difference between three axial chord locations

The increasing surface temperature with higher mass flow makes it clear that either vane passage temperature, the heat transfer coefficient to the vane surface, or both were increasing

between cases. While the cause of the observed temperature increase may be varied, Figure 78 shows that the cooling scheme employed provided a greater proportional benefit at Case 1. This means that the performance of future cooling designs will be difficult to predict when not tested at their expected operating conditions.

4.1.4 Impact of Blowing Ratio

Analysis of the cooling scheme's blowing ratios began by examining the internal to external pressure balance that drove the coolant flow. Internal pressures, measured near the 85% axial chord location, indicated the majority of the cooled vanes had nearly identical pressures as shown in Figure 79. These started at 3000 Pa (gauge) for the low core flow condition and then increased to 3800 Pa at the highest flow condition. Vane C differed, given it had the same inlet conditions as the other vanes but lacked a trailing edge slot as indicated in Table 8. This change resulted in an elevated internal pressure of 4500 Pa at the lowest mass flow which increased nearly linearly to 5800 Pa at the highest core mass flow.

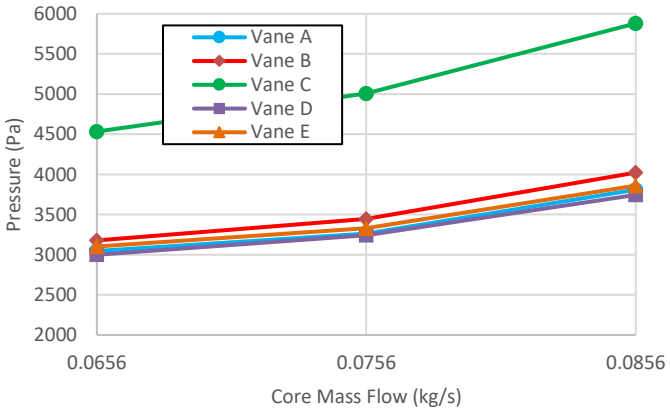

Figure 79: Vane internal gauge pressure

With the internal pressures known, a differential to the vane passage static pressure, taken at each vane passage mid-pitch at the outside diameter, was computed and can be seen in Figure 80. Vane E had the largest exit area resulting in the lowest internal flow restriction, and thus the

lowest pressure differential, compared to Vanes A and C. Vane A had a slightly smaller exit area resulting in a slightly greater pressure differential. Finally, Vane C, with no trailing edge slot, had nearly three times the pressure differential as all ingested coolant had to exit through the film-cooling holes.

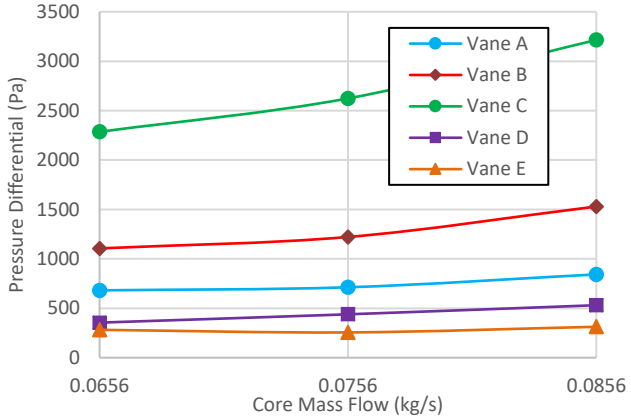

Figure 80: Vane internal to external pressure differential

To determine the blowing ratio, the coolant exit mass flow must be known, but this is not a value that can be directly measured. As discussed in Section 2.4, the coolant hole's discharge coefficient combined with the pressure differential between the interior and exterior of the vane enables the exit mass flow to be calculated. In this study, the average blowing ratio from the row of six coolant holes was desired for each film-cooled vane, at each case. While variations in the blowing ratio are expected between the individual holes in the row of six coolant holes, the goal of this analysis was to understand the average effect of the row of holes.

Coolant temperature was evaluated first to allow coolant Mach number and density to be determined. The temperature was assessed to be lower than the computational value of DeMarco et al. [7] for two reasons: measured circumferential cavity temperatures were lower (1,193 K versus 2,200 K) and measured vane passage temperatures with the addition of stagnation effects were approximately equal. As such a coolant temperature range of 441 K to 491 K was selected,

correlating to the CFD predicted value and 50 K cooler, yielding a density range of 0.72 to 0.80 kg/m^3. Coolant exit velocity would ultimately be calculated using Equation (15), but an initial velocity estimate would first be needed to determine the discharge coefficient from Figure 23. This value was initially guessed to be 50 m/s, based on the value of DeMarco et al., yielding a Mach number of approximately 0.1.

Next passage density and velocity were needed. In order to quantify passage density, passage temperature was measured by replacing the pressure taps measuring vane passage pressure with thermocouples. These thermocouples measured passage temperature off of the vane surface at the 75% airfoil span. Measured passage temperatures at Case 2 conditions were 1058 K for Vane A, 1037 K for Vane C, and 1026 K for Vane E which varied by no more than 43 K at the other two test conditions. A freestream velocity of 199 m/s at Case 2 conditions was taken (mid-span at the same axial chord location as the row of film-cooling holes) from the CFD analysis of DeMarco et al. and scaled proportionally with changes in core flow (Case 1: 173 m/s, Case 2: 199 m/s, and Case 3: 226 m/s). Freestream Mach number was found, using Kestin's [44] adiabatic index (1.37) for combustion gases at the experimental conditions, to be approximately 0.3.

Total coolant pressure to passage static pressure varied little between test cases with values of 1.04 for Vane E and A and 1.09 for Vanes C. Interpolating between the data from Gritsch et al. [32], shown in Figure 23, the experimental geometry and conditions in the present study resulted in a discharge coefficient of approximately 0.8. It is also important to note that the film-cooling holes employed in the present study had a length to diameter ratio of 3 while those of Gritsch et al. had a value of 6. As shown by Huning [45], this difference will cause the experimental coefficient of discharge to be higher than that predicted by Gritsch et al.

The discharge coefficient, pressure differential, and density were then used to determine the coolant jet's mass flow via Equation (16). As vane passage temperature varied across the radial span, a density range was determined for each passage at each condition spanning ±50 K from the measured temperature yielding values of 0.33 to 0.37 kg/m^3. Lastly, DeMarco [7] found the average coolant exit velocity for the row of six coolant holes was 30% greater than the exit velocity of the furthest radially outward film-cooling hole in that row. This difference correlated to a variation in vane internal to external pressure. In the present study, as vane internal pressure was being measured at the outside diameter and the average coolant exit velocity for the entire row of coolant holes was desired, a 30% correction was added to the coolant exit velocities mirroring the findings of DeMarco. Table 9 details the primary values used in determining various blowing ratios.

Table 9: Primary values used in determining coolant jet blowing ratio

Property	Vane A	Vane C	Vane E	Passage
Temperature (K)	441-491			≈1040
Velocity (m/s)	35	79	24	199
Density (kg/m^3)	0.72-0.80			0.33-0.37
Mach Number	0.1			0.3
Blowing Ratio	0.42-0.58	0.82-1.07	0.26-0.38	N/A

Using Equation 1 and the above values, the blowing ratio range for Cases 2 and 3 was 0.42 to 0.58 for Vane A, 0.82 to 1.07 for Vane C, and 0.26 to 0.38 for Vane E with Case 1 having a higher upper and lower bound for each vane by approximately 10%. While there was uncertainty in the calculated blowing ratios, comparisons between the three vane configurations could be made. Vane C exceeded the optimum blowing ratio of 0.6 described by Bogard et al. [29], while Vane A was slightly below this value, and E was well below this mark. As previously mentioned, the film-cooling hole scheme employed only had a limited area of jet coverage, but the coolant did

impact the radial temperature distribution. Figure 81 shows the three vane temperatures before and after the row of six film-cooling holes. In the near hole region, none of the coolant configurations resulted in a large change in normalized temperature. There did seem to be a larger variation for Vanes A and E where more attached coolant jets were expected to occur.

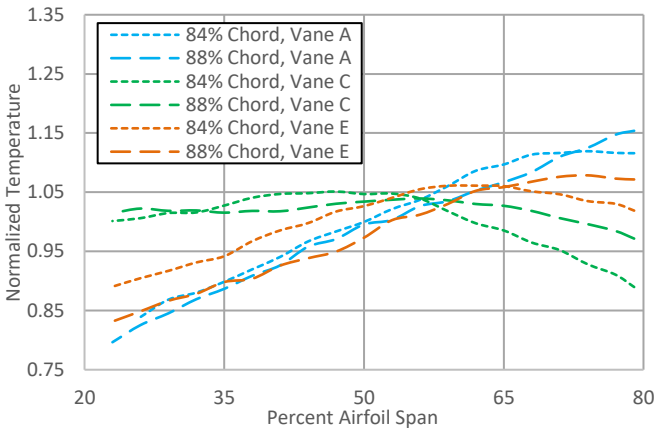

Figure 81: Vane A, C and E radial temperature distribution before and after film-cooling holes at Case 2

What was more prevalent was the shift in temperature distribution seen in Vane C. At this higher blowing ratio, the coolant jets were expected to separate and penetrate into the core flow. As discussed in Section 2.4.1, DeMarco et al. [7] noted that the coolant jets had the effect of disrupting local hot streaks which can be seen in Figure 32 by comparing the movement of the hot streak between the solid vane and the film-cooled vane. With Vane C having a greater pressure differential than in the analysis of DeMarco et al., this effect was more pronounced as shown in Figure 82. Upstream film-cooling has shifted the hot streak location on Vane C such that it entered the field of view much closer to the center of the vane compared to Vanes A and E. At the row of six coolant holes, Vane C's strong coolant jets normal to the passage flow further disrupted the radial temperature variation resulting in a flatter temperature profile across the airfoil span. A graphical representation of a separated jet and its effect on temperature distribution can be seen in

the bottom image of Figure 22. Vane A experienced an attached coolant jet and had a lesser effect on the hot streak migration, while Vane E had an even lower blowing ratio resulting in a weak coolant buffer to the hot passage flow.

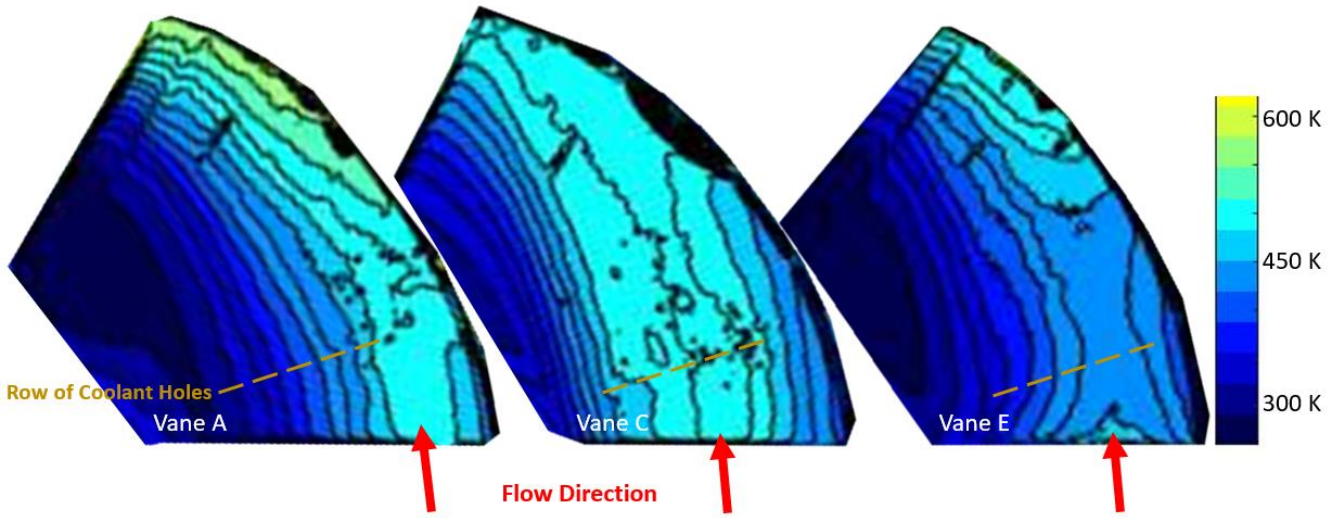

Figure 82: Calibrated IR image of Vane A, C, and E at Case 2 conditions

4.1.5 Impact of Film-Cooling

To isolate the impact of film-cooling, Vanes D and E were compared at Case 2 conditions and their surface temperature distributions can be seen in Figure 83. Both vanes had a common trailing edge slot size of 0.587 cm^2, but Vane E had coolant holes, while Vane D did not. This difference enabled an examination into the actual impact that the film-cooling might have on surface temperature. Normalized temperature at three axial chord locations for both vanes is shown in Figure 84 and normalized temperature differences (calculated in the same manner as Figure 78) are plotted in Figure 85. Vane E exhibited a temperature differential from 84% to 88% axial chord which continued downstream as shown in the 84% to 93% lines. Vane D, with no film-cooling, had little temperature change from 84% to 88% and less temperature change from 84% to 93%

compared to Vane E. This difference in temperature change indicates a positive benefit of film-cooling even with the limited area of impact of the current film-cooling scheme employed.

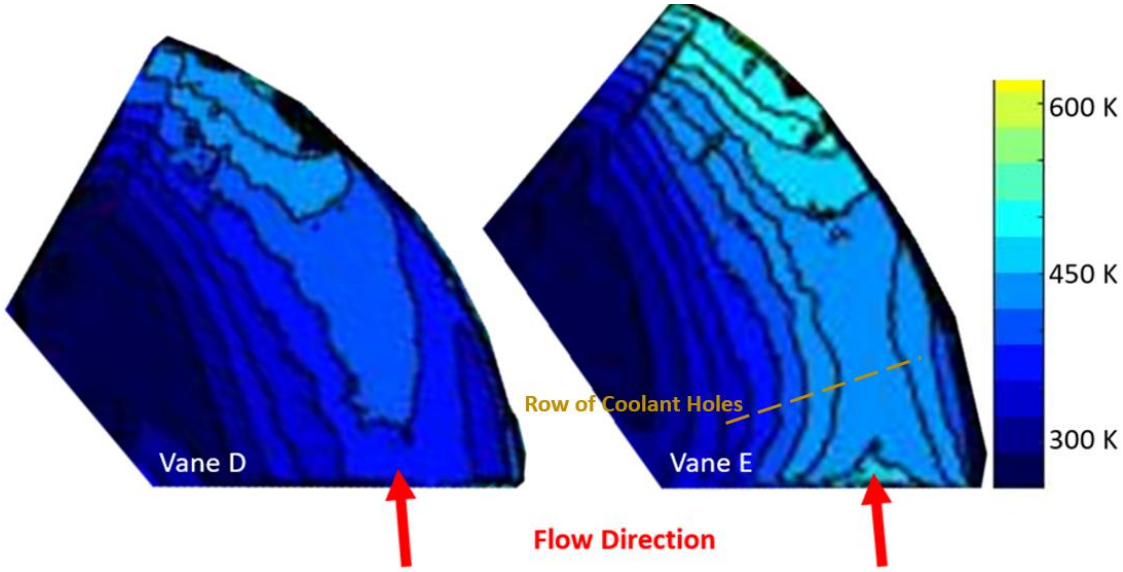

Figure 83: Vane D and E calibrated IR image at Case 2 conditions

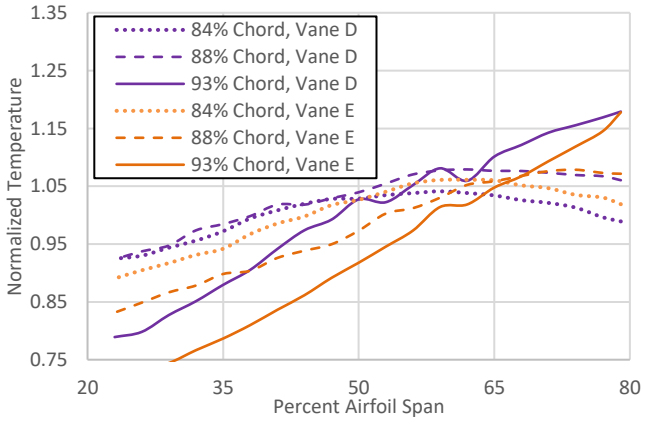

Figure 84: Vane D and E radial temperature at three axial chord locations for Case 2

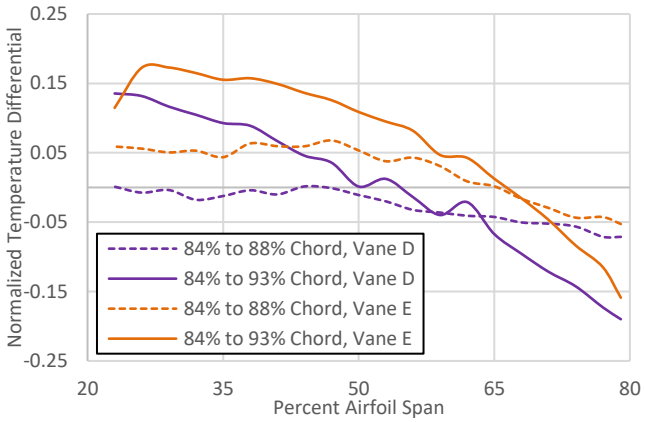

Figure 85: Vane D and E radial temperature differences for Case 2 between three axial chord locations

4.1.6 Impact of Internal Plug Location

The last investigation studied whether the inlet plug location impacted the temperature of the HGV. Vane B had the same geometry as Vane D with the exception of its internal plug being located at 2.29 mm from the vane leading edge instead of 5.84 mm. As shown by Bohan et al. [6] the plug impacted the manner in which the coolant entered the internal portion of the airfoil where decreasing the plug's distance from the opening resulted in a 0.7% higher mass flow through the part. Figure 86 shows the calibrated thermal image for both vanes at Case 2 conditions. Figure 87 details the normalized temperature at three axial chord locations for both vanes and Figure 88 indicates the temperature differentials which were calculated in the same manner as Figure 78. As neither vane employed film-cooling, the hot streak location and radially outward movement was similar between the two vanes.

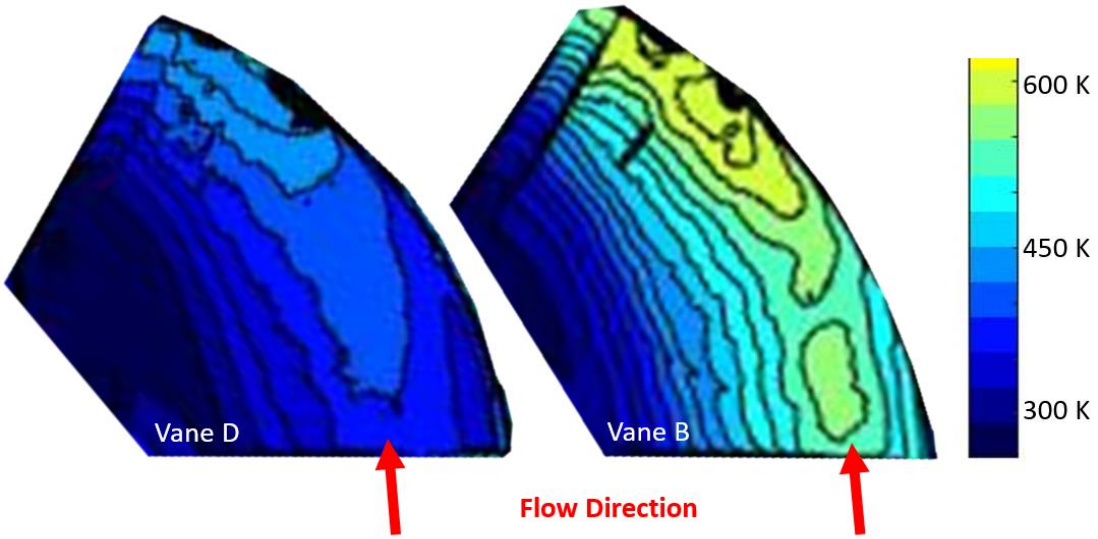

Figure 86: Vane D and B calibrated IR image at Case 2 conditions

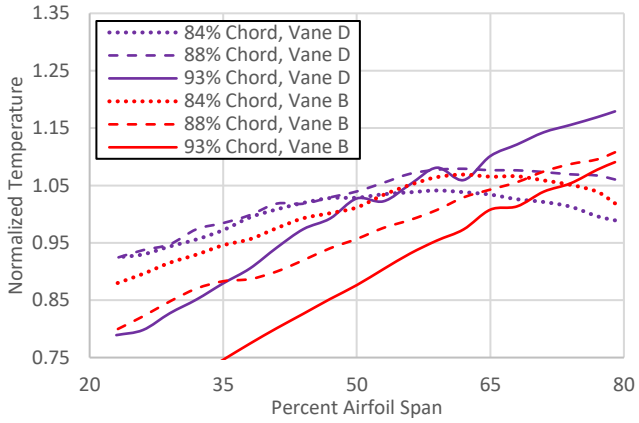

Figure 87: Vane D and B radial temperatures at three axial chord locations for Case 2

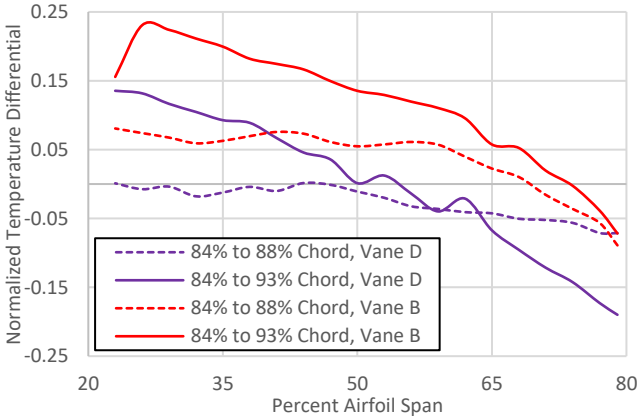

Figure 88: Vane D and B radial temperature differences for Case 2 between three axial chord locations

Vane B was expected to have slightly more internal mass flow than Vane D. More mass flow would be expected to result in a more rapid temperature change moving downstream due to increased heat transfer to the internal coolant. This difference was observed, however, it was not conclusively a result of the plug location. As seen in Figure 86, Vane B had a hotter surface compared to Vane D which equates to a larger temperature gradient between the internal coolant and surface temperature. As the rate of heat exchange was a function of the temperature difference, the higher surface temperature of Vane B would result in a greater rate of cooling.

While the effects on surface temperature may not be apparent, the difference in internal to external vane pressure is. Vane B developed twice the pressure differences compared to Vane B at the 85% axial chord location. This makes internal plug distance a sound means to achieve the desired pressure differential (and thus blowing ratio) as it has the ability to alter the pressure rise without dramatically changing the internal vane mass flow.

The results of this section conclude the research objective of understanding the impact of various passive cooling schemes for the HGV. It was shown that internal vane cooling was an effective means to reduce the surface temperature. Increasing core mass flow possibly altered both vane passage temperature and the heat transfer coefficient at the surface, showing that the UCC operating conditions will inform the optimum cooling scheme configuration. Coolant hole blowing ratio was strongly affected by changes in exit slot area and the resulting vane internal to external pressure differential. Two of the vanes exhibited sub-optimal blowing ratios while Vane C had a large enough value to disrupt the migration of hot gases through the vane passage. The specific hole scheme employed provided limited surface film coverage, but still indicated a modest benefit. Substantial vane passage temperature differences obfuscated any possible cooling benefit of varying the distance of the vane internal plug from the vane opening. However, moving the plug

location resulted in doubling the vane internal to external pressure difference. This shows that an optimal blowing ratio can be achieved by adjusting the plug location to create the ideal pressure rise.

4.2 Analysis of Combustion Characteristics in the Circumferential Cavity

The second analysis investigated flow behavior in the circumferential cavity of AFIT's UCC to address the second objective. Initially, data were collected without an exhaust collar and provided information on general flow behavior (Section 4.2.1), cavity tangential velocity distribution (Section 4.2.2), observed reaction frequencies (Section 4.2.3), the effectiveness of the step flame stabilizers (Section 4.2.4), and flow characteristics at flameout (Section 4.2.5). Six test conditions, detailed in Table 7 and shown in Figure 89, were conducted that replicated experimental conditions tested by DeMarco et al. [8] to better understand the underlying combustion dynamics driving their observed average exit temperatures. An exhaust collar was then added and measurements of cavity flow path length and flow path travel time were taken (Section 4.2.6) and Case 2 from Section 4.1 was rerun to investigate the flow dynamics creating the non-uniform vane passage temperatures (Section 4.2.7).

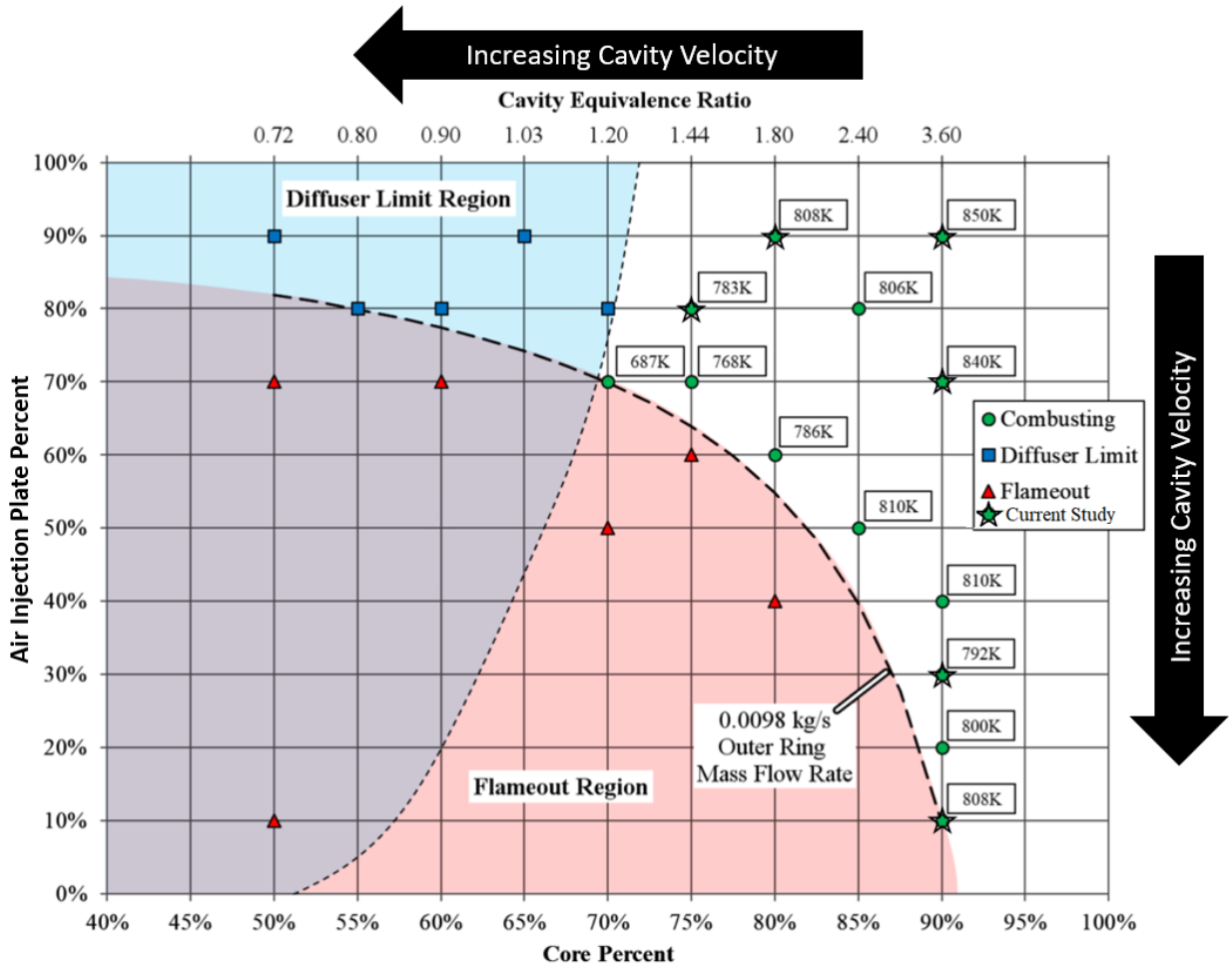

Figure 89: Test matrix for 0.108 kg/s total airflow (modified from [8] and repeat of Figure 17)

4.2.1 Flame Behavior in the Circumferential Cavity

OH radical CI was captured using the experimental setup and test conditions described in Section 3.5 and a sample frame from the initial setup can be seen in Figure 90. Highlights have been added to features of interest to better orient the reader. At the center of the image is the trailing edge of the HGV and exhaust cone. The ring around this is the circumferential cavity which contains the counter clockwise rotating combusting flow. White indicates areas where the molecules of interest are luminescing and dark areas where they are not. Along the outside

perimeter of the frame is the profile of the 12-Step outer ring. Alignment challenges in the initial setup resulted in the off center image.

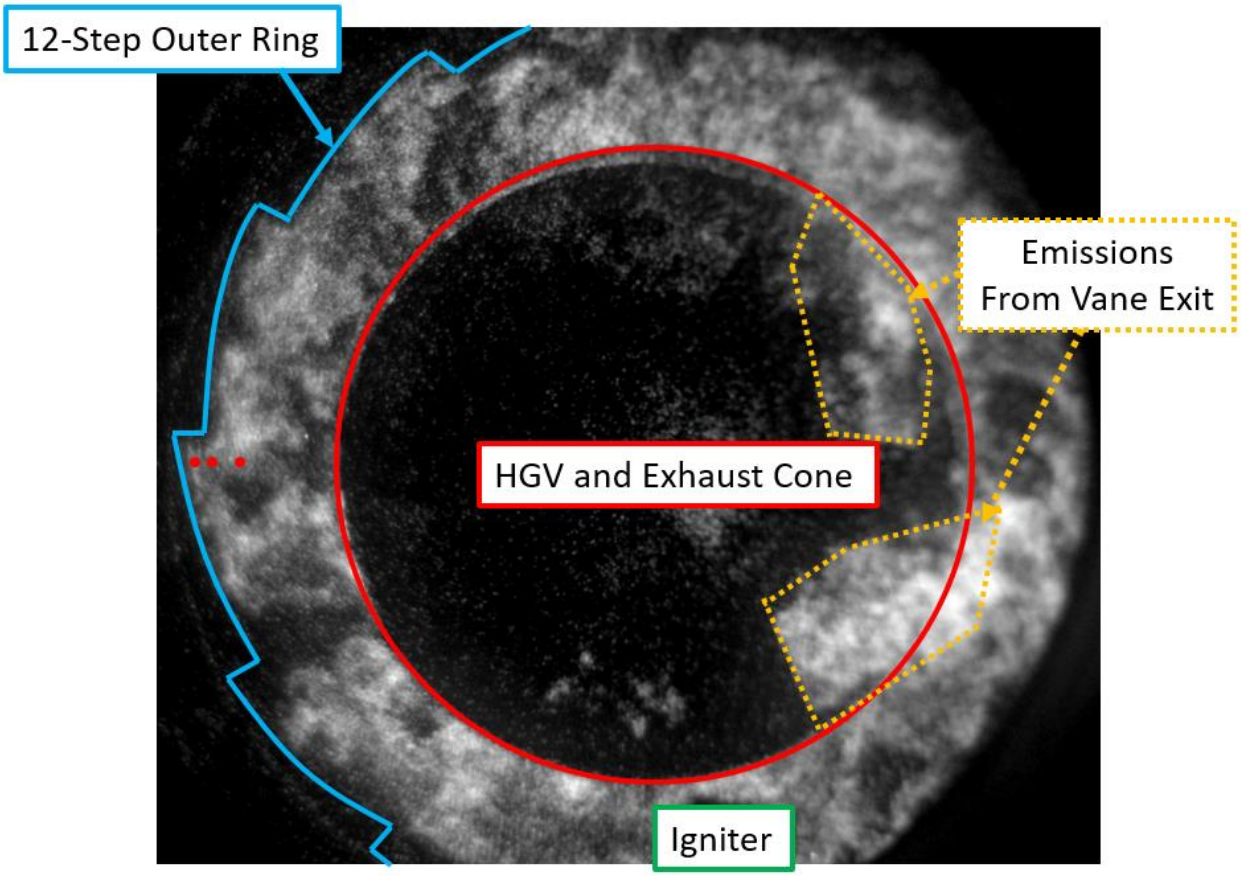

Figure 90: CI video frame from initial setup detailing captured features

For the second set of tests (covered in Sections 4.2.6 and 4.2.7), the exhaust collar was added, radially bounding emissions from the HGV. This enabled improved imaging of the circumferential cavity as shown in Figure 91. While the camera positioning was improved, its field of view was not able to image the entire circumferential cavity. As such, an off-angle view was chosen as it permitted the greatest portion of the cavity to be viewed.

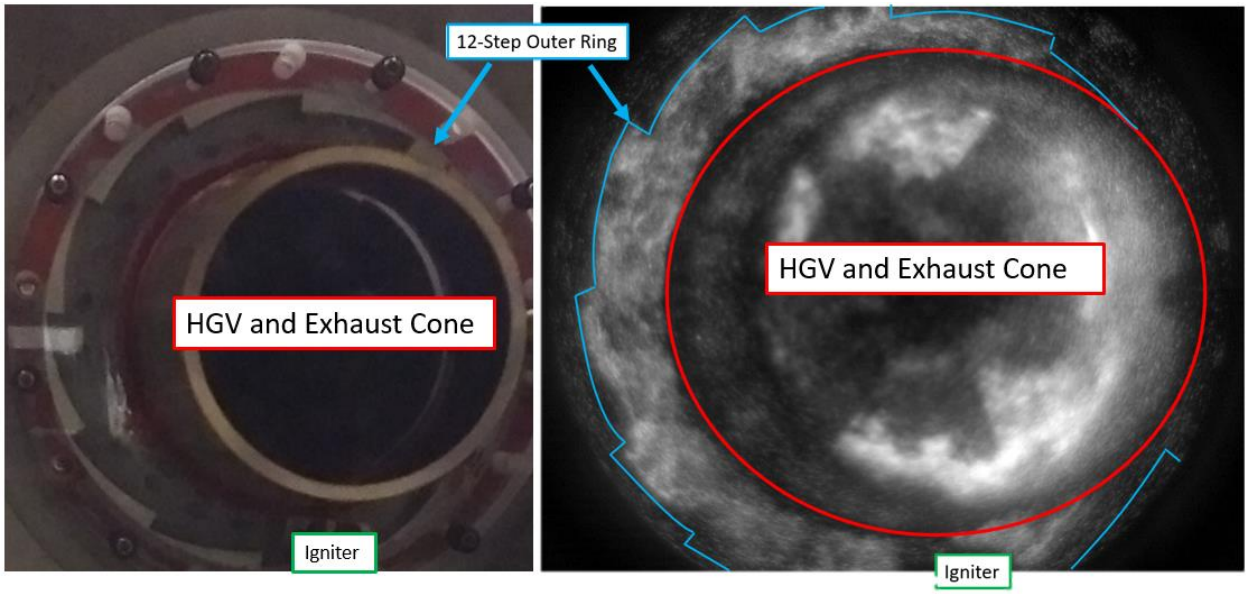

Figure 91: Panchromatic image (left) and CI frame (right) of UCC with added exhaust collar detailing captured features

All flow splits exhibited fluctuations in cavity combustion, but the unsteadiness was much more pronounced in the operating conditions where DeMarco et al. [8] observed lower exit temperatures. Sequential video frames from the 90/30 flow split with the exhaust collar are shown in Figure 92 to detail this observation. Voids, with little reaction activity, were present between the reacting areas and rotated around the circumferential cavity. These pockets had an oscillating boundary line with no apparent consistent frequency. The flow splits with lower expected tangential velocity had primarily small voids, resulting in a cavity more full of reactions.

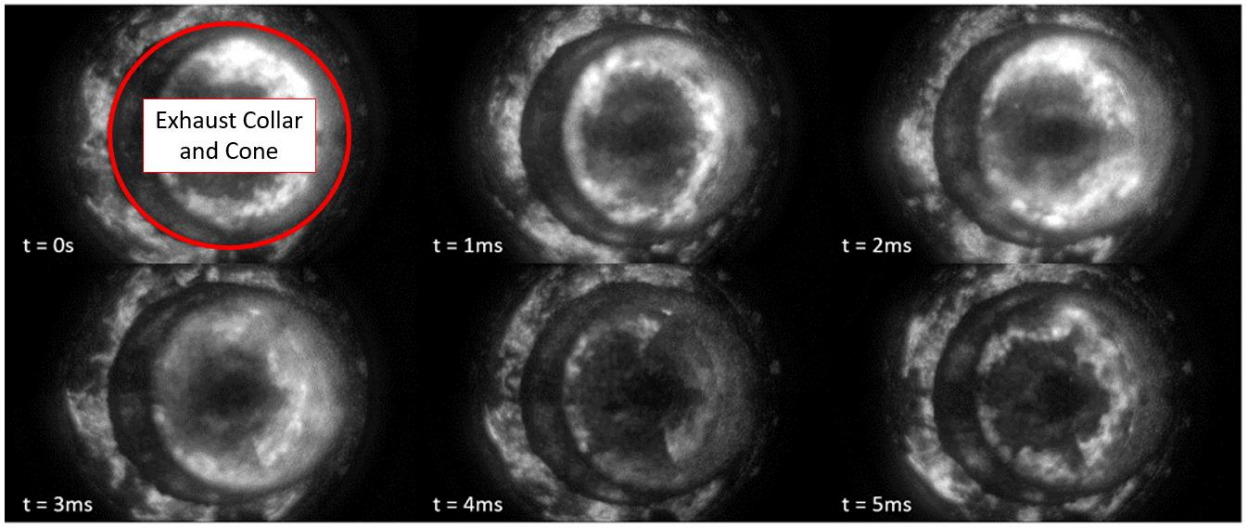

Figure 92: CH radical CI montage of 90/30 airflow split with exhaust collar

4.2.2 Circumferential Cavity Tangential Velocity Distribution

For the first set of analysis, CI was converted from a pixel to dimensional coordinate system using the step height as a known dimension and the center of the exhaust cone as the origin. Next, movement of OH radicals was tracked in relation to the coordinate system across sequential frames allowing the average flame tangential velocity at each pixel location to be determined. Processed results from CI data of the 90/70 flow split are shown in Figure 93. As flame velocity determination requires sequential tracking of OH movement, velocity near the outside diameter of the cavity and near the HGV could not be determined as OH radicals were entering and exiting the field of view at those locations. Velocity accuracy was constrained as a function of the physical length of a pixel, which in this analysis resulted in an uncertainty of 0.19 m/s. This error does not consider particle movement in the axial direction, which cannot be captured with a single camera setup, but this motion was expected to be small as the cavity was only 2.54 cm deep. The velocities shown in Figure 93 represents the average velocity at each given location calculated from all 5,000 frames. Combustion fluctuations with a frequency approximately lower than 10 Hz could

potentially skew the average, as data was collected for 0.5 seconds. However, frequency intensity distribution (discussed further in the following Section) indicated an intensity that was dispersed over 0-400 Hz with no consistently large low frequency spikes. The 75/80 and 90/90 flow splits were rerun on a separate date and found to have an average tangential velocity approximately 20% faster than the original data sets indicating variability based on external UCC conditions. While the flow conditions were held constant between these two days, the later test added an exhaust collar. It is possible a back pressuring of the system drove the observed velocity differences.

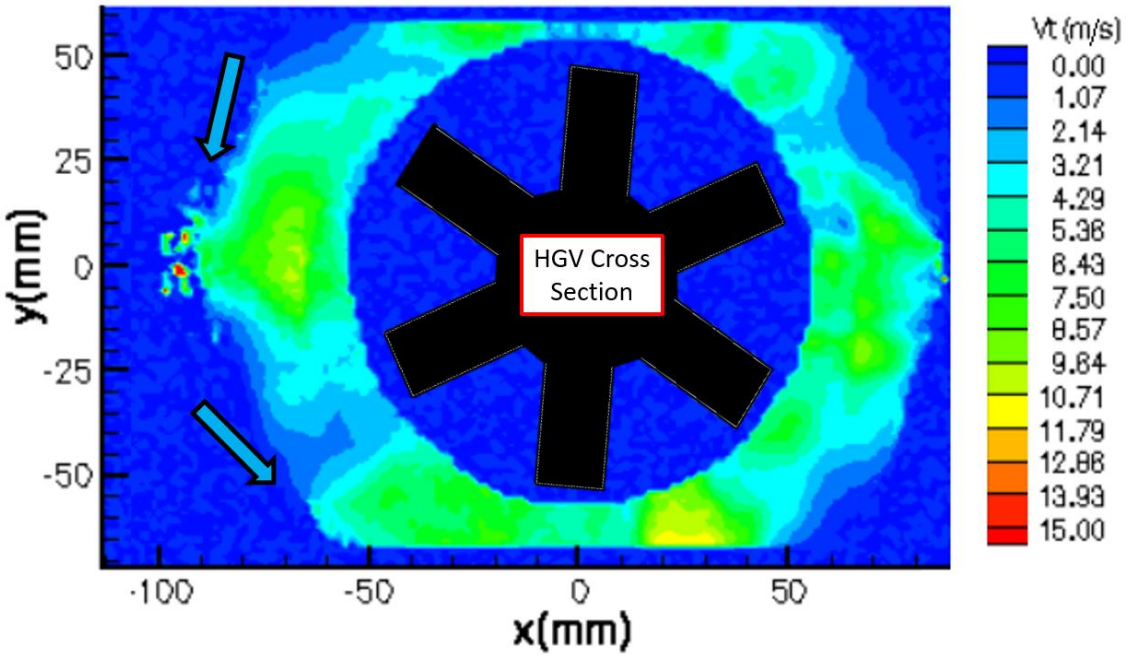

Figure 93: Average flame tangential velocity for the 90/70 flow split determined from CI data

The data indicated that while the direction of fluid swirl within the cavity was consistent, the magnitude of that motion varied in a periodic manner. Pockets of increased tangential velocity of around 10 m/s appeared at various circumferential locations that had little variation in the radial direction. The pockets correlated to the air injection from the fuel and air steps on the 12-step outer ring (indicated with arrows) and the location of the HGV vane passages. The pressure side of the

vanes, where the rotating cavity flow impinged, disrupted the tangential flow creating pockets of decreased downstream flame velocity. Average flame tangential velocity for the first five cases are shown in Table 10 as well as those reported by DeMarco et al. [8]. The root mean square of the velocity data would provide insight to the velocity fluctuations, but was not evaluated as part of the primary analysis. However, to scope the possible extent of this unsteadiness, the average root mean square of velocity data from the visible area of the 90/90 flow split was computed and found to be 4.26 m/s indicating significant fluctuations in velocity. The variations between the present study's average velocity findings and those of DeMarco et al. are likely explained by the differences in observable cavity area. The analysis by DeMarco et al. had very limited optical access to the combustion cavity, thus a locally fast or slow region may have been all that was visible in their observations. With a larger field of view, the present study's average velocity captures these rotationally periodic variations. Velocity trends from the present study match expectations with less core flow or air injection plate flow resulting in increased velocity.

Table 10: Average flame tangential velocity at various flow splits

Core Percent	Air Injection Plate Percent	DeMarco et al. [8] Results (m/s)	Current Findings (m/s)
75	80	Not reported	7.38
80	90	Not reported	5.73
90	30	6.0	6.24
90	70	4.0	5.55
90	90	3.9	4.33

4.2.3 Circumferential Cavity Frequency Analysis

Next, the frequency of OH luminance intensity at discrete locations was examined at five flow splits acquired at 10,000 frames/sec. Visual analysis of the data did not exhibit either the uniform pulsing or periodic intensity observed by Bohan et al. [27]. By applying a Fast Fourier Transform (FFT), spectral data from three locations downstream of the fuel only step shown as

red circles on Figure 90 (radially one half step height, one full step height, or two step heights from the outside diameter and all at one step height downstream from the step face) were further analyzed. These data are shown in Figure 94 and Figure 95 at a resolution of 10 Hz and exhibited no discernable trends. If a revolving flame front were present it would be expected to have a frequency on the order of 10-30 Hz which is the frequency the bulk tangential motion creates traveling around the circumferential cavity. As only 0.5 seconds of video were captured at 10,000 frames/sec and several periods of a given frequency must be observed for accurate quantification, low frequency data was limited in resolution. Longer data collects would have enhanced low frequency resolution.

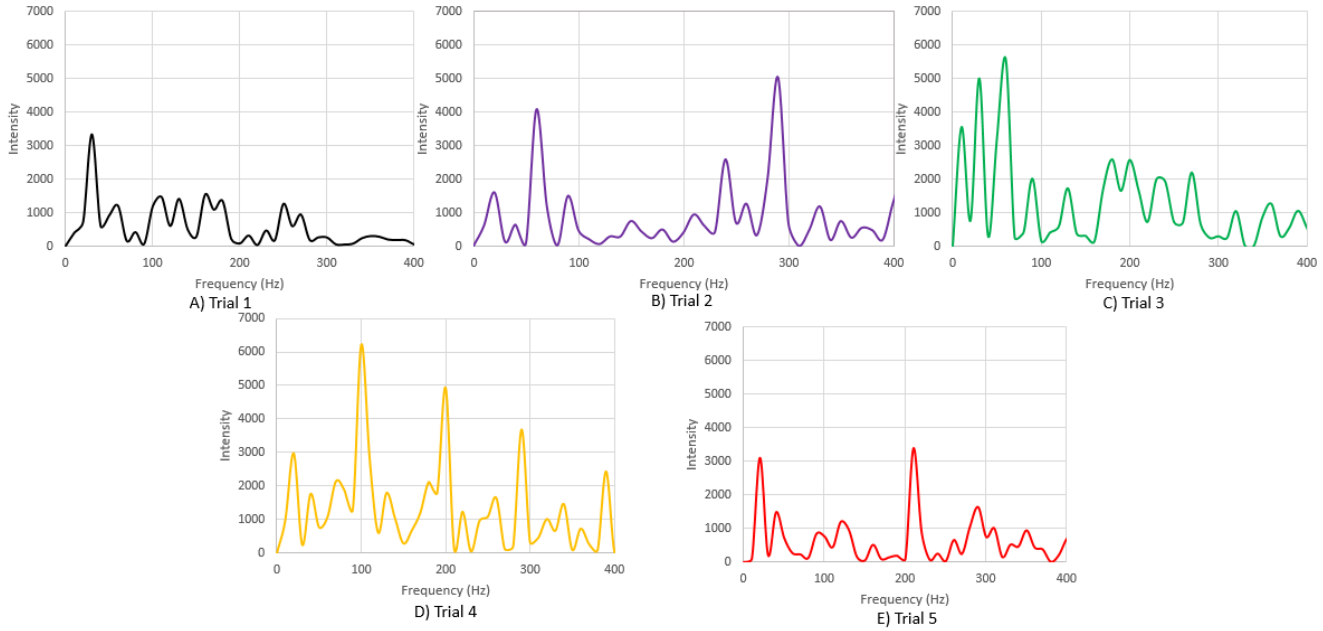

Figure 94: FFT of emission intensity from the middle measurement point

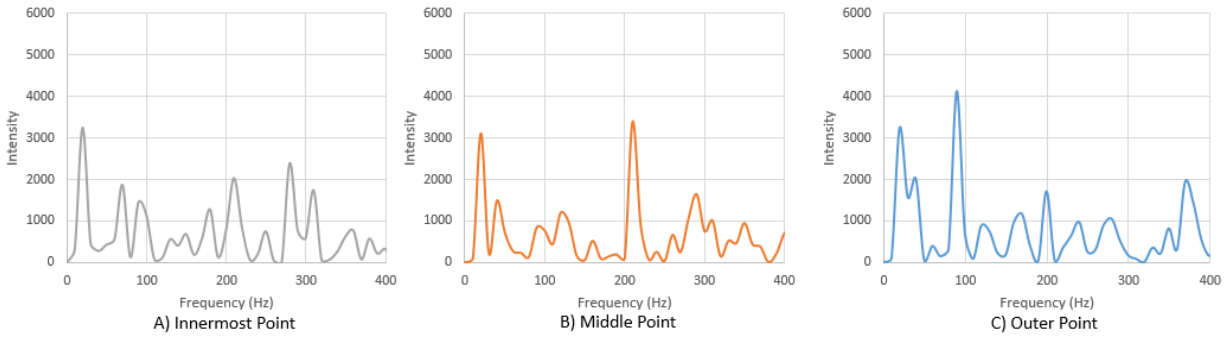

Figure 95: FFT of three locations at the 90/90 flow split conditions

4.2.4 Effectiveness of Step Stabilizer

The backward-facing steps were examined at each experimental condition to determine their efficacy as flame anchors. To conduct this analysis, one thousand consecutive frames (0.1 seconds of data) from each flow split were averaged resulting in a composite image with lighter regions indicating areas of greater OH radical presence. If a recirculating flame was present behind a step, that region would on average have more flame activity and thus appear brighter in the averaged image. Resulting analysis for the 90/70 flow split (left) and 90/90 flow split (right) can be seen in Figure 96 with the UCC geometry and flow features highlighted for ease of interpretation. From the left image, recirculation behind the fuel only steps (1, 3, and 5) can be seen which extends radially to the bottom of the step and tapers until it breaks up at 1.5 step heights downstream. No recirculation was present at the step face of the fuel and air steps (2 and 4). A layer of low flame activity extends from the fuel and air steps along the outside diameter of the cavity until approximately three step heights downstream. The 75/80, 80/90, and 90/30 flow split conditions exhibited similar patterns as observed in the 90/70 flow split. However, the 90/90 flow split experienced recirculation regions behind each step which led to more flame in the cavity and a more uniform cavity intensity. As fuel flow was constant at each step and across the five flow splits, this behavior can be explained by examining the airflow supplied to the steps. The first four

flow splits had larger step air mass flows resulting in a jet of air exiting the step region and disrupting recirculation behind the step. Whereas, the 90/90 flow split had the lowest airflow resulting in less mass flow behind the step allowing recirculation to occur and a subsequent flame to anchor. Recirculation behind each step led to more combustion occurring in the cavity and, correlating to DeMarco et al. [8], produced the hottest exit temperatures.

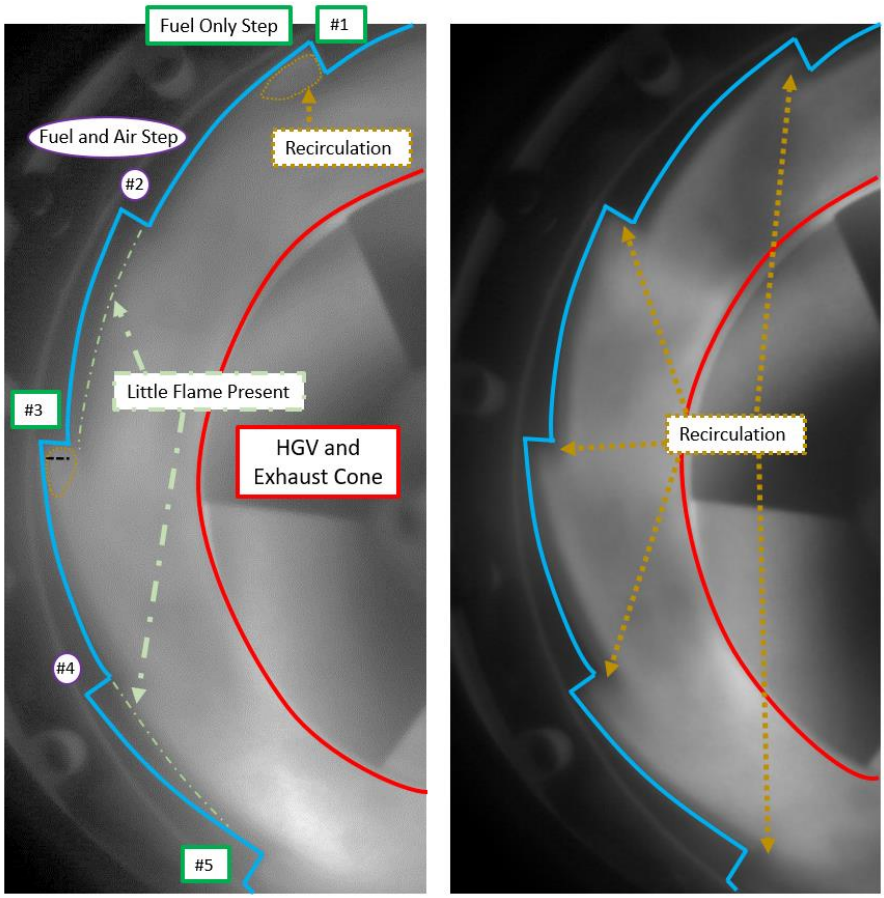

Figure 96: Average of 1,000 CI frames indicating areas of consistent flame activity for 90/70 flow split (left) and 90/90 flow split (right)

To quantify the reaction intensity behind each step, average CI intensity was measured parallel to the step face, one half step height downstream and from the furthest radially inward location of the step to three quarters of its height as indicated by the black dashed line on step #3 in Figure 96. These values were then normalized by the average of each average intensity from all

five conditions. The resulting data from this analysis is shown in Figure 97. The 75/80 flow split condition exhibited lower flame activity in the top of the cavity compared to the bottom resulting in lower intensity in step one. The 80/90, 90/30, and 90/70 flow split conditions had noticeable intensity disparities between the fuel, and fuel and air steps. Among these, the greatest difference was in the 90/30 flow split which also had the largest step airflow. This result further indicates that large air jet velocities will dominate the flow field and prevent recirculation. The 90/90 flow split had much lower step-to-step variation, coinciding with the lowest step airflow, and recirculation was present behind all step types.

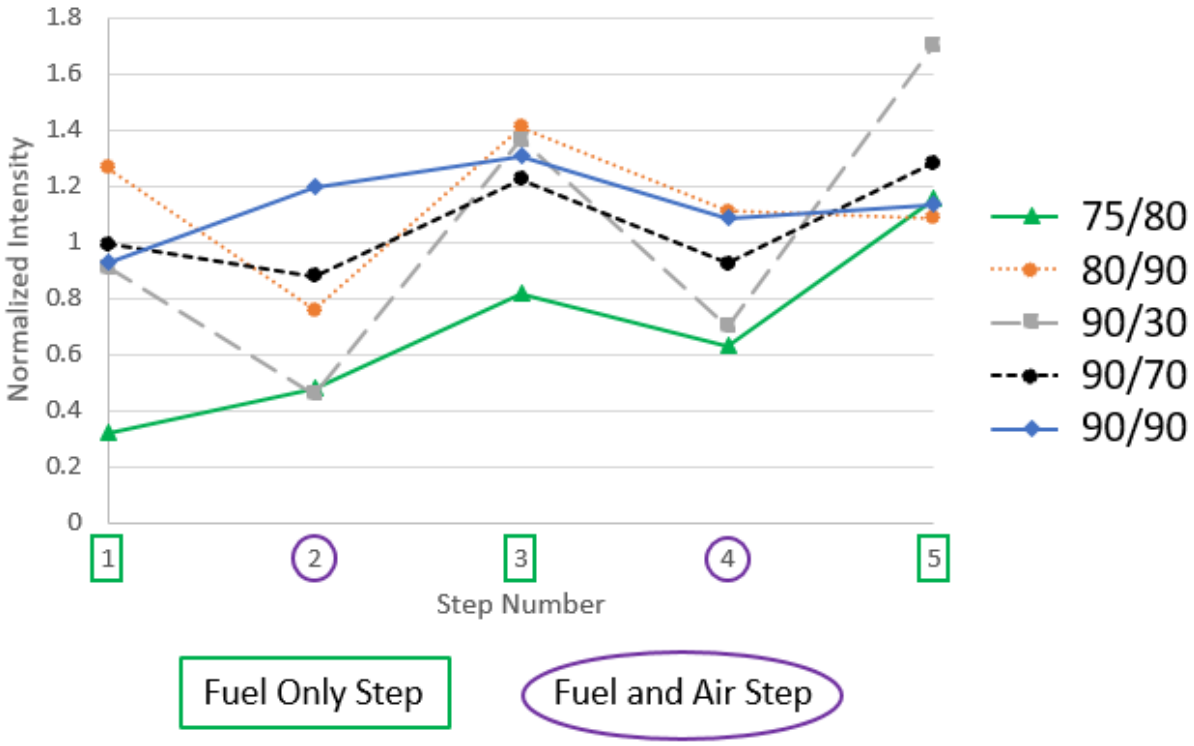

Figure 97: Normalized CI intensity behind five sequential steps

4.2.5 Flameout Combustion Behavior

Unsuccessful attempts were made to reach the 90/10 flow split conditions by starting at the 90/30 flow split condition and incrementally altering flow parameters. While flameout occurred,

panchromatic data captured 0.273 seconds prior to loss of combustion provided further insight into the UCC's flame stabilizing mechanisms and is shown in Figure 98. In this image, the bright blue indicates flame presence and the profile of the 12-step outer ring can be seen along the outside diameter of the UCC. As airflow to the steps was increased to 90% of the cavity flow, the momentum of the air jets dominated the step flow, preventing recirculation at the air and fuel steps and buffering the recirculation region at the fuel only step from the rest of the cavity. With the recirculation region prevented from interacting with the rest of the cavity flow, it ceased functioning as a flame anchor. This resulted in the remaining cavity flame completely lifting off of the 12-step outer ring, pushing all cavity combustion to the perimeter of the HGV. A combination of turbulent flame propagation in the mixture and vortical structures in the cavity flow enabled a temporarily sustained flame, but this was short lived and resulted in flameout. This observed behavior confirms the flameout boundary established by DeMarco et al. [8], and indicates that step air flow, not average tangential cavity velocity, is the driving factor in flameout. At large mass flow rates, step air momentum not only prevents recirculation behind the fuel and air step, but prevents flame anchoring by the fuel only step by isolating it from the primary cavity flow.

Figure 98: Circumferential cavity combustion 0.273 seconds prior to flameout

4.2.6 Circumferential Cavity Flow Path and Residence Time

With the addition of the flow collar, radical emissions could be tracked for longer durations allowing a more clear understanding of flow path and residence time within the cavity. Both OH and CH emissions were recorded, but only the latter was used as it provided new insight to cavity flow behavior. At the interface between a combusting region and flameless void, CH intensity spiked. Using *ImageJ* software, a composite image was created that showed the maximum intensity at each pixel location from the compiled images. The camera's capture speed had a strobe-light like effect, capturing the CH intensity spike as it traveled with the flow path. Thus a lower intensity regions would be present in the composite image where the frame had progressed between camera exposures. N number of these low intensity regions would be present when N number of frames were used to create the composite image. To demonstrate this phenomenon, a

magnified portion of a composite image is shown from the region detailed in Figure 99. The flame movement can be seen in three composite images, each starting at the same time, but composed of increasing numbers of frames as shown in Figure 100. The area of lower intensity, formed where the flame's progress occurred between images, are highlighted in red.

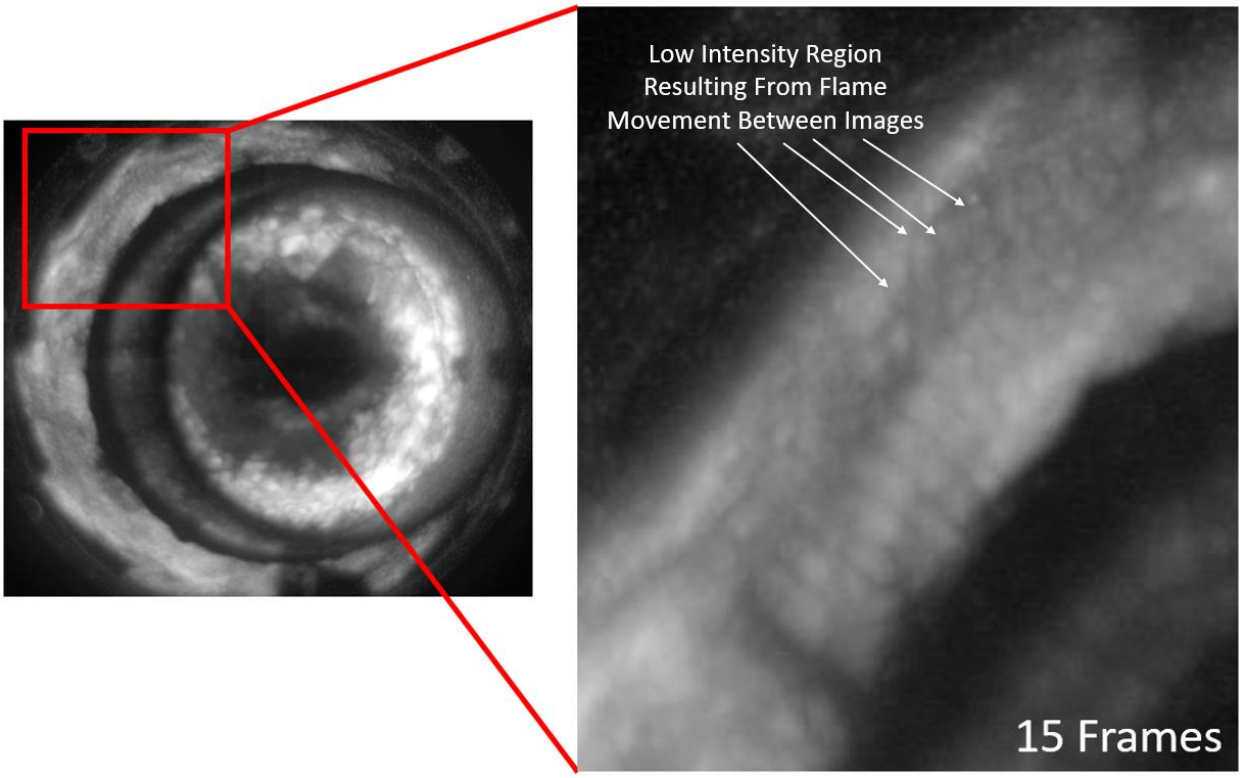

Figure 99: Maximum intensity composite CH emission image from the 90/30 flow split

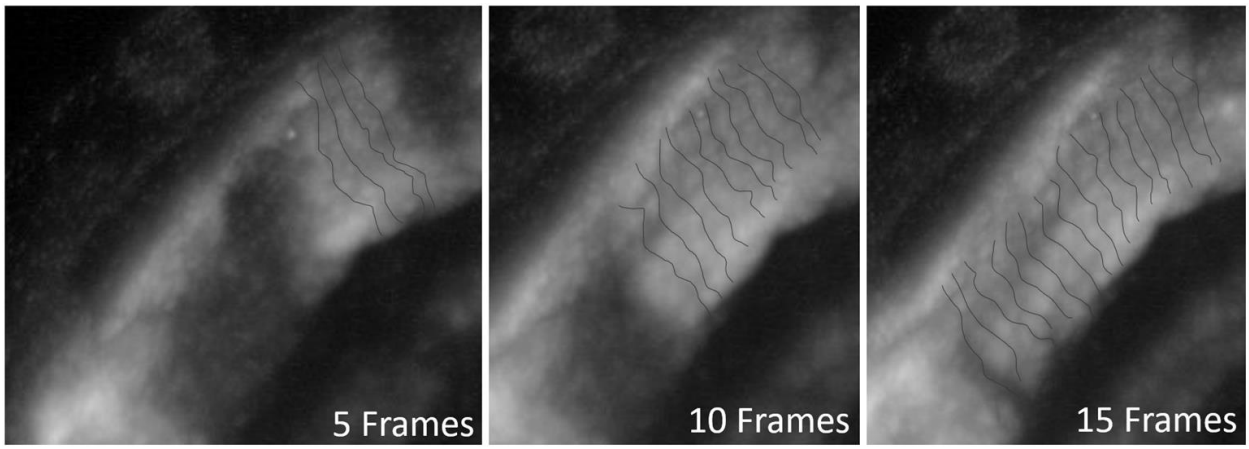

Figure 100: Maximum intensity composite CH emission images the 90/30 flow split

This analysis method provided two details on flow behavior. First, the path of a high intensity region could be tracked as it traveled around the circumferential cavity. Second, path travel time could be calculated by counting the number of steps, as shown in Figure 100, and multiplying by the time step between images. For actual calculated values, composite images were examined at most five frames at a time to minimize image blurring. If distinct voids in the combustion field were not present, visual tracking of the flow path was used.

Values for various flow splits are shown in Table 11 in addition to the measured tangential velocity from Table 10 and exit temperatures observed by DeMarco et al. [8]. As previously mentioned, flow in the circumferential cavity fluctuated in both direction and magnitude non-periodically and as such the data reported below characterized the time-averaged motion. As the initiation of a high intensity region was difficult to determine, a uniform starting point at a fuel only step was selected as the flow leaving this step had the greatest visibility to the camera. Additionally, the flow accelerated in proximity to the HGV, making the terminal leg of the travel path difficult to determine. However, this last portion of travel composed only a small percentage of the total path travel time limiting the impact of this uncertainty.

Table 11: Combustion flow path, travel time, and exit temperatures

Core Percent	**Air Injection Plate Percent**	**Flow Path Length (cm)**	**Flow Path Travel Time (ms)**	**Average Cavity Tangential Velocity (m/s)**	**Average UCC Exit Plane Temperature (K)** [8]
80	90	9	4	5.73	808
90	30	8	3	6.24	792
90	70	9	6	5.55	840
90	90	13	8	4.33	850

Flow path length did not vary greatly between the cases as ingestion into the HGV occurred in discrete locations, at the vane passages as can be seen in Figure 101. Unless the changes between

flow conditions were significant enough, flow would continue to be primarily entrained into the same HGV vane passage. Therefore two different flow conditions, such as 90/30 and 90/70 flow split conditions, had nearly identical flow path lengths. However, the velocity along that path varied, resulting in the changes in flow path travel time. The 90/90 flow split condition had a longer average path of travel compared to the other flow splits, as it was evenly entrained between two vane passages. While a combusting recirculation region was not present behind the fuel and air step, which made the flow path at this step much more difficult to determine with CI, the fuel was likely heating up and initiating pre-combustion decomposition enabling it to ignite much more quickly at the recirculation region at the fuel only step. From the measurements taken from the fuel only step, flow path travel time and tangential velocity had a nearly linear relationship to the average exit temperature observed by DeMarco et al. [8]. This finding confirms their assessment, showing that the benefit of centrifugally enhanced combustion was minimized by the greater residence time that occurred at lower tangential velocities.

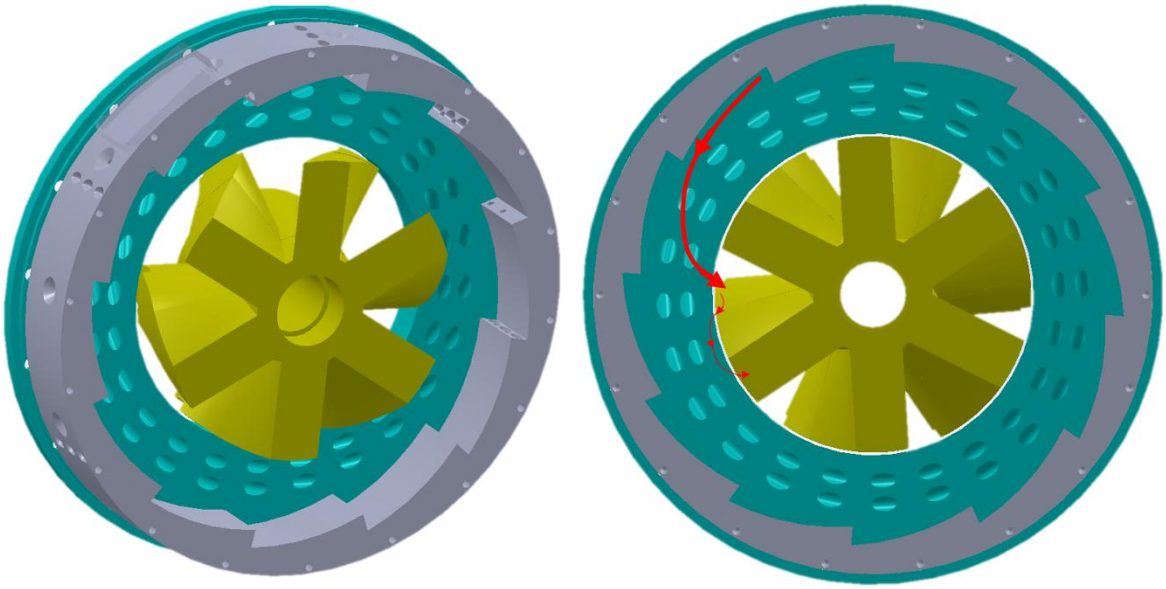

Figure 101: Circumferential cavity isometric view (left) and typical flow path (right)

4.2.7 Investigation of Cooled HGV Case 2

To better understand the uneven vane passage temperatures observed while studying passive cooling of the HGV, Case 2 from that study (see Table 6) was evaluated using the uncooled HGV, CI hardware, and optical measurements employed in this section. From the video, flame fluctuations in the cavity were observed, but would not cause a time average temperature difference provided they occurred uniformly. To investigate reaction uniformity, one thousand consecutive video frames were averaged resulting in the composite image seen in Figure 102 where lighter regions indicated areas of greater average CH radical presence. While recirculation appeared behind all the visible steps resulting in reactions filling a large portion of the cavity, local differences in average CH emission intensity are still present.

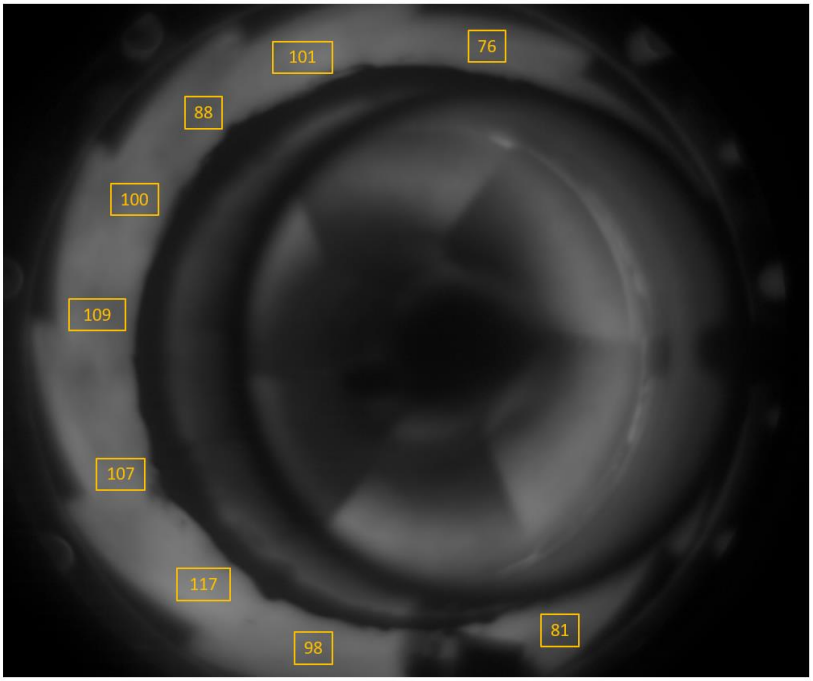

Figure 102: Average CH radical intensity at Case 2 conditions

Average intensity from 20x20 pixel blocks are indicated on the figure to better quantify the results. The lowest average values were both on the top and bottom, right hand side of the image

while a region of high intensity spanned the six to nine o'clock position. This intensity distribution may indicate lower flame activity at the top and bottom of the cavity or that the entire right half (which was not visible) had lower flame activity. As the vane surface temperature observed in Section 4.1.1 exhibited higher temperatures over one half of the vane, the latter of these two scenarios was most likely. The cause of this non-uniformity is unclear and warrants further investigation.

The results of this section concludes the second research objective of understanding the relation between tangential velocity within the circumferential cavity and average combustion exit temperature. Flow within the combustor was found to become increasingly unsteady at increasing cavity tangential velocities. This also led to less volume of the cavity being filled with reactions. Tangential velocity was confirmed to be a function of the way in which air was introduced in the UCC, decreasing as more of the total flow was directed to the core or cavity flow was directed to the air injection plate. Local velocity distribution was impacted by the orientation of the HGV, where flow around the vane tips disrupted the tangential movement of the bulk rotating flow. Velocity also affected the ability of the backward facing steps to stabilize a flame where increasing velocity would first lower flame activity behind the fuel and air steps and then cause the flame to lift off the outside diameter all together. Lastly, while the length of the flow path from the outside diameter to the HGV did not vary greatly between flow conditions, the time taken to travel that path did. Lower cavity tangential velocities were observed to have longer residence times correlating to the hotter combustor exit temperatures previously reported.

V. Conclusions

The Ultra Compact Combustor promises to greatly reduce the size of a gas turbine engine's combustor by altering the manner in which fuel is burnt. This reduction is achieved by using a circumferential cavity as the combustion primary zone to hold a rotating flame. The Hybrid Guide Vane is located in the center of the UCC both altering the exiting gas flow angle and serving as a secondary combustion zone. As improved UCC designs lead to higher operating temperatures, cooling of this unique piece of hardware must be considered. Therefore, the first objective of the present investigation was to determine the impact of HGV passive cooling scheme features on the vane surface temperature distribution. Critical to achieving these higher operating temperatures is understanding the complex flow field and combustion dynamics within the circumferential cavity. However, previous UCC hardware had only limited optical access, enabling visualization of no more than 20% of the cavity. As such, the second objective of this research was to modify AFIT's UCC hardware to provide a full field view of the circumferential cavity to enable enhanced optical analysis. The third and final objective was to use the modified UCC hardware to investigate the relation between cavity tangential velocity and average exit temperature. Previous investigations have identified the operating conditions that produced the highest exit temperatures, but the combustion behavior that resulted in these values has not previously been identified.

5.1 HGV Passive Cooling Conclusions and Recommendations

As the HGV is a unique component to AFIT's UCC design, cooling of this part must be considered as combustor temperatures continue to increase. By comparing five cooled HGV configurations and a solid vane, the effect of individual cooling scheme design parameters was able to be determined. All designs employed a leading edge slot to ingest cooler air upstream of

the combustor. As expected, internal coolant flow was found to have a positive benefit as it transferred heat away from the vane surface and into the internal flow. This resulted in a proportionally greater temperature decrease between an upstream and downstream axial position compared to the uncooled solid vane. Additionally, vanes that had higher internal mass flow exhibited greater normalized temperature decrease between three axial chord locations compared to those with lower internal mass flow.

Each configuration was tested at three core mass flows while holding flow to the cavity constant. The resulting surface temperature profile, but not magnitude, was nearly identical across all three cases. The greatest temperature decrease between two axial chord locations occurred at the lowest core flow condition. As fuel flow, and thus potential heat release, remained the same between all cases, this result indicates that a given vane cooling scheme will perform better at specific operating conditions. Therefore, future cooling schemes must be tailored to the UCC operating condition in which they will be used to achieve their peak benefit.

Next blowing ratio was examined. The vane trailing edge slot size and internal plug location played a key role in developing the vane internal to external pressure differential that drove the blowing ratio. The vane with no trailing edge slot had six times greater vane internal to external pressure difference compared to the vane with a large trailing edge slot, altering the blowing ratio from approximately 0.9 to 0.3. With no trailing edge slot, the blowing ratio was too large, creating detached coolant jets that penetrated into the passage flow. However, this had the positive benefit of disrupting the combustor hot streak migration causing a more uniform vane surface temperature profile. The large trailing edge slot size yielded a blowing ratio that was half of the ideal value creating coolant jets that had no impact on passage flow and provided limited surface cooling benefit. This difference in blowing ratio effect showed the importance of achieving

the ideal vane internal to external pressure difference to obtain maximum benefit from the film-cooling jets.

Although slot size affected blowing ratio, it also had a large impact on internal coolant mass flow rate. The vane with no trailing edge slot had much less total coolant flow resulting in very little temperature change between axial chord locations. The vane internal plug presents a means to alter the vane internal to external pressure difference while having minimal impact on coolant mass flow rate. Previous studies indicated that halving the distance of the internal plug from the vane inlet reduced coolant flow by 2% and the present study found this same change doubled the vane internal to external pressure difference. This indicates the cooling scheme design process should first establish the trailing edge slot size necessary to achieve the desired coolant mass flow rate, then alter the internal plug distance to achieve the desired pressure differential.

The film-cooling scheme employed was designed to assess viability, not to maximize effectiveness. Thus large surface temperature reductions from this cooling technique were not observed, nor were the tests able to determine surface temperature reduction. However, comparison between a vane with film-cooling and one without revealed a greater temperature reduction between two axial chord locations indicating a positive benefit. This result confirms the viability of film-cooling using passive air ingestion and as such the next cooled HGV configuration should employ a smaller pitch spacing and employ more coolant holes for maximum benefit.

There are two areas of improvement to build upon the current investigation. Non-uniformity in the combustion source presented many challenges in data analysis and prevented direct temperature comparisons between vanes. Therefore, future experimental efforts should focus on designing a uniform heat source to alleviate this issue. Additionally, the lessons learned about cooling the HGV should be implemented into an improved cooling scheme. Future work

must consider the balance between diverting air for cooling and using it for combustion. Conducting engine cycle analysis would provide the necessary data to assist future researchers in making this decision.

5.2 Modification to AFIT's UCC Hardware Conclusions

Optical measurements have the desired spatial and temporal resolution to characterize combusting flow dynamics. However, previous UCC hardware employed either a 1.91 cm x 2.54 cm rectangular or 2.45 cm wide 80° arc quartz window enabling no more than 20% of the circumferential cavity to be imaged. To maximize the visible area, the UCC back plate was redesigned to be made entirely of quartz. Its design featured several modifications to prevent cracking due to thermal expansion such as enlarged clearances between all metal components, employing springs to secure the quartz to the UCC while still permitting part growth, and eliminating the compression mounted metal exhaust collar via a thicker back plate. An exhaust collar was added to further enhance optical access to the circumferential cavity by blocking exiting combustor flames. This component featured a tapered design to clear the camera's line of sight. It attached to the exhaust enclosure so as not to put additional stress on the quartz, and used a Fiberfrax gasket to both pad and seal the collar on the quartz surface. The resulting design achieved unrestricted optical access to the circumferential cavity enabling optical measurements of the entire combusting flow field of interest. Additionally, the modified hardware suffered no failures over 29 test cycles, providing a continued benefit to AFIT's UCC research.

5.3 Flow Dynamics in the Circumferential Cavity Conclusions and Recommendations

The implementation of the quartz back plate enabled previously unattainable optical access to the circumferential cavity. This was leveraged by using a high speed camera, image intensifier,

and bandpass filters to capture chemiluminescence of OH and CH radicals. Flow conditions from DeMarco et al. [8] were replicated to understand the combustor behavior driving their observed average exit temperatures. Operating conditions with the highest stability (90% core and 90% air injection plate flow split) exhibited the steadiest combustion flow with reactions filling the entire cavity. Less stable operating conditions had regions of low flame activity intermittently appearing in the rotating flow field and along the outside diameter of the 12-Step ring. As expected, more combustion within the cavity correlated to previously observed higher exit temperatures.

Quantitative analysis of the video data began with assessing the average tangential velocity at each cavity location by tracking the movement of OH radicals. Increasing the percentage of total flow directed to the core or the percentage of cavity flow directed through the air injection plate decreased the average tangential velocity within the cavity. This was logical based on the orientation in which air moves through these features and agrees with the average velocities found by DeMarco et al. [8]. Local tangential velocity was found to have little variation in the radial direction, but a periodic increase in the circumferential direction coinciding with both the air and fuel step on the 12-Step outer ring and the vane passages on the HGV. As flow moving both tangentially and radially inward approached an HGV vane passage, the flow would impact the vane pressure surface. The majority of the flow would then entrain into the vane passage while a lesser portion spilled back into the circumferential cavity prior to entraining into the next downstream vane passage. This movement disrupted the tangential motion of the flow near the HGV vane tips driving a significant portion of the observed non-uniformities in the combusting flow field. This disruption is undesirable as it contributes to less uniform combustion and a larger pattern factor. By adding a fillet to the portion of the HGV vane sides that are in the circumferential

cavity, flow could more easily divide between two vane passages decreasing the disruption to the local flow field.

Frequency of the flow field was assessed by performing a Fast Fourier Transform of the intensity data at select pixel locations. Bohan et al. [27] reported two frequency observations while investigating a similar UCC configuration: one where the entire visible cavity intensity pulsed in unison and another where the intensity rippled across the visible area at the same velocity as the bulk circumferential motion. Neither of these phenomena was observed in the present study. While low combustion areas were present and rotated at the same speed as the cavity flow, they would inconsistently form and breakup resulting in dominant frequencies too fast to coincide with a rotating flame front.

To investigate flame stability in a fluctuating flow field, the average intensity at each pixel location across the entire video was calculated. The resulting composite image displayed where flame activity was on average higher. This analysis indicated recirculating flow behind the steps was effectively anchoring a flame. At low cavity tangential velocities, this occurred behind both types of steps. As tangential velocity increased, the fuel and air steps exhibited less flame activity than the fuel only steps. Lesser flame activity also extended downstream along the outside diameter of the cavity from the fuel and air step. This behavior was explained by the increasing mass flow rate through the air injection holes on the step faces. As the air jet momentum increased, the shear layer above that step was weakened. At test conditions that produced a large cavity tangential velocity, combustion was observed to lift entirely off of the outside diameter and stabilize around the HGV. Any further increase in cavity tangential velocity caused the flame to extinguish. This observation confirms the flameout boundary line established by DeMarco et al. [8], indicating that

step air, and not average tangential velocity within the cavity, is the driving mechanism behind flameout.

The last analysis performed examined the effect of cavity tangential velocity on flow path length and flow path travel time. Areas of peak intensity were tracked as they progressed from the outside diameter of the cavity to the perimeter of the HGV. While individual particles traveled less uniform paths, the bulk motion of these larger groupings followed similar trajectories. As flow could only enter the HGV at discrete locations, the path of travel was fairly uniform in length between different flow conditions. All conditions had a path of flow travel that traversed approximately 60° of the cavity with the exception of 90/90 flow split condition, which had the lowest tangential velocity and traveled an average of 90°. In this last flow split, flow was evenly entrained between two vane passages causing half of the flow to travel 60° of the cavity and half to travel 120°. The time taken for the flow to transit was a strong function of tangential velocity, with slow flow taking the longest time. This confirms the hypothesis of DeMarco et al. [8] that at low tangential velocities increased residence in the combustor occurred and resulting in increased average exit temperatures.

Based on the experiments conducted and the data collected, the author has three recommendations for future work. First, purchase a larger window for the exhaust enclosure to allow the camera to be positioned further back. Increasing the distance between the back plate and camera lens would enable the entire circumferential cavity to be imaged at the same time. This would take full advantage of the quartz back plate and enable further data collection. Second, examine the combustion dynamics after replacing the HGV with a vaneless center body. As the HGV disrupted both tangential velocity and length of flow path, its removal may allow enhanced fuel residence and thus exit temperatures. Lastly, examine the combustor dynamics with no airflow to the steps. While this configuration previously resulted in a fuel rich zone along the outside

diameter, turbulent mixing due to step induced instabilities may prevent this issue. The 12-Step outer ring would need to be modified to prevent fuel from being forced into the air injection holes and thus filling the air plenum with a highly combustible fuel and air mixture.

References

[1] Mattingly, J. D., Heiser, W. H., and Pratt, D., *Aircraft Engine Design*, AIAA, Reston, Virginia, 2nd ed., 2002.

[2] Zelina, J., Sturgess, G. J., and Shouse, D. T., "The Behavior of an Ultra-Compact Combustor (UCC) Based on Centrifugally-Enhanced Turbulent Burning Rates," Proceedings of the 40th AIAA/ASME/SAE/ASEE Joint Propulsion Conference and Exhibit, 2004, AIAA 2004-3541.

[3] Lewis, G. D., "Swirling Flow Combustion - Fundamentals and Application," *Presented at AIAA/SAE 9th Propulsion Conference, Las Vegas, Nevada*, November 1973, AIAA Paper No. 73-1250.

[4] Bohan, B. T., *Analysis of Flow Migration in an Ultra Compact Combustor*, Master's thesis, Air Force Institute of Technology, WPAFB, OH, 2011, AFIT/GAE/ENY/11-M02.

[5] DeMarco, K. J., *Control, Characterization, and Cooling of an Ultra Compact Combustor*, Master's thesis, Air Force Institute of Technology, WPAFB, OH, 2018, AFIT-ENY-MS-18-M-250.

[6] Bohan, B. T., Polanka, M. D., and Rutledge, J. L., 2017. "Computational Analysis of a Novel Cooling Scheme for Ultra Compact Combustor Turbine Vanes". *Proceedings of the ASME Turbo Expo 2017: Charlotte, NC*. GT2017-63319.

[7] DeMarco, K. J., Bohan, B. T., Polanka, M. D., Rutledge, J. L., and Akbari, P.J., 2018. "Computational Analysis of an Additively Manufactured Cooled Ultra Compact Combustor Vane". *Proceedings of the ASME Turbo Expo 2018: Oslo, Norway*. GT2018-75392.

[8] DeMarco, K. J., Bohan, B. T., Rathsack, T. C., Polanka, M. D., and Goss L. P., "Performance Characterization of a Circumferential Combustion Cavity," *Joint Propulsion Conference, Cincinnati, Ohio,* 2018, AIAA-2018-4922.

[9] Turns, S. R., *An Introduction to Combustion*, McGraw-Hill, Inc, New York, 2012, 3rd Edition.

[10] Klimov, A. M., "Premixed Turbulent Flames--Interplay of Hydrodynamic and Chemical Phenomena," *8th ICOGER, Minsk, USSR,* 1981.

[11] Yonezawa, Y., Toh, H., Goto, S., and Obata, M., "Development of the Jet-Swirl High Loading Combustor," *26th AIAA/ASME/SAE/ASEE Joint Propulsion Conference, Orlando, FL,* 1990, AIAA-90-2451.

[12] Williams, G. C., “Basic Studies on Flame Stabilization," *Journal of the Aeronautical Sciences,* Vol. 16, No. 12, pp 714-722, 1949.

[13] McManus, K. R., Vandsburger, U., and Bowman, C. T., “Combustor Performance Enhancement Through Direct Shear Layer Excitation,” *Journal of Combustion and Flame,* Vol. 82, pp 75-92, 1990.

[14] Lapsa, A. P. and Dahm, W. J., “Hyperacceleration effects on turbulent combustion in premixed step-stabilized flames," *Proceedings of the Combustion Institute,* Vol. 32, 2009, pp. 1731-1738.

[15] Lapsa, A. P. and Dahm, W. J. A., “Experimental Study on the Effects of Large Centrifugal Forces on Step-Stabilized Flames," *Proceedings of the 5th US Combustion Meeting, San Diego, CA,* 2007, H14.

[16] Damele, C. J., Polanka, M. D., Wilson, J. D., and Rutledge, J. L., “Characterizing Thermal Exit Conditions for an Ultra Compact Combustor," *Proceedings of the 52nd AIAA Aerospace Sciences Meeting,* 2014, AIAA-2014-0456.

[17] Briones, A. M., Sekar, B., and Erdmann, T. J., “Effect of Centrifugal Force on Turbulent Premixed Flames," *Journal of Engineering for Gas Turbines and Power,* Vol. 137, 2015, GTP-14-13091.

[18] Moenter, D. S., *Design and Numerical Simulation of Two Dimensional Ultra Compact Combustor Model Sections for Experimental Observation of Cavity-Vane Flow Interactions*, Master's thesis, Air Force Institute of Technology, WPAFB, OH, 2006, AFIT/GAE/ENY/06-S07.

[19] Thomas, L. M., *Flow Measurements Using Particle Image Velocimetry In The Ultra Compact Combustor*, Master's thesis, Air Force Institute of Technology, WPAFB, OH, 2009, AFIT/GAE/ENY/09-S18.

[20] LeBay, K. D., Drenth, A. C., Thomas, L. M., Polanka, M. D., Branam, R. D., and Schmidt, J. B., “Characterizing the Effects of G-Loading in an Ultra Compact Combustor via sectional models," *Proceedings of the ASME Turbo Expo 2010, Glasgow, UK,* 2010, GT2010-22723.

[21] Wilson, J. D., Damele, C. J., and Polanka, M. D., “Flame Structure Effects at High G-Loading," *Journal of Engineering for Gas Turbines and Power,* Vol. 136, 2013, GTP-14-1068.

[22] Conrad, M. M., *Integration of an Inter Turbine Burner to a Jet Turbine Engine*, Master's thesis, Air Force Institute of Technology, WPAFB, OH, 2013, AFIT/GAE/ENY/13-M-06.

[23] Cottle, A. E. and Polanka, M. D., "Numerical and Experimental Results from a Common-Source High-G Ultra-Compact Combustor," *Proceedings of the ASME Turbo Expo 2016 Seoul, South Korea*, 2016, GT2016-56215.

[24] Cottle, A. E. and Polanka, M. D., "Optimization of Ultra Compact Combustor Flow Path Splits," *Proceedings of the 53rd AIAA Aerospace Sciences Meeting, AIAA SciTech*, 2015, AIAA-2015-0100.

[25] Cottle, A. E., Polanka, M. D., Goss, L. P., and Goss, C. Z., "Investigation of Air Injection and Cavity Size Within a Circumferential Combustor to Increase G-Load and Residence Time," *Journal of Engineering for Gas Turbines and Power*, Vol. 140, 2016, GTP-17-1182.

[26] Bohan, B. T., Polanka, M. D., and Goss, L. P., "Development and Testing of a Variable Geometry Diffuser in an Ultra-Compact Combustor," *Proceedings of AIAA SciTech Forum, Grapevine, Texas*, 2017, AIAA-2017-0777.

[27] Bohan, B. T., Polanka, M. D., and Goss, L. P., "Measurement of Temperature, Pressure, Velocity, and Frequency in an Ultra Compact Combustor," *56th AIAA Aerospace Sciences Meeting, SciTech Forum, Kissimmee, FL*, 2018.

[28] Han, J. C., "Heat Transfer Augmentation Technologies for Internal Cooling of Turbine Components of Gas Turbine Engines," *International Journal of Rotating Machinery*, Vol. 2013, 2013, Article ID 275653.

[29] Bogard, D. G. and Thole, K. A., "Gas Turbine Film Cooling," *Journal of Propulsion and Power, Vol. 22, pp 249-269*, December 2005.

[30] Baldauf, S., Schulz, A., and Wittig, S., "High-Resolution Measurements of Local Effectiveness From Discrete Hole Film Cooling," *Journal of Turbomachinery*, Vol. 123, 2001, pp. 758-765.

[31] Hay, N. and Lampard, D., "Discharge Coefficients of Turbine Cooling Holes: A Review," *Journal of Turbomachinery*, Vol. 120, pp 314-319, April, 1998.

[32] Gritsch, M., Schulz, A., and Wittig, S., "Effect of Crossflows on the Discharge Coefficient of Film Cooling Holes With Varying Angles of Inclination and Orientation," *Journal of Turbomachinery*, Vol. 123, pp 781-787, Feb, 2001.

[33] Bohan, B. T., *"Combustor Dynamics and Heat Transfer In An Ultra Compact Combustor,"* Doctoral Dissertation, Air Force Institute of Technology, WPAFB, OH, 2009, AFIT-ENY-DS-18-S-057.

[34] Modest, M. F., *Radiative Heat Transfer*, Oxford Academic Press, Boston, 2013, 3rd Edition.

[35] Teledyne Judson Technologies, “Photoconductive Mercury Cadmium Telluride Detectors,” http://www.teledynejudson.com/products/photoconductive-mercury-cadmium-telluride-detectors, accessed 17-Sep-2018.

[36] Coblentz, W. W. and Hughes, C. W., “Emissive tests of paints for decreasing or increasing heat radiation from surfaces," *US Bureau of Standards,* Vol. 18, No. 254, pp 171-187, 1924.

[37] FLIR, “FLIR Thermal Imaging Cameras Reveal What’s Behind The Flames,” https://www.flir.com/discover/instruments/furnace-boiler/petroval/, accessed 18-Sep-2018.

[38] InfraTec, “Standard Infrared Filters and Infrared Windows from InfraTec,” https://www.infratec-infrared.com/sensor-division/ir-filters/, accessed 18-Sep-2018.

[39] Martiny, M., Schiele, R., Gritsch, M., and Wittig, S., “In Situ Calibration for Quantitative Infrared Thermography," *Quantitative InfraRed Thermography Journal*, Vol. 96, June 1996, pp. 3-8.

[40] Vogert, C. J., *Relating Film Cooling Performance Between Ambient and Near Engine Temperatures,* Master's thesis, Air Force Institute of Technology, WPAFB, OH, 2017, AFIT-ENY-MS-17-M-157.

[41] Adrian, R. J., “Twenty Years of Particle Image Velocimetry," Experiments in Fluids, Vol. 39, 2004, pp. 159-169.

[42] Fisher, R., Perkins, S., Walker, A., and Wolfart, E., “Laplacian/Laplacian of Gaussian,” http://homepages.inf.ed.ac.uk/rbf/HIPR2/log.htm, accessed 20-Jan-2019.

[43] Wilson, J. D., *Characterizing G-Loading, Swirl Direction, and Rayleigh Losses in an Ultra Compact Combustor,* Master's thesis, Air Force Institute of Technology, WPAFB, OH, 2013, AFIT-ENY-13-S-02.

[44] Kestin, J., “Thermodynamic Properties of Combustion Gases," *Journal of Aeronautical Sciences,* Vol. 20, No. 8, pp 234-242, 1948.

[45] Huning, M., “Discharge Coefficient Measurements of Round, Inclined Orifices With Inlet Cross-Flow In and Against Direction of Inclination," *Journal of Mechanical Engineering Science,* Vol. 227, No. 6, pp 1266-1279, 2012.

REPORT DOCUMENTATION PAGE

Form Approved
OMB No. 0704-0188

1. REPORT DATE *(DD-MM-YYYY)*	2. REPORT TYPE	3. DATES COVERED *(From - To)*
21-03-2019	Master's Thesis	29 September 2017 - 21 March 2019

4. TITLE AND SUBTITLE
Examination of Flow Dynamics and Passive Cooling in an Ultra Compact Combustor

5a. CONTRACT NUMBER

5b. GRANT NUMBER

5c. PROGRAM ELEMENT NUMBER

6. AUTHOR(S)
Rathsack, Tylor C, Capt

5d. PROJECT NUMBER

5e. TASK NUMBER

5f. WORK UNIT NUMBER

7. PERFORMING ORGANIZATION NAME(S) AND ADDRESS(ES)
Air Force Institute of Technology
Graduate School of Engineering and Management (AFIT/EN)
2950 Hobson Way
Wright-Patterson AFB OH 45433-7765

8. PERFORMING ORGANIZATION REPORT NUMBER
AFIT-ENY-MS-19-M-239

9. SPONSORING/MONITORING AGENCY NAME(S) AND ADDRESS(ES)
Aerospace Systems Directorate
Dr Andrew Caswell
2130 Eighth St
Wright-Patterson AFB OH 45433-7542
andrew.caswell.4@us.af.mil

10. SPONSOR/MONITOR'S ACRONYM(S)
AFRL/RQT

11. SPONSOR/MONITOR'S REPORT NUMBER(S)

12. DISTRIBUTION/AVAILABILITY STATEMENT
Distribution Statement A. Approved for Public Release

13. SUPPLEMENTARY NOTES
This work is declared a work of the U.S. Government and is not subject to copyright protection in the United States.

14. ABSTRACT
The Ultra Compact Combustor (UCC) promises to greatly reduce the size of a gas turbine engine's combustor by burning fuel circumferentially. This design employs a combustor center body that changes the flow path angle. The first goal of the present investigation was to experimentally evaluate five cooling configurations to quantify the impact of internal geometry and film-cooling on the body's surface temperature distribution. The second goal of this investigation was to understand the complex airflow and combustion dynamics that resulted in the hottest combustor exit temperatures. Prior studies have determined what UCC operating conditions created the highest exit temperatures, but not why.

15. SUBJECT TERMS
Compact Combustion, Chemiluminescence, Thermography, Circumferential Combustion

16. SECURITY CLASSIFICATION OF:			17. LIMITATION OF ABSTRACT	18. NUMBER OF PAGES	19a. NAME OF RESPONSIBLE PERSON
a. REPORT	b. ABSTRACT	c. THIS PAGE			Dr. Marc D. Polanka AFIT/ENY
					19b. TELEPHONE NUMBER *(Include area code)*
U	U	U	UU	143	312-785-3636 x4714 marc.polanka@afit.edu

Standard Form 298 (Rev. 8/98)
Prescribed by ANSI Std. Z39.18